Neutron Magnetic Form Factor G_M^n Measurement at High Q^2 with CLAS12

Lamya Baashen

Abstract

LIST OF FIGURES

FIGURE PAGE

LIST OF TABLES

CHAPTER 4

Quasi-elastic Ratio Measurement

In this chapter, we focus on the measurement of the Ratio used to extract G_M^n. We will start by discussing the data sets that have been used for this measurement. Next, we will describe the procedure used to select quasi-elastic $D(e, e'p)$ and $D(e, e'n)$. Finally, we will present the results of the Ratio measurement.

4.1 RGB Run Period

The CLAS12 Run Group B (RG-B) data were taken over three periods: Spring of 2019, Fall of 2019 and Spring of 2020. A 5 cm liquid deuterium target was used with a polarized electron beam operating at three different beam energy (10.6, 10.2 and 10.4 GeV). Two different polarities of the torus magnet was used: outbending, where the track of a negative particle bends away from the beamline, and inbending, where the track of a negative particle bends toward the beamline. A summary of the run conditions are shown in table 4.1. We analyzed each dataset separately. The outbending dataset was excluded from the analysis due to a limited statistics.

Exp. Detail	In-bending	Out-bending	In-bending
Run Period	Spring 2019	Fall 2019	Spring 2020
Run Range	6156 - 6603	11093 - 11300	11323 - 11571
Number of runs	117 runs 106 runs	97 runs	171 runs
Beam	10.6 GeV 10.2 GeV	10.4 GeV	10.4 GeV
Target	Unpolarized LD2	Unpolarized LD2	Unpolarized LD2
Current	35-50 nA	40 nA	35-50 nA
Torus Field	-1	+1/+1.008	-1
Solenoid Field	-1	-1	-1

Table 4.1: RG-B run period conditions

4.2 Events select

and no additional neutrons in the FD? and you ignore hits in the TOF, right?

and no charged particles??

The data files analyzed are referred to as ”gmn” files, which contain events of two channels: $D(e, e'n)$ and $D(e, e'p)$. In the $D(e, e'n)$ channel, the file included events where an electron was detected and all neutral particles in the forward detector, while for $D(e, e'p)$ channel, the file contained events with both an electron and a positive charge particle detected in the forward detector. In both $D(e, e'n)$ and $D(e, e'p)$ channels, the electron identification requires the cuts discussed in Sec. 3.4 and summarized in Table. 4.2. For nucleon identification, different selections were made depending on the channel. In the $D(e, e'p)$ channel, a positively charged particle that hit the calorimeter was selected as a proton candidate, while in the $D(e, e'n)$ channel, neutral particles that hit the calorimeter were considered as neutron candidates as shown in Table. 4.2.

electron	proton	neutron
pid = 11 v_z vertex position $N_{ph} > 2$ PCAL fiducial V, W > 14 cm cut DC fiducial cut for 3 DC regions SF vs. P_{ele} $\pm 3.5\sigma$ Diagonal cut chi2pid $\lvert\chi^2\rvert < 3$ cut Minimum PCAL $E_{dep} > 60$ MeV	Positive charge particle hit calorimeter	Neutral charge particle hit calorimeter

Table 4.2: Cuts used for electron and nucleon identification.

Once a scattered electron has been identified in the $D(e, e'n)$ and $D(e, e'p)$ channels, the 4-momentum of a recoil nucleon (proton or neutron) can be calculated

assuming QE scattering

as:

$$P_e^\mu + P_N^\mu = P_{e'}^\mu + P_{N'}^\mu, \\ P_{N'}^\mu = P_e^\mu + P_N^\mu - P_{e'}^\mu = h^\mu, \tag{4.1}$$

where P^μ=($\vec{P}$, E) is the 4-momentum for each particle, and N is refer to either proton or neutron. The square of the invariant mass of the nucleon can be written as:

$$W^2 = h^\mu h_\mu, \tag{4.2}$$

where h_μ is the 4-momentum of the recoil nucleon.

4.3 Quasi-elastic Selection

this is a good place to put the theta_pq figure to define the angle if it has not been shown yet. I'm losing track of where things are in your thesis.

In order to measure the ratio σ_n/σ_p and extract G_M^n, the Quasi-elastic peak of the $D(e,e'n)$ and $D(e,e'p)$ channels is selected. For the $D(e,e'p)$ channel, we required at least one electron in the forward detector and a positive charge particle hit the calorimeter. For the $D(e,e'n)$ channel, we required at least one electron in the forward detector and a neutron hit the calorimeter. The distribution of the invariant mass W as a function of θ_{pq}, which is the angle between the direction of the detected nucleon (proton or neutron) and the direction of the virtual photon is shown in figure 4.1.

The quasi-elastic events tend to be emitted close to the direction of the momentum transfer $\vec{q}$ ($\theta_{pq} \sim 0°$) while inelastic events are not. It is hard to observe the quasi-elastic peak of the $D(e,e'n)$ event compared to the $D(e,e'p)$ channel due to the mixing of the neutron with photons at this stage. The invariant mass W distribution of $D(e,e'p)$ and $D(e,e'n)$ channels, shown in Fig 4.2, show a significant amount of inelastic background events, which ~~makes~~ the quasi-elastic peak of the nucleon ~~difficult to observe~~. Therefore, several cuts need to be applied to reduce the inelastic

obscures

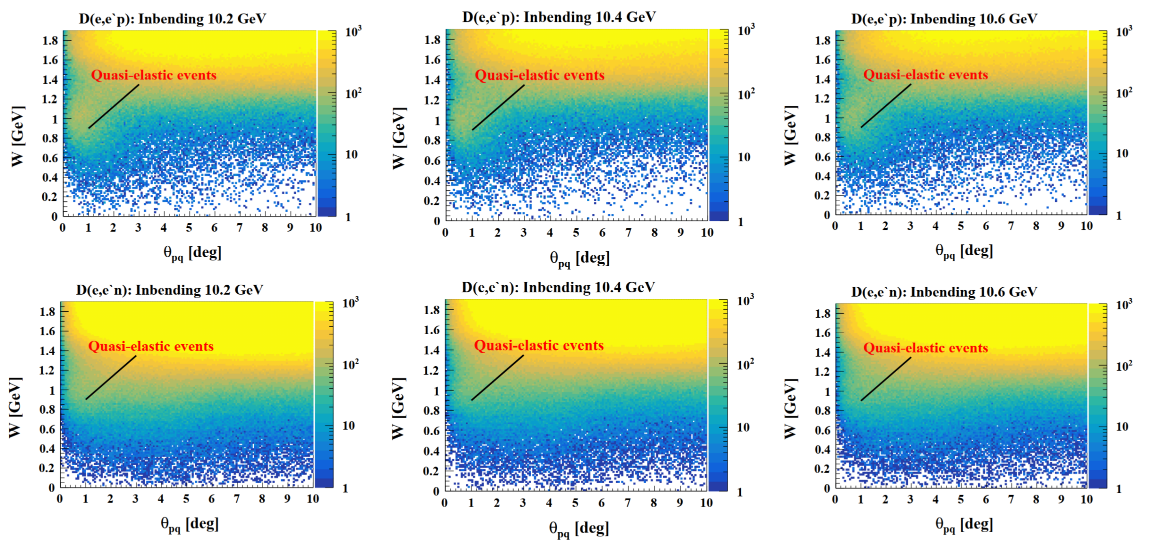

Figure 4.1: The invariant mass W distribution as a function of θ_{pq} for $D(e, e'p)$ (top) and $D(e, e'n)$ (bottom) for each data set.

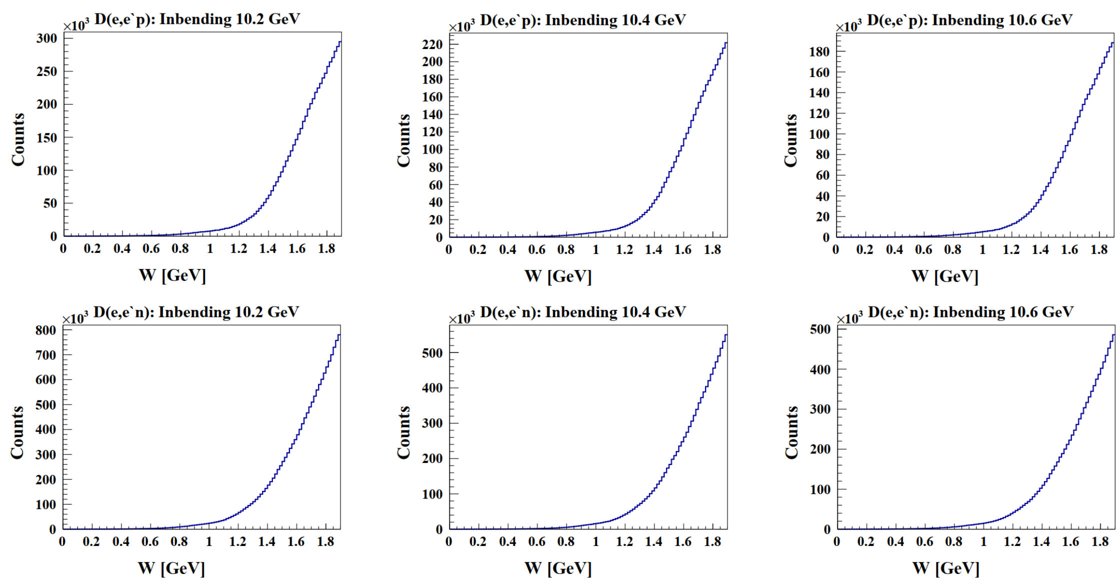

Figure 4.2: The invariant mass W distribution of $D(e, e'p)$ (top) and $D(e, e'n)$ (bottom) for each dataset.

background and make the peak of the proton and neutron masses visible. There are three cuts applied to select quasi-elastic events:

1. Incident electron beam energy cut.
2. $\Delta\phi$ c ut
3. θ_{pq} cut.

rogue space

Below we will discuss each cut in detail.

from the measured events

4.3.1 Incident electron beam energy cut

The incident electron beam energy can be calculated in two different way:

1. $E_{\text{beam}}^{\text{angles}}$: Using the scattering polar angles of the electron and the nucleon, measured by CLAS12 FD, the beam energy is [84]:

$$E_{\text{beam}}^{\text{angles}} = \frac{m_{N'}}{1-\cos\theta_{e'}}\left(\cos\theta_{e'} + \cos\theta_{N'}\frac{\sin\theta_{e'}}{\sin\theta_{N'}} - 1\right). \tag{4.3}$$

define the observables here where they are first introduced instead of in the second equation in this section.

2. $E_{\text{beam}}^{\text{from ele}}$: Using the scattering momentum and polar angle of the electron, measured by CLAS12 FD, the beam energy is [85]:

$$E_{\text{beam}}^{\text{from ele}} = \frac{P_{e'}}{1-2P_{e'}\sin^2(\frac{\theta_{e'}}{2})/m_N}, \tag{4.4}$$

where m_N is the nucleon mass, $\theta_{e'}$, $\theta_{N'}$ are polar angles of scattered electron and nucleon, either proton or neutron, respectively, and $P_{e'}$ is the momentum of the scattered electron.

The correlation between $E_{\text{beam}}^{\text{angles}}$ and $E_{\text{beam}}^{\text{from ele}}$ for events satisfying $\theta_{pq} < 10°$ is shown in Fig. 4.3. It is observed that the quasi-elastic events in the $D(e,e'n)$ channel exhibit a wider spread compared to the $D(e,e'p)$ channel, making it difficult to discern the peak in the $E_{\text{beam}}^{\text{angles}}$ distribution. To address this, a cut is applied on the invariant mass around the known nucleon mass, $0.85 < W < 1.05$ GeV, in order to reduce the inelastic background under the $E_{\text{beam}}^{\text{angles}}$ distribution. Subsequently, quasi-elastic events are selected by applying sector-dependent cuts on the $E_{\text{beam}}^{\text{angles}}$ distribution. Figures 4.4 and 4.5 show the $E_{\text{beam}}^{\text{angles}}$ distributions for $D(e,e'p)$ and $D(e,e'n)$ for each sector, respectively. These distributions satisfied the criteria of $0.85 < W < 1.05$ GeV, and $\theta_{pq} < 10°$ cuts, thereby capturing the peak corresponding to the incident beam energy. The cut used for quasi-elastic selection corresponds to 1 σ on the Gaussian function fit to the central peak.

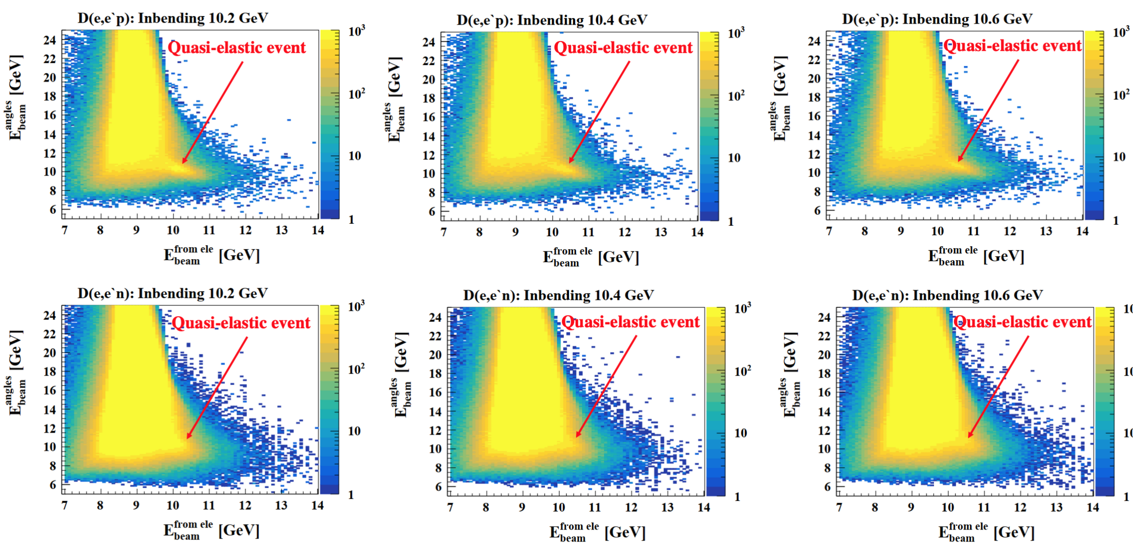

Figure 4.3: The $E_{\text{beam}}^{\text{angles}}$ vs. $E_{\text{beam}}^{\text{from ele}}$ distributions for $D(e, e'p)$ (top) and $D(e, e'n)$ (bottom) that satisfied $\theta_{pq} < 10^{\circ}$ cut for each dataset.

It is expected for quasi-elastic scattering that the particle will lie in or nearly in the same plane.

4.3.2 $\Delta\phi$ Cut

The difference in the lab azimuthal angle between the nucleon and the scattered electron ($\Delta\phi = \phi_{N'} - \phi_{e'}$) is used to select the quasi-elastic events. This particular cut becomes necessary for the $D(e, e'n)$ channel, where some background remains even after applying the incident beam energy cut ($E_{\text{beam}}^{\text{angles}}$), as shown in Fig. 4.6. This background is most likely due to photon contamination. The cut applied corresponds to 1 σ on the Gaussian function fit to the central peak. These cuts are tight in order to select as clean of a sample of quasi-elastic events as possible for $D(e, e'n)$ channel. For consistency, the same cut (1 σ on the Gaussian) is applied for the $D(e, e'p)$ channel.

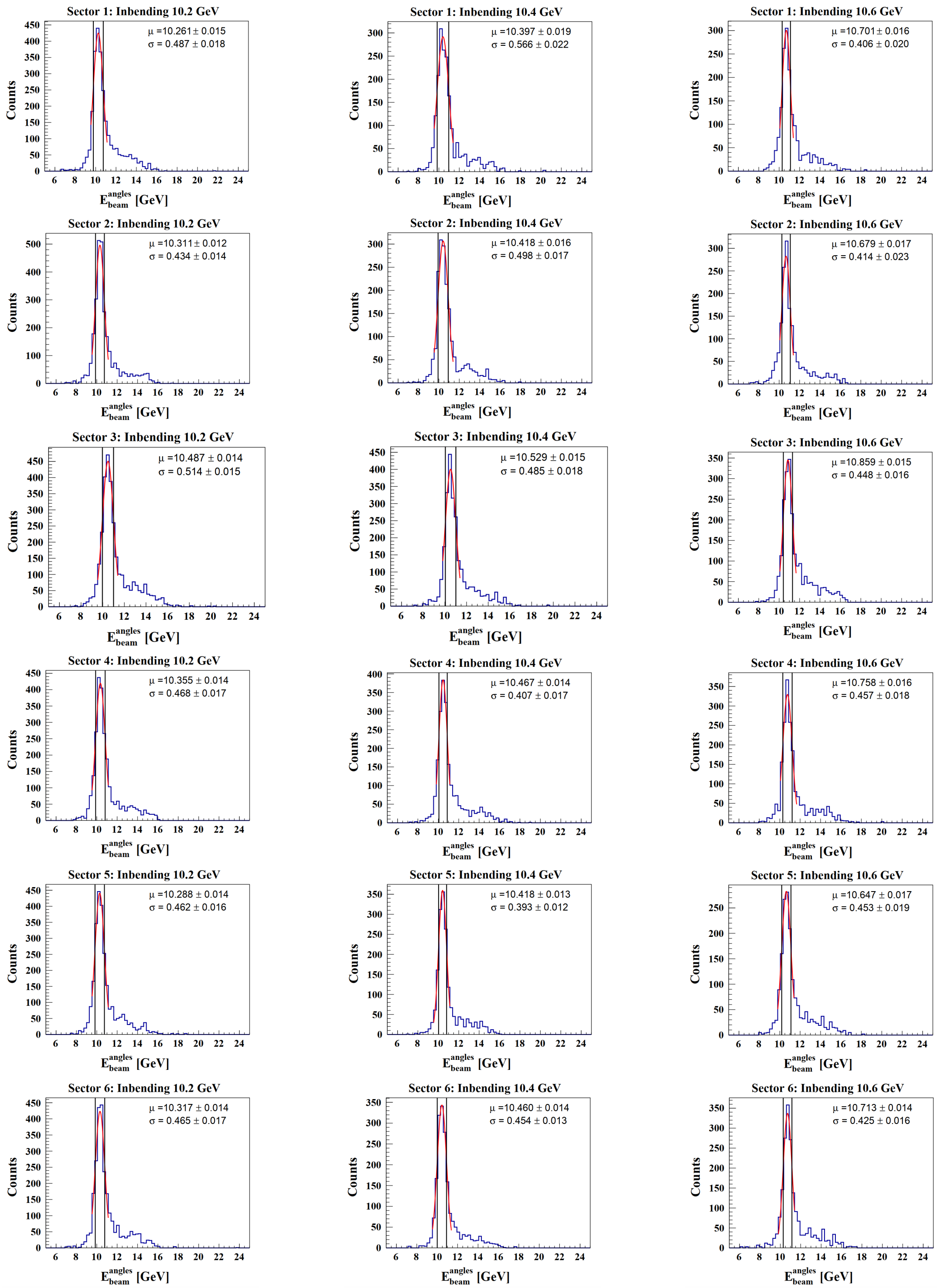

Figure 4.4: The $E_{\text{beam}}^{\text{angles}}$ distributions of $D(e, e'p)$ events that satisfied $0.85 < W < 1.05$ GeV and $\theta_{pq} < 10°$ cut for each sector. The black vertical lines show the cut applied within 1σ.

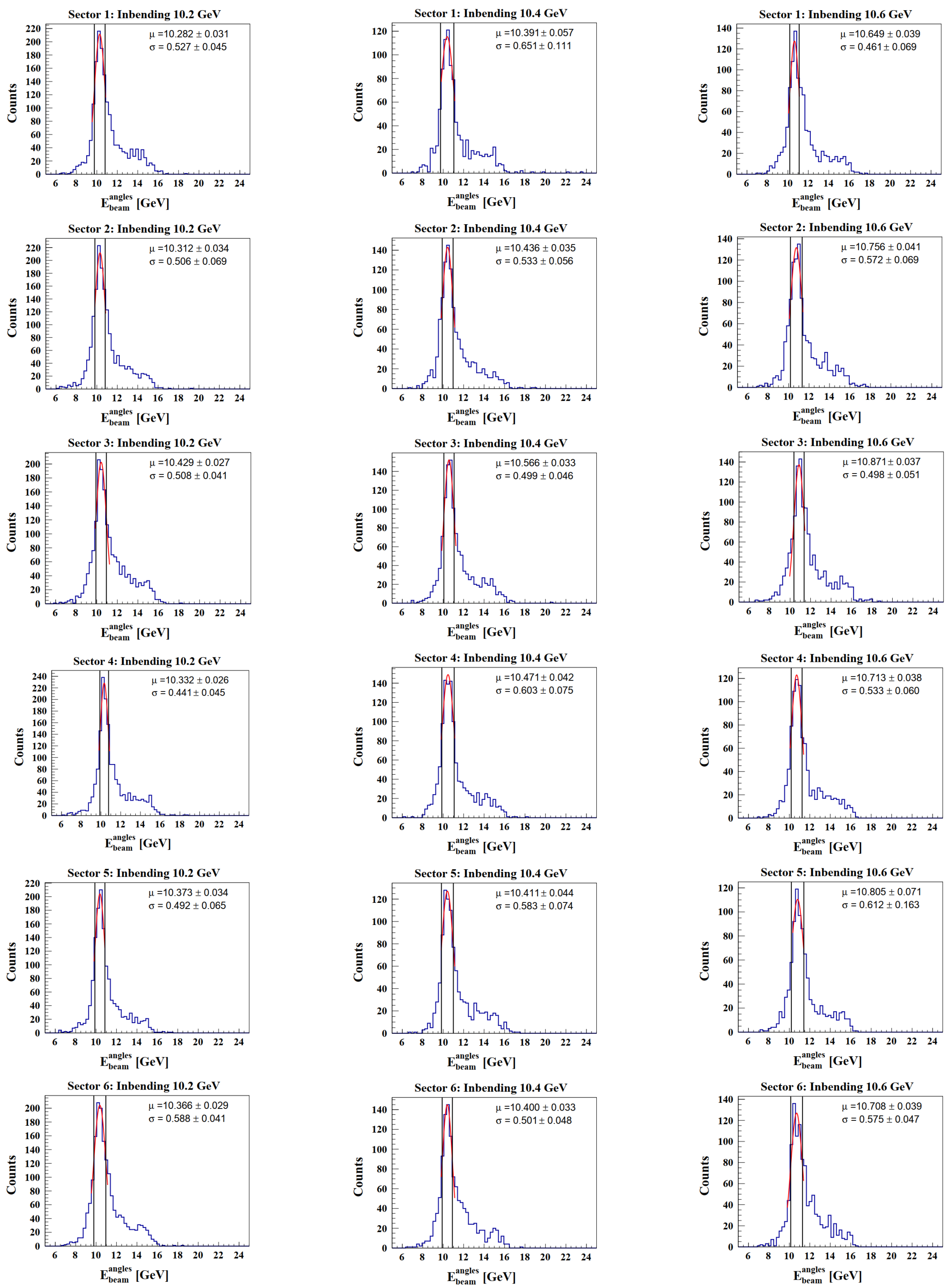

Figure 4.5: The $E_{\text{beam}}^{\text{angles}}$ distributions of $D(e, e'n)$ events that satisfied $0.85 < W < 1.05$ GeV and $\theta_{pq} < 10^\circ$ cut for each sector. The black vertical lines show the cut applied within 1σ.

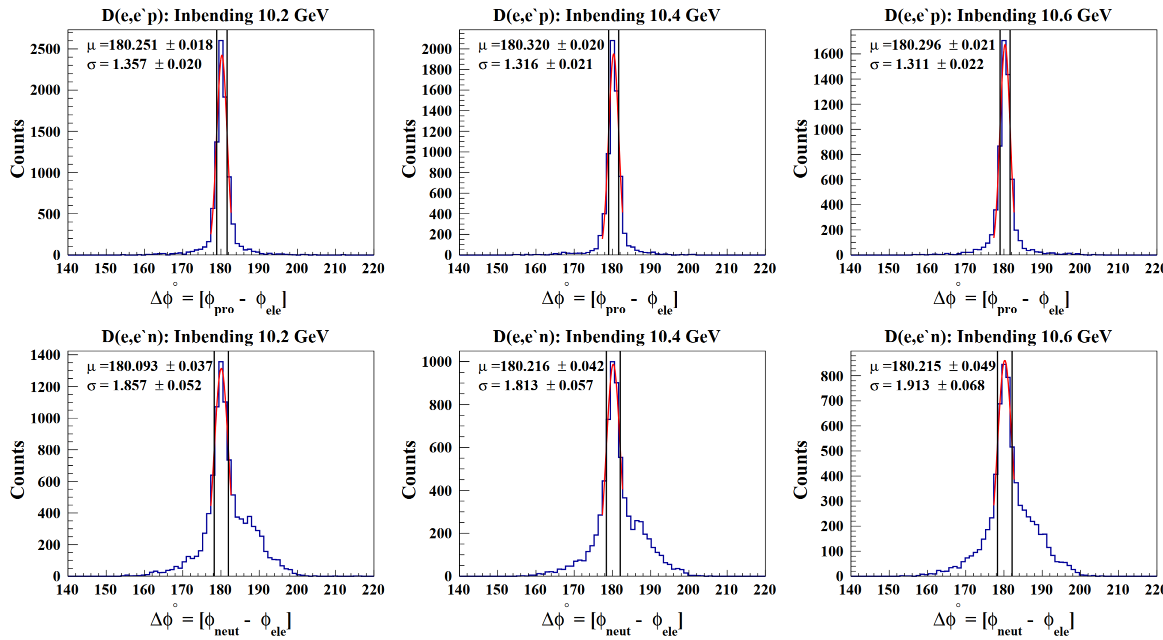

Figure 4.6: The $\Delta\phi$ distributions for events passing cut on $0.85 < W < 1.05$ GeV, $\theta_{pq} < 10°$ and $E_{\text{beam}}^{\text{angles}}$ cuts for $D(e,e'p)$ (top) and $D(e,e'n)$ (bottom) for each datasets. The black vertical lines show the cut applied within 1σ.

4.3.3 θ_{pq} Cut

The distribution of the Q^2 as a function of θ_{pq} for $D(e,e'p)$ and $D(e,e'n)$ events that satisfied $0.85 < W < 1.05$ GeV, $\theta_{pq} < 10°$, $E_{\text{beam}}^{\text{angles}}$ and $\Delta\phi$ cuts are shown in Fig 4.7. The quasi-elastic events depend on the Q^2 value, where the distribution of quasi-elastic events is narrow at higher Q^2 values and becoming broader as the Q^2 range decreases.

To select quasi-elastic events while minimizing background contamination in the absence of the W cut, a function is introduced as follows:

$$f(\theta_{pq}) = 2.5204 + \frac{6.2127}{\theta_{pq}^{0.9003}}, \tag{4.5}$$

This function, defined using the TCut feature of the ROOT data analysis framework, is used as a cut in both $D(e,e'p)$ and $D(e,e'n)$ channels. The cuts applied are

2.0 deg?

Will any of the previous cuts you have applied be varied to determine systematic uncertainties? If yes, that should be mentioned above when you discuss the cuts.

$Q^2 < f(\theta_{pq})$ and $\theta_{pq} < \cancel{1.60^\circ}$ and is shown in Fig. 4.7 as a red curve. It's important to mention that the selection of the $\theta_{pq} < 1.60^\circ$ cut was done visually. However, it should be noted that this cut will be varied during the systematic uncertainty analysis.

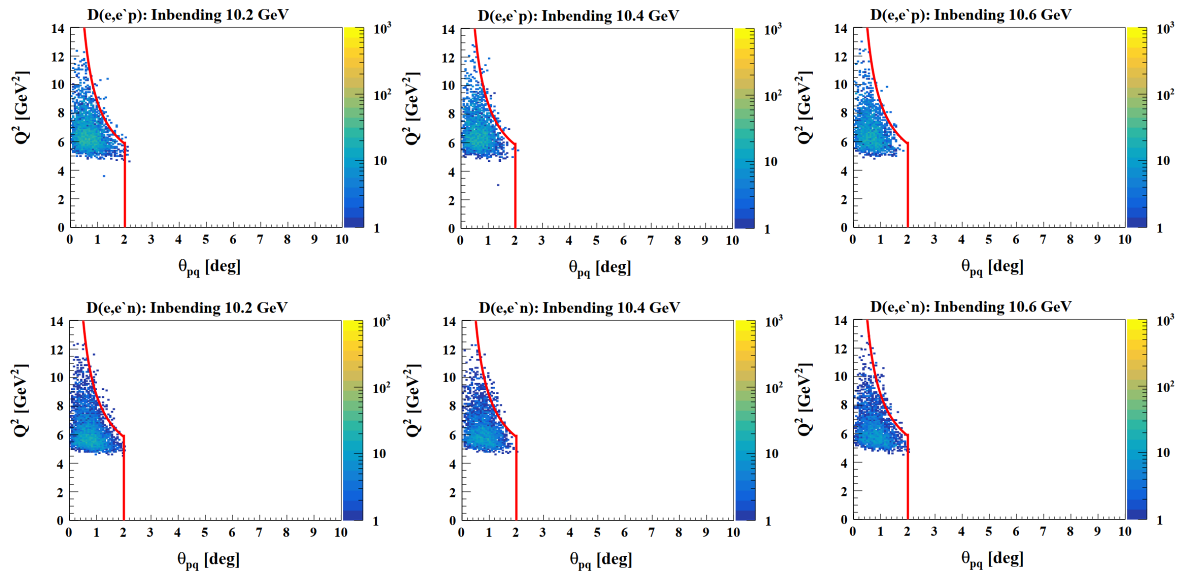

Figure 4.7: The Q^2 as a function of θ_{pq} distribution for $D(e,e'p)$ (top) and $D(e,e'n)$ (bottom) for each datasets that satisfied $0.85 < W < 1.05$ GeV, $E^{\text{angles}}_{\text{beam}}$ and $\Delta\phi$ cuts. The red curve is the cut used to select the quasi-elastic events.

The W distribution of the quasi-elastic events for both $D(e,e'p)$ and $D(e,e'n)$ that satisfied $E^{\text{angles}}_{\text{beam}}$, $\Delta\phi$ and θ_{pq} cuts are shown in Fig 4.8.

You are, I think, using the shape and position of the W2 distribution and the similarity between e-n and e-p events to make the point that you have cleanly extracted the QE events. You should say something like that. Don't assume the reader will be overpowered by the astounding glory of fig. 4.8

To measure the ratio of neutron to proton cross-sections σ_n/σ_p correctly, it is important to account for the geometric acceptance for each cross section. To ensure that both neutrons and protons have the same acceptances, a common fiducial region is required. This can be done by using the acceptance matching technique as shown in Fig. 4.9 and described as follows.

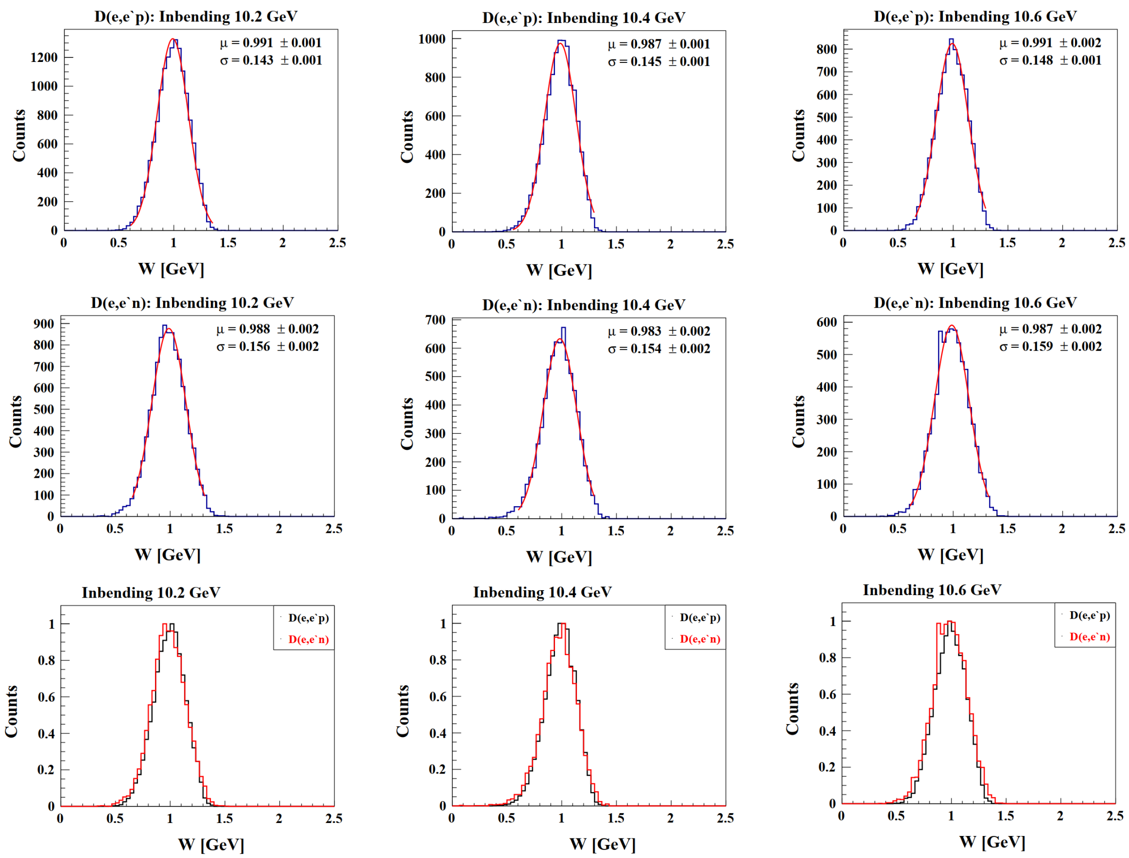

Figure 4.8: The W distribution for $D(e,e'p)$ (top) and $D(e,e'n)$ (middle) for each datasets that satisfied $E_{\text{beam}}^{\text{angles}}$, $\Delta\phi$ and θ_{pq} cuts. The bottom plots shows the comparison between $D(e,e'p)$ and $D(e,e'n)$ channels. The counts are scaled by normalize both $D(e,e'p)$ and $D(e,e'n)$ events.

1. In each event, the expected 3-momentum of the nucleon (either neutron or proton) is determined based on the measured electron kinematics and assuming elastic scattering and nothing else.

2. For each event we start with a good electron and assume the nucleon is a neutron first. Then, we swim it through the CLAS12 detector system by drawing a straight line from the electron vertex in the direction of the expected 3-momentum of the neutron. This path is “swum” through the CLAS12 detector system to see if the track strikes the fiducial volume of the calorimeter. If

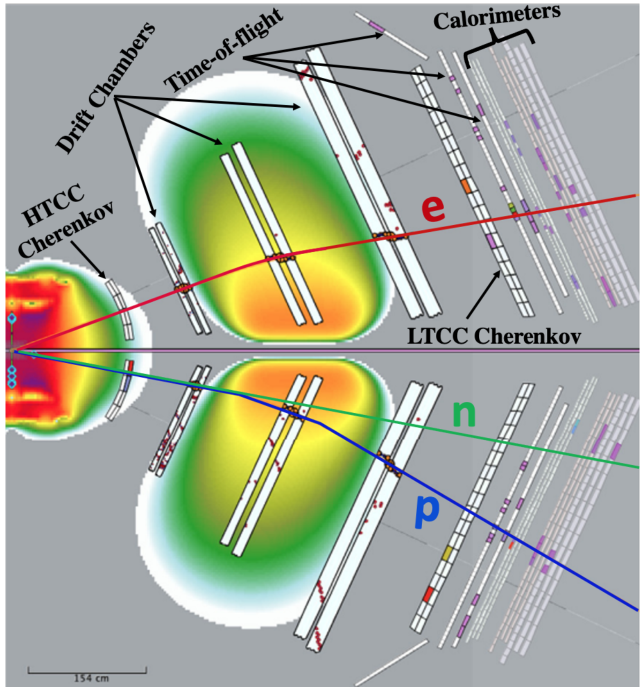

Figure 4.9: Acceptance matching using the "swimming" technique for negative torus polarity "inbending" field, where the electron is bent toward the beam line. By requiring both swimming neutron and swimming proton tracks to hit the calorimeters, the geometric acceptance of $D(e, e'p)$ and $D(e, e'n)$ are equal.

',' needed

it hits the ECAL and is at least 10 cm away from the edge of the calorimeter the analysis continues. If it misses the entire event is dropped.

3. If the event passes step 2 above, we then assume the expected nucleon is a proton. The charged particle track of the proton is "swum" from the electron vertex through the magnetic field of CLAS12 towards the calorimeter. If this charged track also strikes the ECAL fiducial volume and is at least 10 cm away from the edge, the entire event is kept. Otherwise the event is dropped.

The acceptance matching technique described above is performed twice, once for the $D(e, e'p)$ channel and once for the $D(e, e'n)$ channel. The hit position of the swum particles within the fiducial region of the calorimeter is shown in Fig. 4.10 for these channels. The distinct hit positions of protons and neutrons within the fiducial region being

of the calorimeter are due to ~~that~~ the protons ~~are~~ deflected by the magnetic field in the detector, while neutrons are not affected by the magnetic field.

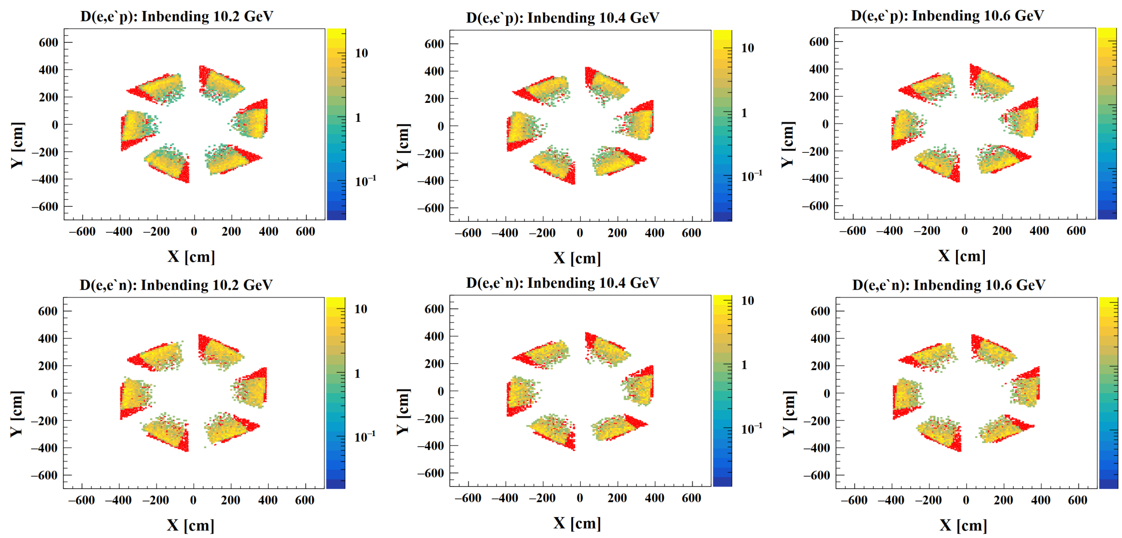

Figure 4.10: The distribution of the swum neutron (yellow points) and swum proton (red points) in the $x-y$ plane of the ECAL for $D(e,e'p)$ (top) and $D(e,e'n)$ (bottom) for each data set.

4.5 Uncorrected Ratio Results

Events that satisfy the quasi-elastic selection cuts and pass acceptance matching are used to fill two histograms, one for neutron events and one for proton events. They are binned in Q^2, and each bin in the histogram contains the count of events (either proton or neutron). The σ_n/σ_p ratio histogram is calculated by dividing each bin in the neutron histogram by the corresponding bin in the proton histogram:

$$R^i_{\text{meas}} = \frac{b^i_{neut}}{b^i_{pro}}, \tag{4.6}$$

where b^i_{neut} and b^i_{pro} are the number of neutron and proton events found in the i^{th} Q^2 bin, respectively. The uncertainty on each bin in the ratio histogram is given by the

define sigma_b^i_neut
and sigma_b^i_pro

propagation of errors formula:

$$\sigma_{R^i_{\text{meas}}} = \sqrt{\left(\frac{\partial R^i_{\text{meas}}}{\partial b^i{}_{neut}}\right)^2 \sigma^2_{b^i{}_{neut}} + \left(\frac{\partial R^i_{\text{meas}}}{\partial b^i{}_{pro}}\right)^2 \sigma^2_{b^i{}_{pro}}}, \tag{4.7}$$

where R^i_{meas} represents the value of the ratio histogram in the i^{th} bin, b_{neut} is the number of neutron entries in that bin, and b_{pro} is the number of proton entries in that bin. Fig. 4.11 shows the σ_n/σ_p ratio histograms from different data sets, showing the consistency of the ratio results at different beam energies.

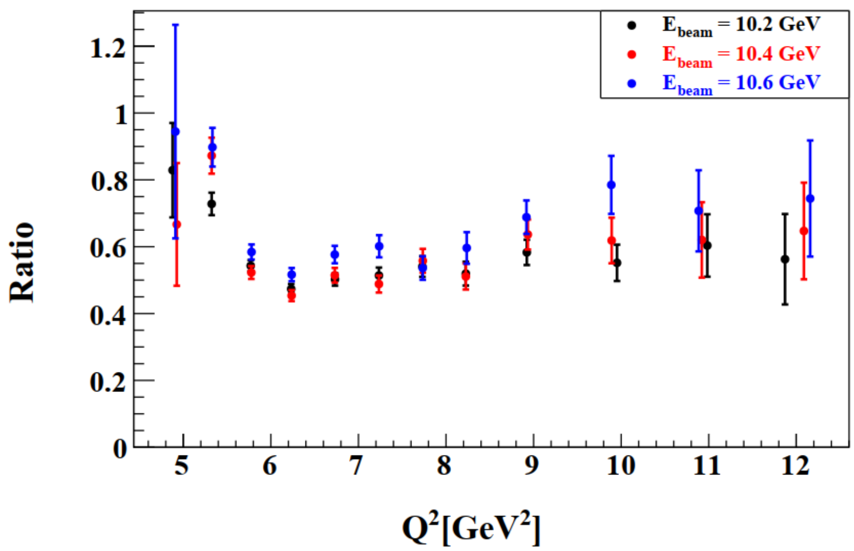

Figure 4.11: The σ_n/σ_p ratio results from different data sets at three different beam energies 10.2, 10.4, and 10.6 GeV binned in Q^2

.

CHAPTER 5

Corrections to Quasi-elastic Ratio

This chapter will discuss the corrections to the ratio measurements. These corrections include neutron efficiency (NDE), Fermi motion and radiative effect.

5.1 NDE corrections to the Ratio

The essential correction to the Ratio is NDE, which is calculated in Chapter 3. To implement the NDE correction, we used the functional form in Eq 3.30, that discussed in Sec. 3.10. At this stage, we used the Crystal Ball parametrization in Table 3.7 due to its ability to fit a higher range of missing mass values. However, it's important to note that the Gaussian parametrization will also be taken into consideration as part of the systematic uncertainty analysis.

The $D(e, e'n)$ events that satisfy both the quasi-elastic selection cuts in Sec 4.3 and pass acceptance matching are used to fill a histogram. This histogram is binned in Q^2 and the entries are weighted by the reciprocal of the neutron detection efficiency calculated from the Crystal Ball function. The R^i_{Cor} ratio histogram is calculated by dividing each bin in the neutron weighted histogram by the corresponding bin in the proton $D(e, e'p)$ histogram:

$$R^i_{\text{Cor}} = \frac{b^i_{neut_w}}{b^i_{pro}}, \tag{5.1}$$

where R^i_{Cor} is the ratio corrected for the NDE in the i^{th} Q^2 bin, $b^i_{neut_w}$ is the efficiency-weighted number of neutron events found in that bin and b^i_{pro} is the number of proton events found in that bin. The uncertainty on each bin in this ratio histogram is given by the propagation of errors formula:

$$\sigma_{R^i_{\text{Cor}}} = \sqrt{\left(\frac{\partial R^i_{\text{Cor}}}{\partial b^i{}_{neut_w}}\right)^2 \sigma^2_{b^i{}_{neut_w}} + \left(\frac{\partial R^i_{\text{Cor}}}{\partial b^i{}_{pro}}\right)^2 \sigma^2_{b^i{}_{pro}}}, \tag{5.2}$$

Fig. 5.1 shows the R^i_{Cor} ratio in each Q^2 bin including NDE correction from different data sets, showing the consistency of the ratio results at different beam energies. The results show that the NDE correction increases the ratio values by approximately 3%.

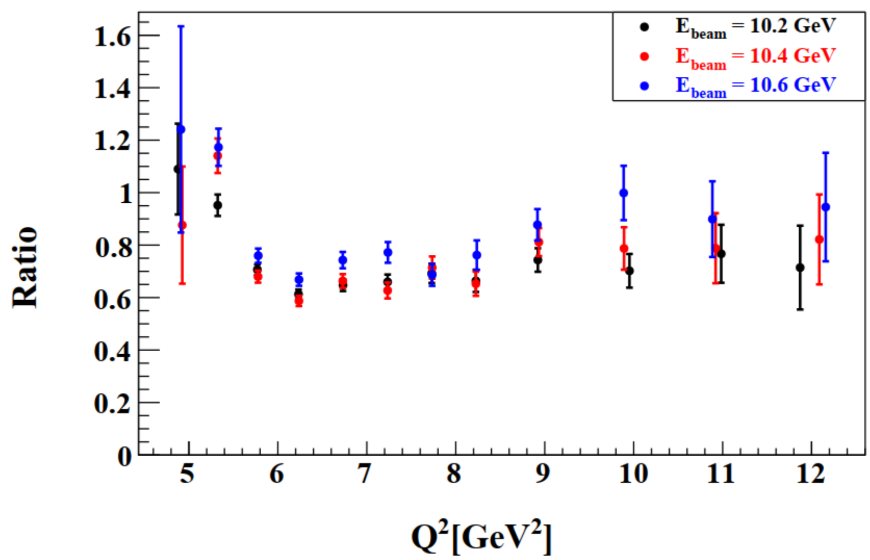

Figure 5.1: The σ_n/σ_p ratio results including NDE correction from different data sets at three different beam energies 10.2, 10.4, and 10.6 GeV binned in Q^2

.

5.2 Correction due to Fermi motion of the target

In experiments where scattering involves a target nucleon in motion, such as in the case of the deuteron, the Fermi motion of nucleons within the deuteron can result in losses or migrations of scattered particles outside the acceptance region of the detector. For instance, if a scattered nucleon is expected to hit near the edge of the detector's acceptance region, the motion of the target nucleon due to Fermi motion may cause the scattered particle to move out of the acceptance region. This can have an impact on the measured σ_n/σ_p ratio. To address and correct for these effects, Monte Carlo simulations are used. These simulations enable the estimation of the fraction of scattered nucleons expected to be removed from the acceptance by Fermi effects.

5.3 Simulating Quasielastic Scattering on Deuterium

The QUasi-Elastic Event Generator (QUEEG) is an event generator developed by J.D.Lachniet and extended by G. Gilfoyle and used for the CLAS6 measurement of the neutron magnetic form factor and the preparations for this experiment. It is designed to simulate quasielastic scattering events in the $D(e,e'p)$ and $D(e,e'n)$ reactions on a deuterium target. In QUEEG, the deuterium target is treated as a composite system composed of two on-shell nucleons. One nucleon acts as a spectator, while the other participates in the elastic scattering with the target nucleon. The generator uses the Hulthen distribution, which is a theoretical model that describes the bound state of the deuterium. QUEEG estimates the effects of Fermi motion, which is the motion of nucleons inside the nucleus. The Fermi-motion distribution inside the deuterium is calculated with the Hulthen distribution, as shown in Figure 5.2. More detail on QUEEG generator can be found in [86].

The quasi-elastic $D(e,e'p)$ and $D(e,e'n)$ events were generated using QUEEG with incident beam energies of 10.2, 10.4, and 10.6 GeV. The events are passed through the GEant4 Monte-Carlo (GEMC) and the CLAS12 reconstruction software for simulation. The GEMC framework uses the GEant4 simulation toolkit for simulating the passage of particles through various materials and the CLAS12 detector components by considering the physical geometry, materials, and response character-

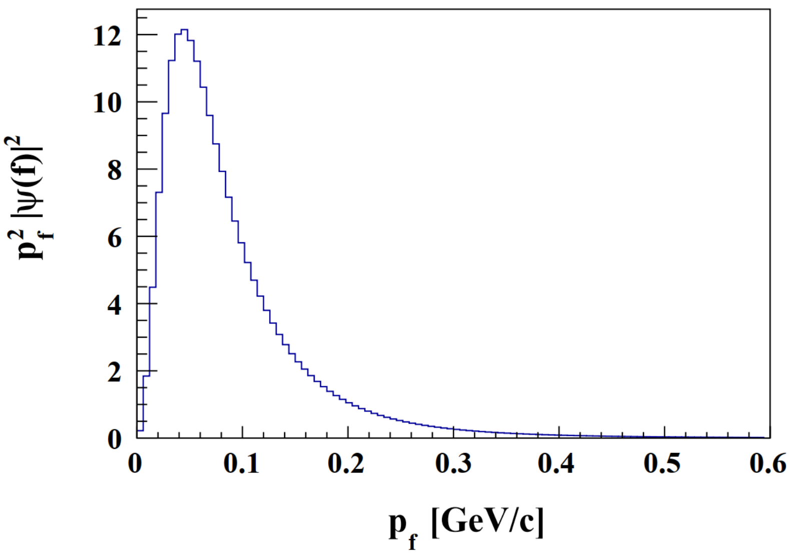

Figure 5.2: Fermi momentum distribution of nucleons inside the deuteron given by Hulthen model.

istics. Three sets of simulations were produced for the in-bending field configuration for the RG-B data set with the incident beam energy of 10.2, 10.4, and 10.6 GeV.

5.3.1 Comparison to Data

The MC data has been analyzed in the same way as the experimental data. All cuts and corrections were made for MC in the same way as the experimental data. The comparison between the experimental data and the simulated events of electron kinematics for the $D(e, e'p)$ and $D(e, e'n)$ is shown in Fig. 5.3 and Fig. 5.4

The comparison between the experimental and the simulated data of the invariant mass W that satisfy the quasi-elastic selection cuts and pass acceptance matching is shown in Fig. 5.5. The counts are scaled by normalize both experimental and simulated data. Good agreement of the W between Monte Carlo and data is found for each dataset.

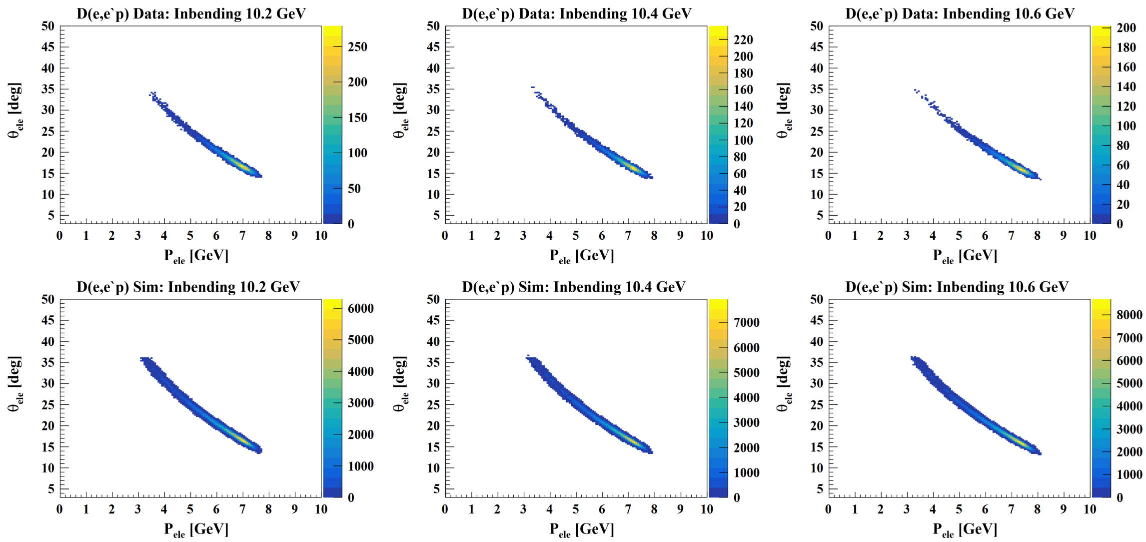

Figure 5.3: The polar angle of the reconstructed electron as a function of the momentum of electron for $D(e, e'p)$ quasi-elastic events for each data set. Top row is the data and bottom is the simulation.

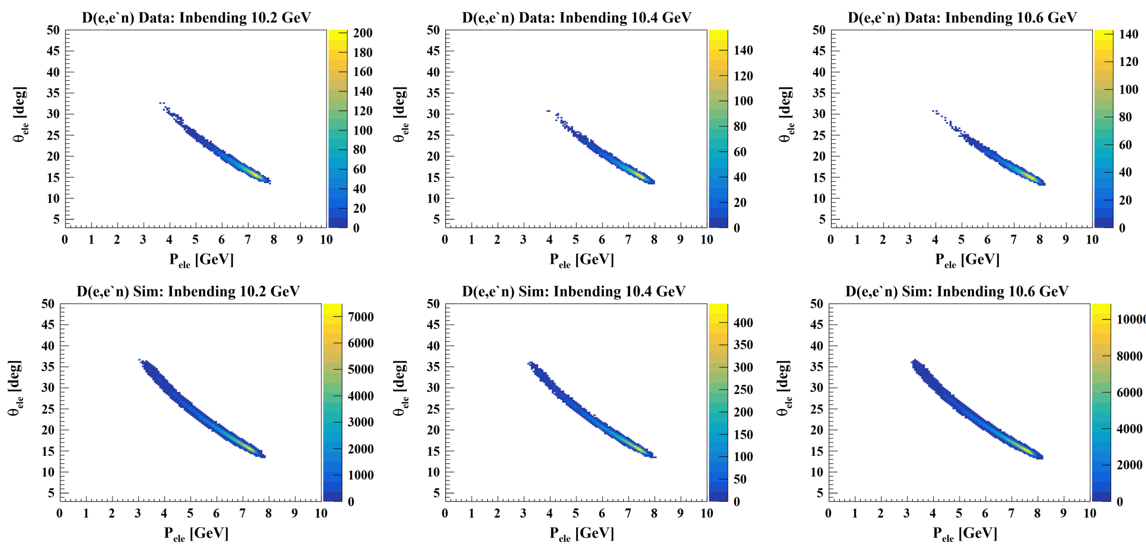

Figure 5.4: The polar angle of reconstructed electron as a function of the momentum of electron for $D(e, e'n)$ quasi-elastic events for each data set. Top row is the data and bottom is the simulation.

5.4 Fermi-Loss Correction to the Ratio

The correction for the effects of Fermi loss in the R^i_{meas} ratio histogram is determined by filling two histograms. The first histogram consists of events where the nucleon

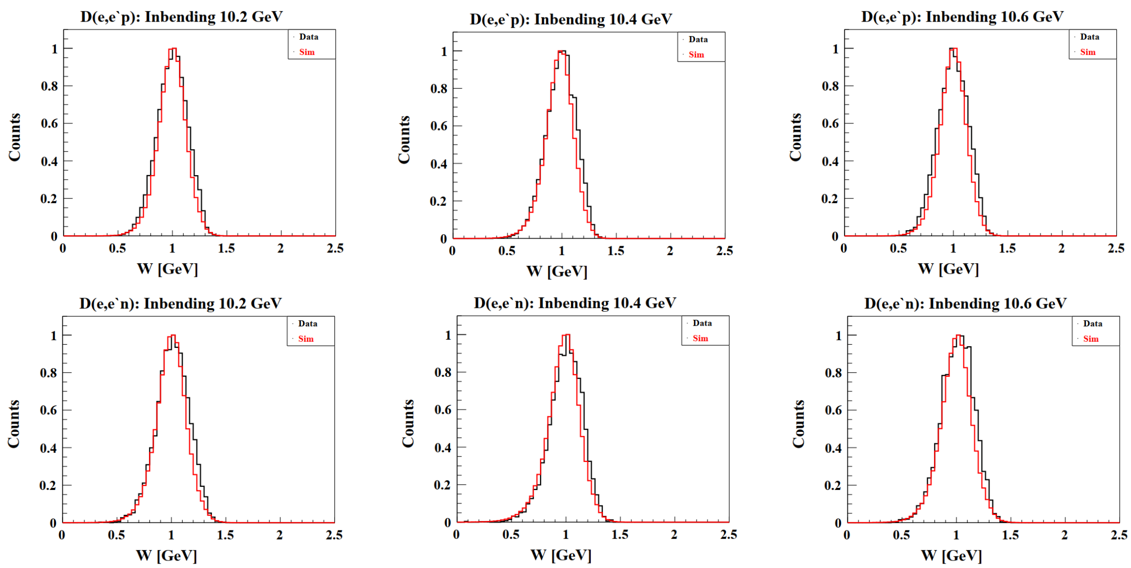

Figure 5.5: The W distribution for $D(e,e'p)$ (top) and $D(e,e'n)$ (bottom) for both experimental (black) and simulated (red) data that satisfied the quasi-elastic selection cuts and pass acceptance matching. The counts are scaled by normalize both experimental and simulated data. The comparison is shown for incident beam energy 10.2, 10.4 and 10.6 GeV.

is expected to be found inside the acceptance of the PCAL/ECAL detector. The expected nucleon location is determined using only the kinematic information of the scattered electron (this is the only available information in real data) and assuming elastic scattering off a stationary target. The second histogram consists of events where the scattered nucleon is actually found inside the acceptance of the PCAL/ECAL detector and satisfies the θ_{pq} cuts described in Sec. 4.3.3. This determination uses the information about the scattered nucleon's momentum from the event generator, which is not available in real data. The ratio of these two histograms provides the fraction of nucleons that are lost due to the effects of Fermi motion, which moves the scattered nucleons outside the acceptance. The loss factor is calculated separately for neutrons and protons as a function of Q^2 and shown in Fig. 5.6.

I still claim this ratio is actually the fraction that are found despite the Fermi motion and so dividing the measured number of nucleons by this fraction corrects for the loss due to the Fermi motion.

To correct for the Fermi loss effects, each Q^2 bin in the R^i_{meas} ratio histogram is multiplied by the corresponding correction factor determined from the Fermi loss

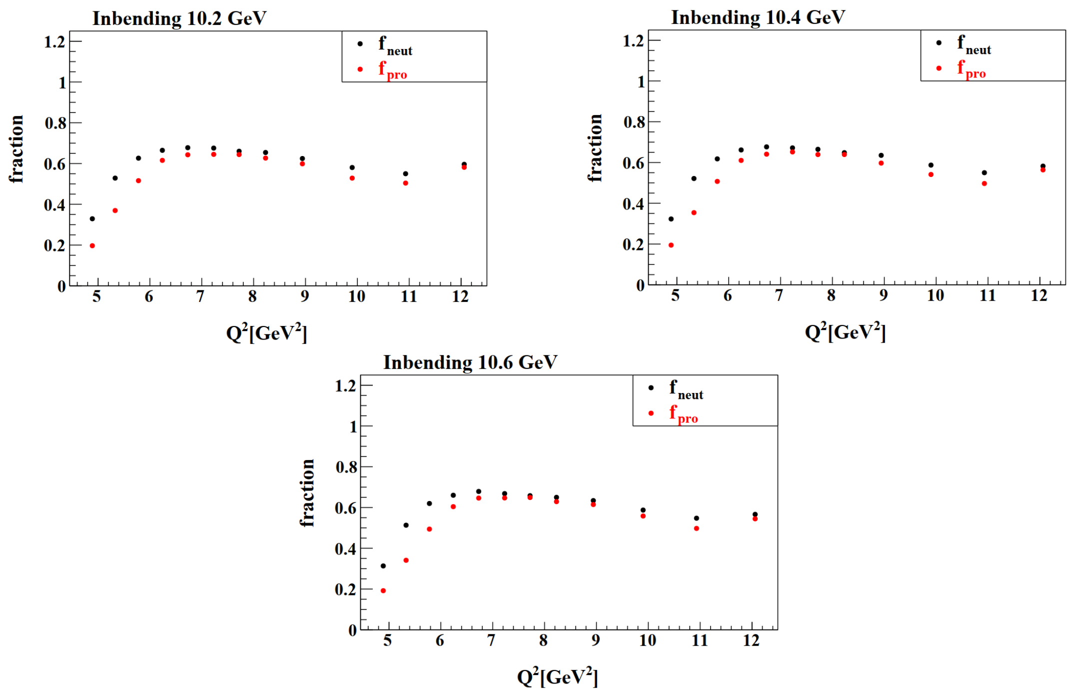

Figure 5.6: The fraction of nucleons scattered at different Q^2 bins, which scattered into the PCAL/ECAL acceptance and satisfied the θ_{pq} cuts and acceptance matching, has been determined using the simulation. The black points on the plot represent the neutron fraction, while the red points represent the proton fraction. These points were generated using an incident beam energy of 10.2, 10.4 and 10.6 GeV.

histograms:

$$R_{\text{Cor}}(Q^2) = \frac{f_{\text{pro}}(Q^2)}{f_{\text{neut}}(Q^2)} R_{\text{meas}}(Q^2) = f_{fermi}(Q^2) R_{\text{meas}}(Q^2), \tag{5.3}$$

where f_{pro}, f_{neut} are taken from the histograms in Fig. 5.6. The correction factor for the R^i_{meas} ratio, which is $f_{fermi}(Q^2) = \frac{f_{\text{pro}}(Q^2)}{f_{\text{neut}}(Q^2)}$ is shown in Fig. 5.7 for the three different beam energy 10.2, 10.4 and 10.6 GeV. It's close to 1.0 above 6 GeV and its the same for all data sets.

The impact of applying Fermi loss corrections on the R^i_{meas} ratio histograms is shown in Figure 5.8 for each dataset. The results indicate that the Fermi correction leads to an increase in the ratio by around $2-5\%$ for Q^2 values above 6 GeV^2, while for values below 6 GeV^2, the effect varies significantly, ranging from 10% to 35%.

Need a bit more here. List all the corrections on fig 5.8 in the text (I know they are in the caption, but should be listed here too). Also, when I compare the Q2=6.2 GeV2 point in Fig 5.1 with the same point in fig 5.8 the ratio goes down in 5.8 by 5-10% not up.

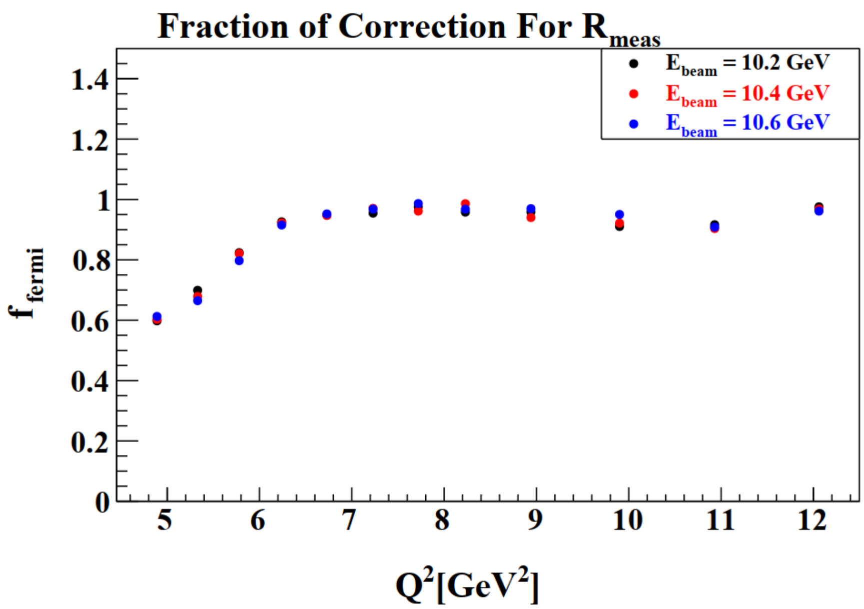

Figure 5.7: The correction factor to the σ_n/σ_p ratio for Fermi loss in the PCAL/ECAL has been determined for the 10.2, 10.4 and 10.6 GeV data.

Include the definition of the correction = f_proton/f_neutron in the caption.

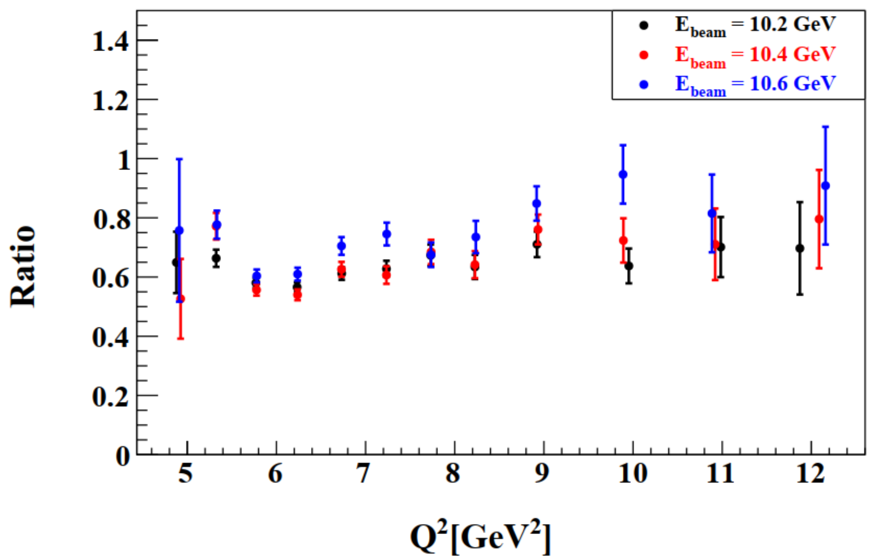

Figure 5.8: The σ_n/σ_p ratio results including NDE and Fermi correction from different data sets at three different beam energies 10.2, 10.4, and 10.6 GeV binned in Q^2

.

5.5 Radiative correction

The cross section measurements are commonly approximated as purely one-photon exchange which is known as Born scattering. However, ~~in reality,~~ there are other processes that effect the total measured cross sections. The electron in particular can emit photons when it is accelerated in the field of the target. Photons can be emitted before or after the collisions and alter the final, detected electron energy. This effect on R^i_{meas} is considered here. The Feynman diagrams of the radiative effects for the electron and nucleon are shown in Fig. 5.9. These diagrams illustrate the following radiative processes that are present in the measured events:

- the Bremsstrahlung, in which the photon is emitted by the incoming or outgoing electron (nucleon), Fig. 5.9 b).
- the vertex correction, in which the photon is emitted by the incoming electron and absorbed by the outgoing electron (nucleon), Fig. 5.9 c).
- the vacuum polarization, in which the virtual photon produces temporarily an e^+e^- pair, Fig. 5.9 d).

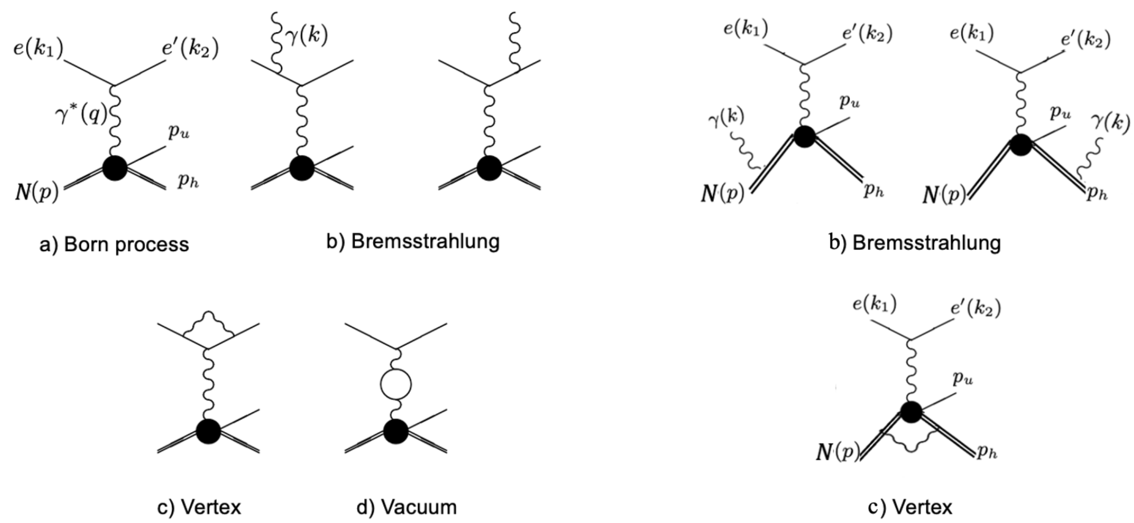

Figure 5.9: Feynman diagrams for Born term and lowest order radiative processes for the electron (left) and the nucleon (right). The p_h and p_u are the the momentum of the detected and undetected hadron, respectively.

Including these other processes in

done

The ~~radiated~~ cross section can be ~~obtained~~ by multiplying the Born cross section by a radiative correction factor:

$$\frac{d\sigma}{d\Omega} = (1+\delta)\left(\frac{d\sigma}{d\Omega}\right)_{Born}, \tag{5.4}$$

where $\left(\frac{d\sigma}{d\Omega}\right)_{Born}$ is the single-photon-exchange cross-section in Eq. 1.11, and the radiative correction factor $(1+\delta)$ comes from the bremsstrahlung, vacuum polarization and vertex corrections.

The radiative corrections (RC) for G_M^n were calculated by the program EXCLURAD. The EXCLURAD program is written by A. Afanasev [87] for exclusive pion electro-production $p(e,e'\pi^+)n$, and it has been further modified by G. Gilfoyle [88] to include the radiative effects in the $D(e,e'p)n$ and $D(e,e'n)p$ channels. The response functions at the deuteron-virtual photon vertex, which describe the deuteron's response to the virtual photon, were calculated by W. Van Orden [89] and incorporated into the code. The EXCLURAD code contains the radiative correction for the electron only which is shown in the left of Fig. 5.9 and does not take into account the nucleon's radiative correction or the two-photon exchange.

The EXCLURAD code is used to generate the ratio of the radiated cross section to the cross section that would be measured if there were no radiative effects for specific kinematic variables. These variables include Q^2 (the square of the four-momentum transfer), W (the invariant mass of the hadronic final state), $\cos\theta_{pq}$ (the cosine of the polar angle between the virtual photon direction and the direction of the detected hadron), and ϕ_{pq} (the azimuthal angle between these directions).

The EXCLURAD code calculates the radiative correction factor for different values of Q^2 as functions of $\cos\theta_{pq}$ and ϕ_{pq}. These surfaces represent the dependence of the radiative correction factor on the angles $\cos\theta_{pq}$ and ϕ_{pq}. To obtain the overall radiative correction factor at a specific Q^2 value, the generated surface is integrated over the experimental range of $\cos\theta_{pq}$ for that particular Q^2 value. The calculation is performed twice, once for the proton detection, $D(e, e'p)n$, channel and once for the neutron detection, $D(e, e'n)p$, channel. Figures 5.10, 5.11, and 5.12 show the comparison of the radiative corrections factor for $D(e, e'p)n$ (red curve) and $D(e, e'n)p$ (green curve) channels at $W = 2.60$ GeV, $\cos\theta_{pq} = 0.998°$ at different Q^2 values for the 10.2 GeV, 10.4 GeV and 10.6 GeV data sets, respectively. There is a significant factor of correction in each $D(e, e'p)n$ and $D(e, e'n)p$ channel. However, the curves are close to each other and the difference between them is very small over all range of the ϕ_{pq} values.

In the G_M^n measurement we are interested in the ratio of $D(e, e'p)n$ to $D(e, e'n)p$ corrections:

$$f_{rad}(Q^2) = \frac{1 + \delta_p(Q^2)}{1 + \delta_n(Q^2} = \frac{\text{RC}_p}{\text{RC}_n}, \tag{5.5}$$

where the subscripts (n, p) indicate the neutron and proton, respectively. Figure 5.13 shows the ratio of radiative corrections (f_{rad}), RCp to RCn, at various Q^2 values for the 10.2 GeV, 10.4 GeV, and 10.6 GeV data sets. This ratio varies from 1.0 by approximately 0.20% on average at low ϕ_{pq} values to 0.35% on average at high ϕ_{pq} values at each Q^2 bin. The differences between the smallest and the largest of the ratio of radiative corrections at each value of Q^2 in Fig. 5.13 will be considered as a systematic uncertainty.

To apply radiative corrections to the R^i_{meas} measurement, we used the average radiative correction over ϕ_{pq} values at each Q^2 point ($R_{cor} = f_{rad} \times R^i_{\text{meas}}$). The average radiative correction factors for RCp and RCn and the ratio of the average radiative correction f_{rad} over the ϕ_{pq} values at each Q^2 point for the 10.2 GeV, 10.4 GeV, and 10.6 GeV data sets are shown in Table 5.1. The radiative correction applied to the R^i_{meas} ratio measurement is shown in Fig. 5.14 for the three different beam energies (10.2, 10.4, and 10.6 GeV). These results show that the radiative correction does not significantly impact the ratio measurements.

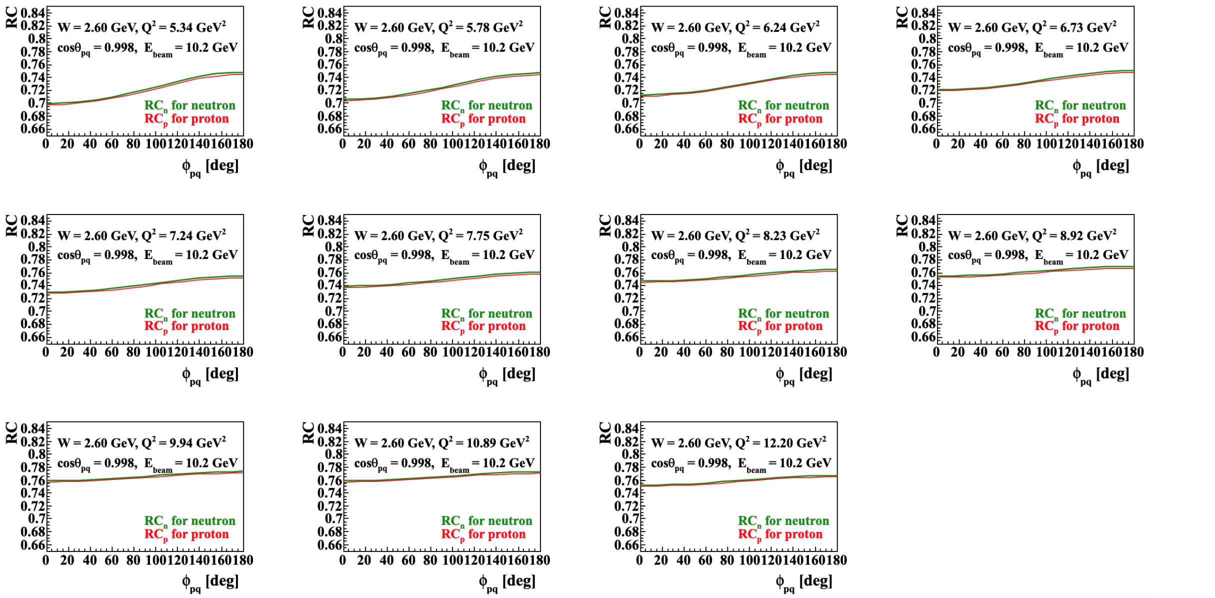

Figure 5.10: A comparison of the radiative correction factor for $D(e, e'p)n$ (red curve) and $D(e, e'n)p$ (green curve) as a function of ϕ_{pq}. The curves shown were generated for a beam energy of 10.2 GeV and $W = 2.60$ GeV at different Q^2 values.

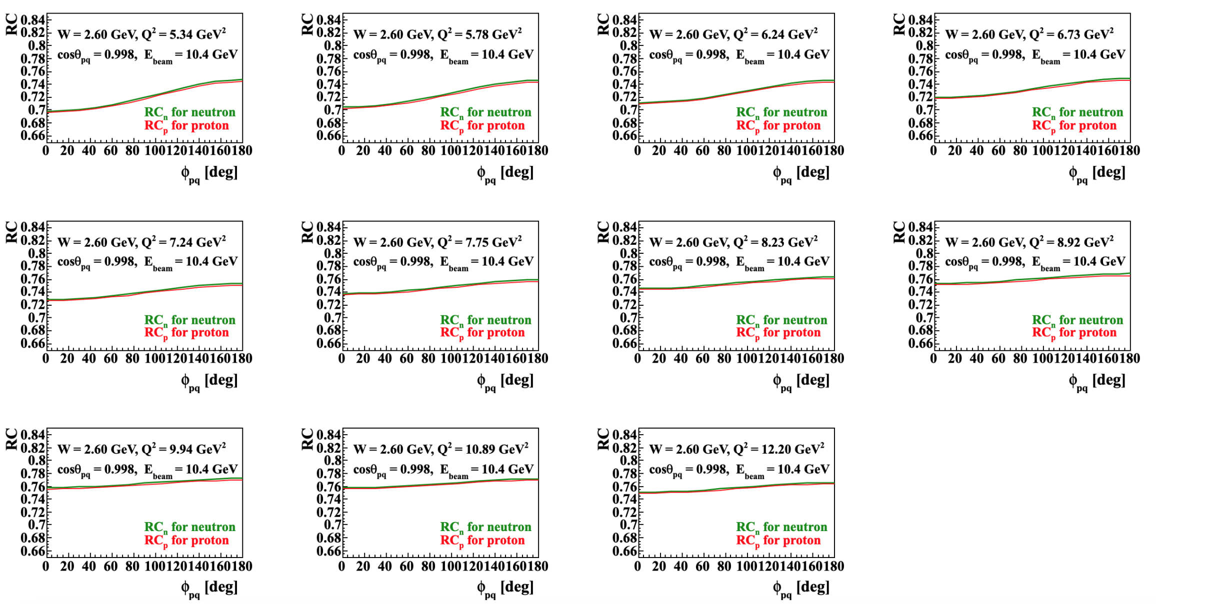

Figure 5.11: A comparison of the radiative correction factor for $D(e, e'p)n$ (red curve) and $D(e, e'n)p$ (green curve) as a function of ϕ_{pq}. The curves shown were generated for a beam energy of 10.4 GeV and $W = 2.60$ GeV at different Q^2 values.

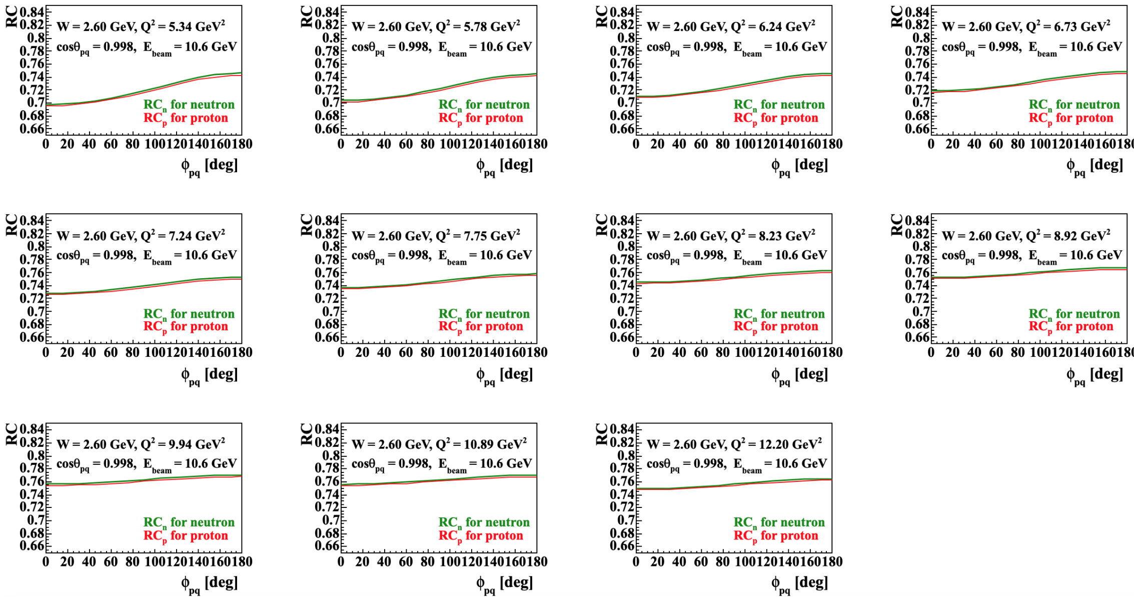

Figure 5.12: A comparison of the radiative correction factor for $D(e,e'p)n$ (red curve) and $D(e,e'n)p$ (green curve) as a function of ϕ_{pq}. The curves shown were generated for a beam energy of 10.6 GeV and $W = 2.60$ GeV at different Q^2 values.

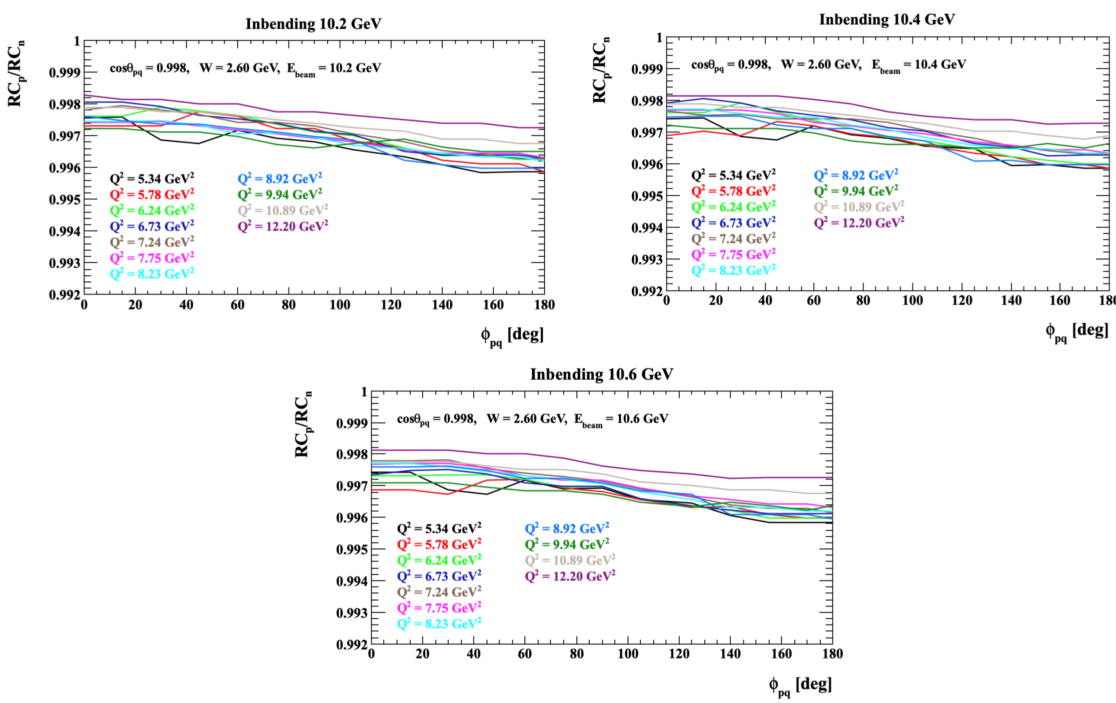

Figure 5.13: The ratio of the radiative correction of $D(e,e'p)n$ to $D(e,e'n)p$ at different Q^2 values for 10.2 GeV (top left), 10.4 GeV (top right) and 10.6 GeV (bottom middle). The average over the ϕ_{pq} values of these radiative correction are used to correct the ratio measurement in each Q^2 point.

Q^2 GeV^2	Inbending 10.2 GeV			Inbending 10.4 GeV			Inbending 10.6 GeV		
	RC$_p$	RC$_n$	f_{rad}	RC$_p$	RC$_n$	f_{rad}	RC$_p$	RC$_n$	f_{rad}
5.34	0.7205	0.7230	0.9966	0.7193	0.7218	0.9966	0.7181	0.7206	0.9966
5.78	0.7236	0.7259	0.9969	0.7222	0.7246	0.9966	0.7210	0.7234	0.9966
6.24	0.7277	0.7299	0.9971	0.7263	0.7286	0.9969	0.7250	0.7274	0.9967
6.73	0.7333	0.7354	0.9971	0.7320	0.7341	0.9971	0.7305	0.7328	0.9968
7.24	0.7402	0.7423	0.9971	0.7389	0.7411	0.9970	0.7376	0.7398	0.9970
7.75	0.7474	0.7497	0.9969	0.7462	0.7484	0.9970	0.7449	0.7471	0.9971
8.23	0.7537	0.7561	0.9969	0.7525	0.7548	0.9970	0.7512	0.7535	0.9970
8.92	0.7601	0.7625	0.9968	0.7587	0.7612	0.9967	0.7575	0.7599	0.9969
9.94	0.7638	0.7663	0.9968	0.7624	0.7649	0.9968	0.7610	0.7635	0.9967
10.89	0.7638	0.7659	0.9974	0.7624	0.7645	0.9973	0.76105	0.7631	0.9973
12.20	0.7578	0.7595	0.9977	0.7563	0.7581	0.9977	0.7549	0.7567	0.9977

Table 5.1: The average radiative correction values for 10.2, 10.4 and 10.6 GeV data set. These values are used to correct the ratio measurement in each Q^2 bin.

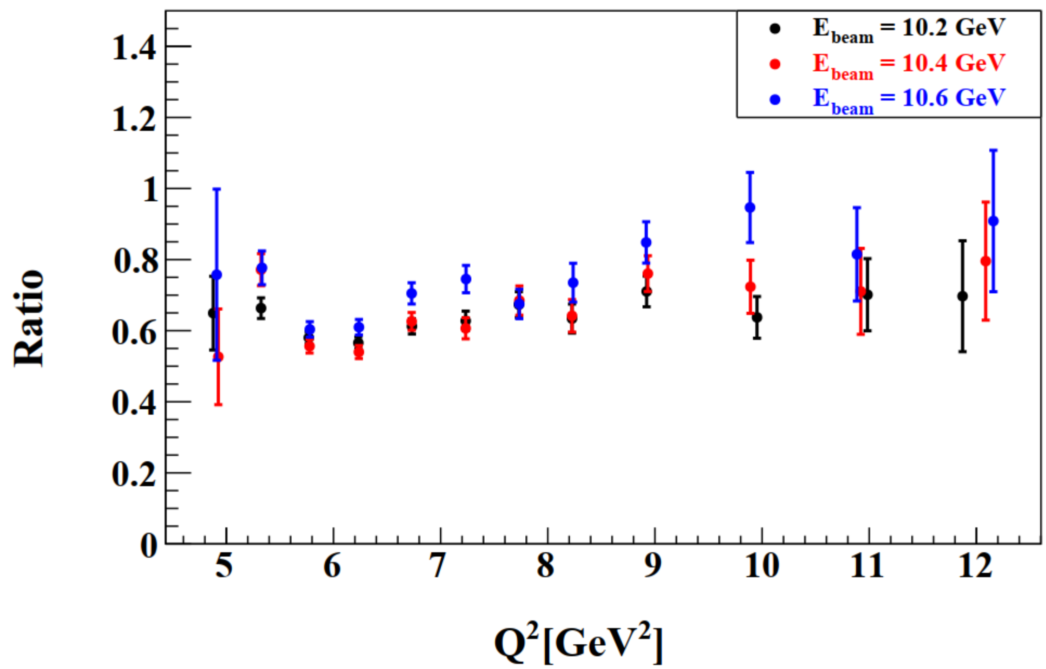

Figure 5.14: The σ_n/σ_p ratio results including NDE, Fermi and radiative corrections from different data sets at three different beam energies 10.2, 10.4, and 10.6 GeV binned in Q^2

.

CHAPTER 6

G_M^n Results

In this chapter, we will extract G_M^n from the ratio of quasi-elastic $D(e,e'p)$ to $D(e,e'n)$ scattering. Then we will discuss the sources of systematic uncertainties that might impact the accuracy of the G_M^n result.

6.1 G_M^n Extraction from Ratio

To extract the neutron magnetic form factor (G_M^n) from the ratio of $D(e,e'n)$ to $D(e,e'p)$ scattering, we begin with the cross-section expression in Eq. 1.11:

$$\frac{d\sigma}{d\Omega} = \sigma_{Mott}\left(G_E^2 + \frac{\tau}{\epsilon}G_M^2\right)\left(\frac{1}{1+\tau}\right), \tag{6.1}$$

where ε and τ are defined as:

$$\varepsilon = \frac{1}{1+2(1+\tau)\tan^2(\frac{\theta_e}{2})} \quad \text{and} \quad \tau = \frac{Q^2}{4M^2}. \tag{6.2}$$

The measured ratio R_{meas} is given by:

$$R_{\text{meas}} = \frac{\frac{d\sigma}{d\Omega}[D(e,e'n)]}{\frac{d\sigma}{d\Omega}[D(e,e'p)]} = \frac{\sigma_{Mott}^n\left({G_E^n}^2 + \frac{\tau_n}{\epsilon_n}{G_M^n}^2\right)\left(\frac{1}{1+\tau_n}\right)}{\sigma_{Mott}^p\left({G_E^p}^2 + \frac{\tau_p}{\epsilon_p}{G_M^p}^2\right)\left(\frac{1}{1+\tau_p}\right)}, \tag{6.3}$$

where the sub-/super-scripts p and n refer to protons and neutrons, respectively. Solving Eq. 6.3 for G_M^n leads to:

$$G_M^n = \pm\sqrt{\left[R_{cor}\left(\frac{\sigma_{mott}^p}{\sigma_{mott}^n}\right)\left(\frac{1+\tau_n}{1+\tau_p}\right)\left({G_E^p}^2 + \frac{\tau_p}{\varepsilon_p}{G_M^p}^2\right) - {G_E^n}^2\right]\frac{\varepsilon_n}{\tau_n}}, \tag{6.4}$$

Where R_{cor} takes into account various corrections including neutron detection efficiency (NDE), proton detection efficiency (PDE), nuclear, Fermi, and radiative corrections

$$R_{cor}(Q^2) = f_{NDE}(Q^2)\, f_{PDE}\,(Q^2)\, f_{Nuclear}(Q^2)\, f_{Fermi}(Q^2)\, f_{Radiative}(Q^2)\, R_{\mathrm{meas}}(Q^2). \tag{6.5}$$

At this stage, the proton detection efficiency correction and the nuclear correction have not been included.

To simplify Eq. 6.4, we make approximations:

We should do some calculations of these ratios to have some idea of how big the approximation is.

$$\frac{\sigma^p_{mott}}{\sigma^n_{mott}} \approx 1, \qquad \frac{1+\tau_n}{1+\tau_p} \approx 1. \tag{6.6}$$

Thus, the neutron magnetic form factor G^n_M becomes:

$$G^n_M = \sqrt{\left[\left({G^p_E}^2 + \frac{\tau_p}{\varepsilon_p}{G^p_M}^2\right)\, R_{cor} - {G^n_E}^2\right]\frac{\varepsilon_n}{\tau_n}} = \sqrt{\left[\sigma_R\, R_{cor} - {G^n_E}^2\right]\frac{\varepsilon_n}{\tau_n}}, \tag{6.7}$$

where $\sigma_R = {G^p_E}^2 + \frac{\tau_p}{\varepsilon_p}{G^p_M}^2$ represents the reduced proton cross section. The standard propagation of errors for the extracted value of G^n_M is determined as:

$$(\delta G^n_M)^2 = \left(\frac{\partial G^n_M}{\partial \sigma_p}\right)^2 (\delta\sigma_p)^2 + \left(\frac{\partial G^n_M}{\partial R_{cor}}\right)^2 (\delta R_{cor})^2 + \left(\frac{\partial G^n_M}{\partial G^n_E}\right)^2 (\delta G^n_E)^2 \tag{6.8}$$

should this be sigma_R? sigma_p not in eq 6.7

To extract G^n_M, the Arrington parametrization [90] is used to calculate the proton form factors (G^p_E and G^p_M) as well as the neutron electric form factor G^n_E. This parametrization is shown in Fig 6.1 as black solid curves. The details of the fit function and the procedure of the fitting that Arrington used can be found in [90]. The Arrington parametrization of G^p_E, G^p_M and G^n_E that we used to extract G^n_M is shown in Fig 6.2.

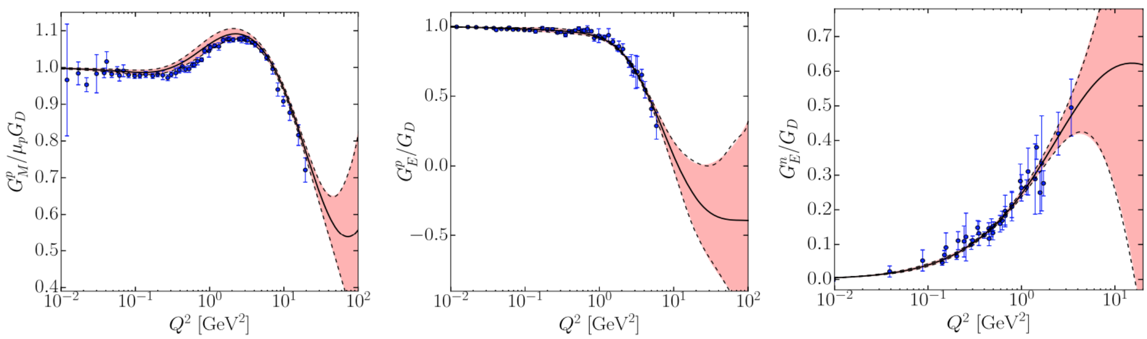

Figure 6.1: Arrington Parameterizations of $G_M^p/\mu_p G_D$ (left), G_E^p/G_D (middle) and $G_E^n/\mu_n G_D$ (right) show as black solid curves. The dashed curves are uncertainty that we used in the G_M^n calculation. The plot from Ref. [90].

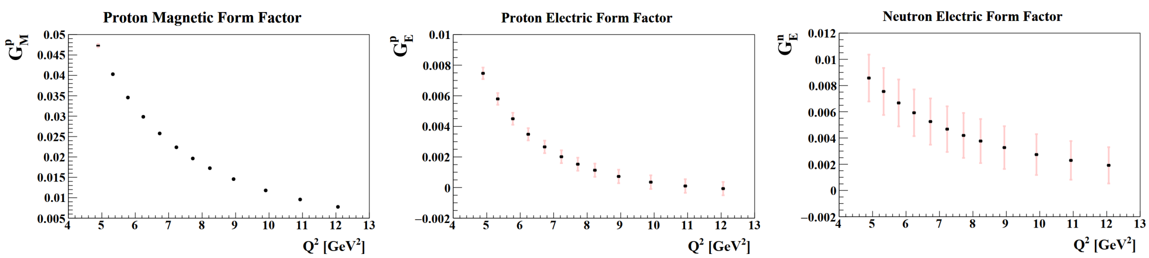

Figure 6.2: Arrington Parameterizations of G_M^p (left), G_E^p (middle) and G_E^n (right) that used for G_M^n calculation.

The results of G_M^n as a function of Q^2 for three different beam energies 10.2, 10.4 and 10.6 GeV are shown in Fig 6.3. The results show that all three data sets are consistent with each other.

The weighted average of G_M^n in each Q^2 bin is obtained by merging the results from these three different beam energies. The calculation of the weighted average involves minimizing the χ^2 value, following the formula [40]:

This reference is the CLAS6 PRL. Is that what you wanted?

$$\chi^2 = \sum_j \frac{(x_j - \bar{x})^2}{\sigma_j^2}, \tag{6.9}$$

where x_j represents the G_M^n value and σ_j is the statistical error associated with the j^{th} measurement contributing in that Q^2 bin (with j being an integer between 1 and

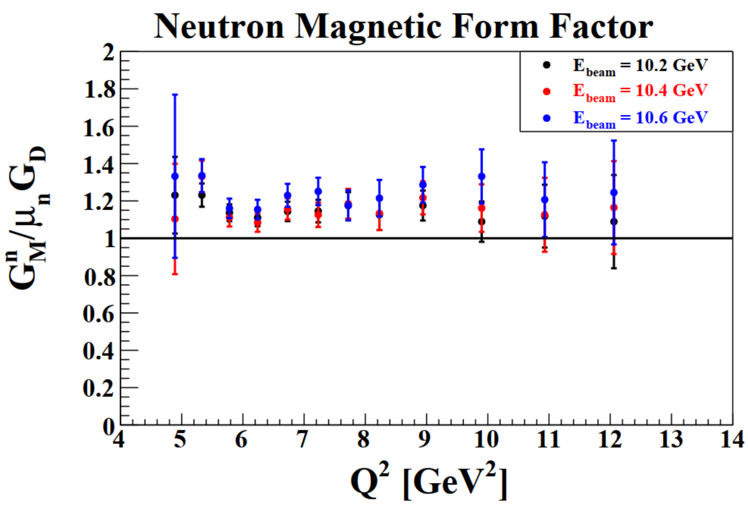

Figure 6.3: The G_M^n as a function of Q^2 for three different beam energy 10.2, 10.4 and 10.6 GeV. The black line showing $G_M^n = \mu_N G_D$.

3). By setting $\partial\chi^2/\partial\bar{x}$ to 0 in Eq. 6.9 and solving for $\bar{x}$, we find:

$$\bar{x} = \frac{\sum_j \frac{x_j}{\sigma_j^2}}{\sum_j \frac{1}{\sigma_j^2}}. \tag{6.10}$$

The statistical error for each point within the weighted average is determined using the following formula:

$$\begin{aligned} \sigma_{\bar{x}}^2 &= \sum_j \left(\frac{\partial\bar{x}}{\partial x_j}\right)^2 \sigma_j^2, \\ &= \frac{1}{\sum_j \frac{1}{\sigma_j^2}}. \end{aligned} \tag{6.11}$$

The result of the weighted average for G_M^n is shown in Fig 6.4. The G_M^n results of CLAS12 data show a flat behavior over the range of $Q^2 = 5 - 12$ GeV^2. The numerical values of the three individual measurements and the weighted average of G_M^n can be found in Appendix C.

as a function of Q2.

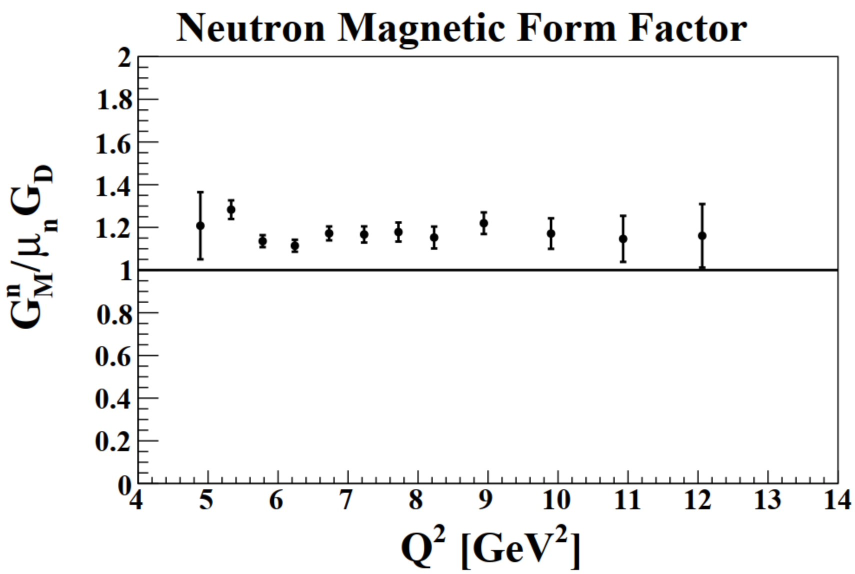

Figure 6.4: G_M^n weighted average as a function of Q^2 obtained by combining data from three different beam energy 10.2, 10.4 and 10.6 GeV. The black line showing $G_M^n = \mu_N G_D$.

6.2 Systematic Uncertainties

need a 'the'

There are multiple sources of systematic uncertainties that can affect the accuracy of G_M^n measurement. To determine the total systematic uncertainty, the following sources have been considered:

Need 'uncertainty' here and for each bullet.

- Systematic due to neutron detection efficiency (δ_{syst}^{NDE})
- Systematic due to electron identification cuts:
  - vertex cut ($\delta_{syst}^{v_z}$)
  - fiducial cut ($\delta_{syst}^{fiducial}$)
  - Sampling Fraction cut (δ_{syst}^{SF})
- Systematic due to quasi-elastic selection cuts:
  - $E_{\text{beam}}^{\text{angles}}$ cut (δ_{syst}^{beam}).
  - $\Delta\phi$ cut ($\delta_{syst}^{\Delta\phi}$)
  - θ_{pq} cut ($\delta_{syst}^{\theta_{pq}}$)
- Systematic due to radiative effects (δ_{syst}^{rad})

These uncertainties are determined by making small variations to a particular source while keeping others constant, and observing how the G_M^n results change. The formula used to calculate the systematic uncertainty associated with the variation in the i^{th} source is given by:

$$\delta^i_{syst} = \frac{|G_M^n - G_M^{n\ alt}|}{G_M^n} \times 100 \tag{6.12}$$

where G_M^n represents the reference measurement and $G_M^{n\ alt}$ corresponds to the measurement with an alternate cut.

Uncertainty

6.2.1 Systematic due to Neutron Detection Efficiency

The neutron detection efficiency (NDE) was calculated using two different functions, Gaussian and Crystal Ball functions, as described in Section 3.8. The difference between the results obtained by these two functions is less than 3% as shown in Fig 6.5.

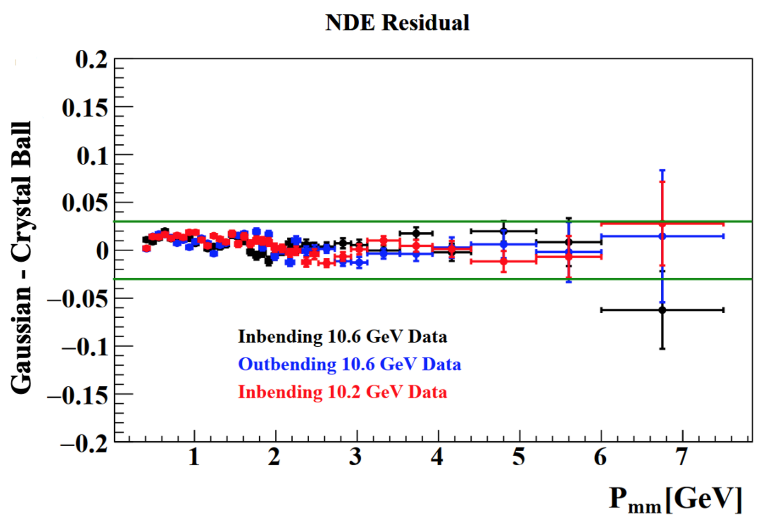

Figure 6.5: The difference of the neutron detection efficiency between the Gaussian and the Crystal Ball function, binned in missing momentum of neutron for inbending and outbending 10.6 GeV and inbending 10.2 GeV datasets.

.

The uncertainty associated with the NDE is determined by recalculating the G_M^n using the Gaussian parametrization listed in Table 3.7. The result of the G_M^n using both the Gaussian and Crystal Ball parametrizations is shown in the left panel of Fig 6.6. The systematic uncertainty is shown in the right panel of Fig. 6.6, which is determined by using Eq. 6.12 .

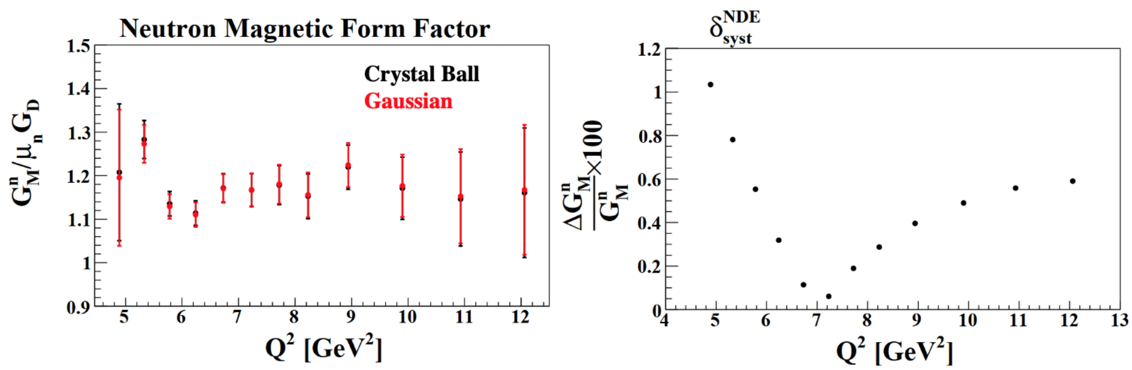

Figure 6.6: Left: Comparison of G_M^n measurements with Crystal Ball (black) and Gaussian (red) functions that applied during the NDE correction. Right: The estimated systematic uncertainty on G_M^n due to the parametrization of the Gaussian function.

Uncertainty

put this at the end of this section after you have shown it to be true,

6.2.2 Systematic due to Electron Identification Cuts

~~Since similar electron ID cuts were applied to both $D(e, e'p)$ and $D(e, e'n)$ channels, the systematic effect on the G_M^n due to electron identification is expected to be small.~~

Electron Vertex Cut: To assess the uncertainty associated with the electron vertex cut, we conducted an analysis without applying this particular cut. Figure 6.7 shows a comparison between G_M^n measurements with and without the electron vertex cut. The right panel of Fig. 6.7 shows the estimated systematic uncertainty due to the electron vertex cut.

Note the difference is zero for Q2 > 7.6 GeV2.

We set the systematic uncertainty at 0.04% or something like that.

Fiducial Cuts: Similarly, we disabled the PCAL and DC fiducial cuts during electron ID selection to investigate their impact. The comparison between G_M^n measurements with and without these fiducial cuts is shown in the left panel of Fig. 6.8. The right panel of the same figure shows the estimated systematic uncertainty due to the fiducial cuts.

We set the systematic uncertainty at 0.8% or something like that.

Sampling Fraction Cut: For the sampling fraction, we initially selected $\mu \pm 3.5\sigma$ from the fitted distribution versus momentum, as detailed in Section 3.4.5. We then modified this cut to $\mu \pm 3.0\sigma$ and recalculated G_M^n. Figure 6.9 shows a comparison of G_M^n results with the $\mu \pm 3.5\sigma$ and $\mu \pm 3.0\sigma$ cuts on the sampling fraction. The right panel of Fig. 6.9 shows the corresponding systematic uncertainty associated with the sampling fraction cut.

We set the systematic uncertainty at 0.4% or something like that.

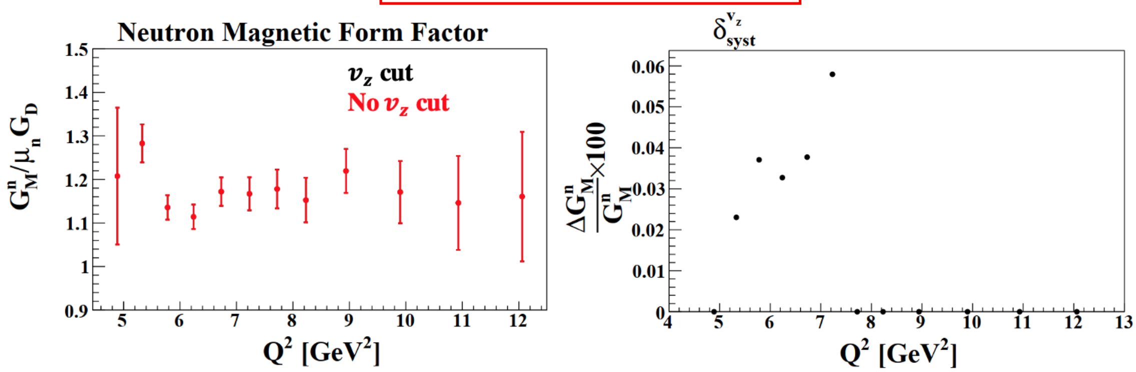

Figure 6.7: Left: Comparison of G_M^n measurements with (black) and without (red) electron vertex cut that applied during particle identification. Right: The estimated systematic uncertainty on G_M^n due to electron vertex cut.

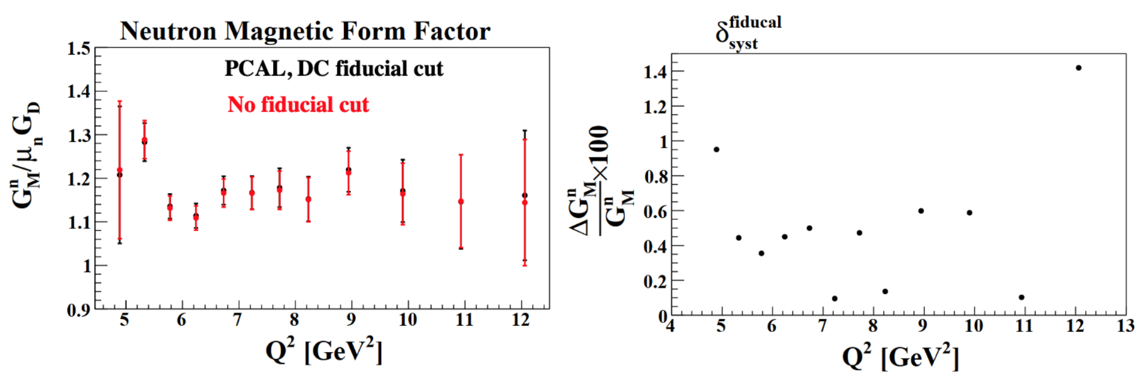

Figure 6.8: Left: Comparison of G_M^n measurements with (black) and without (red) fiducial cuts that applied during particle identification. Right: The estimated systematic uncertainty on G_M^n due to fiducial cuts.

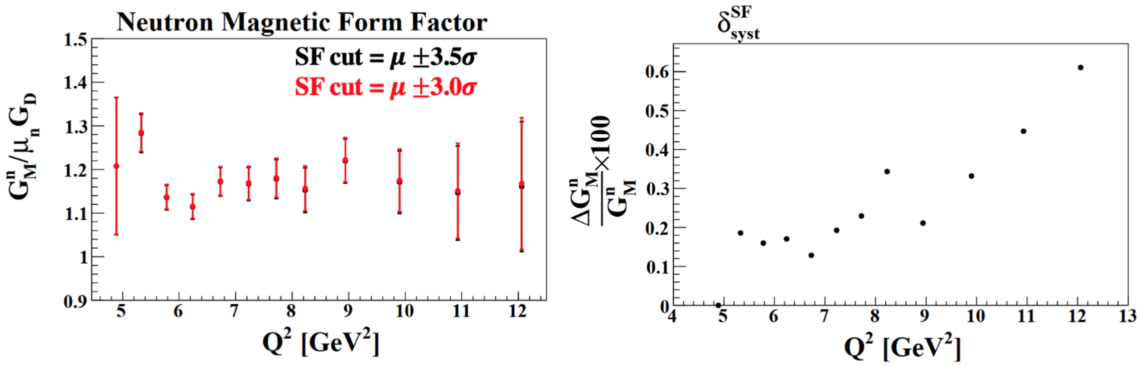

Figure 6.9: Left: Comparison of G_M^n measurements with different SF cut that applied during electron identification. Right: The estimated systematic uncertainty on G_M^n due to SF cut.

Uncertainty due to Quasi-elastic

Why? Again this sounds like a conclusion to put at the end.

6.2.3 Systematic ~~due to Qusi-elastic~~ Selection Cuts

The major source of systematic uncertainties in the G_M^n analysis is expected to be the quasi-elastic selection procedure.

We may want to discuss how this choice was made. e.g. avoids regions where background becomes significant.

Incident Electron Beam Energy Cut: In the quasi-elastic event selection, we applied a $\mu{\pm}1.0\sigma$ cut on the incident electron beam energy $E_{\text{beam}}^{\text{angles}}$, as described in Section 4.3. To assess the systematic uncertainty, we altered this cut to $\mu{\pm}1.25\sigma$ and recalculated G_M^n. The comparison between G_M^n measurements with the $\mu{\pm}1.0\sigma$ and $\mu{\pm}1.25\sigma$ cuts on $E_{\text{beam}}^{\text{angles}}$ is shown in the left panel of Fig. 6.10. The right panel of the

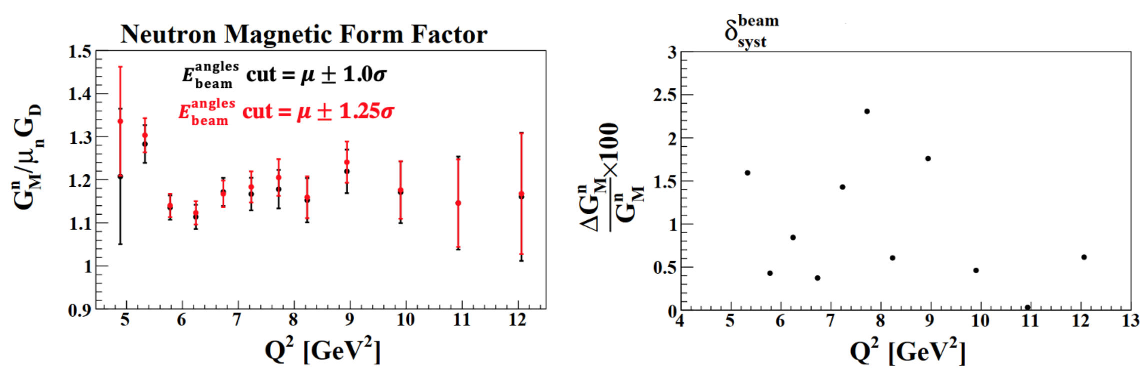

Figure 6.10: Left: Comparison of G_M^n measurements with different $E_{\text{beam}}^{\text{angles}}$ cut that applied during quasi-elastic events selection. Right: The estimated systematic uncertainty on G_M^n due to $E_{\text{beam}}^{\text{angles}}$ cut.

same figure shows the estimated systematic uncertainty due to the incident electron beam energy $E_{\mathrm{beam}}^{\mathrm{angles}}$.

We set the systematic uncertainty at 2.2% or the average of the rhs of fig 6.10 or something like that.

$\Delta\phi$ **Cuts:** Another crucial cut for quasi-elastic event selection was a $\mu\pm1.0\sigma$ cut on the $\Delta\phi$ distribution. We modified this cut to $\mu\pm1.25\sigma$ and recalculated G_M^n. The comparison between G_M^n measurements with the $\mu\pm1.0\sigma$ and $\mu\pm1.25\sigma$ cuts on $\Delta\phi$ is depicted in the left panel of Fig. 6.11. The right panel of the same figure shows the estimated systematic uncertainty due to the $\Delta\phi$ cuts.

We set the systematic uncertainty at 2.2% or the average of the rhs of fig 6.11 or something like that.

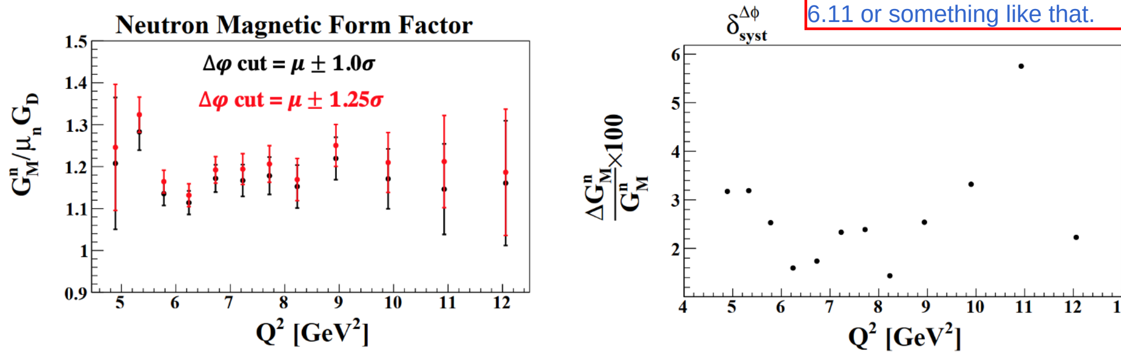

Figure 6.11: Left: Comparison of G_M^n measurements with different $\Delta\phi$ cut that applied during quasi-elastic events selection. Right: The estimated systematic uncertainty on G_M^n due to $\Delta\phi$ cut.

θ_{pq} **Cuts:** The final cut used for quasielastic event selection was the θ_{pq} cut. We considered θ_{pq} cuts that are 10% larger and 10% smaller than the cut we initially used, as shown by the black curves in Fig. 6.12. These variations in the θ_{pq} cut are used to understand how different θ_{pq} cut values affect the G_M^n measurements. The comparison between G_M^n measurements with the the original θ_{pq} cut and the 10% larger and smaller than the original cut are shown in the left panel of Fig. 6.13 and Fig. 6.14, respectively. The right panel of the same figures show the estimated systematic uncertainty due to the variations in the θ_{pq} cut.

We set the systematic uncertainty at 2% or the average of the rhs of figs 6.13 and 6.14 or something like that.

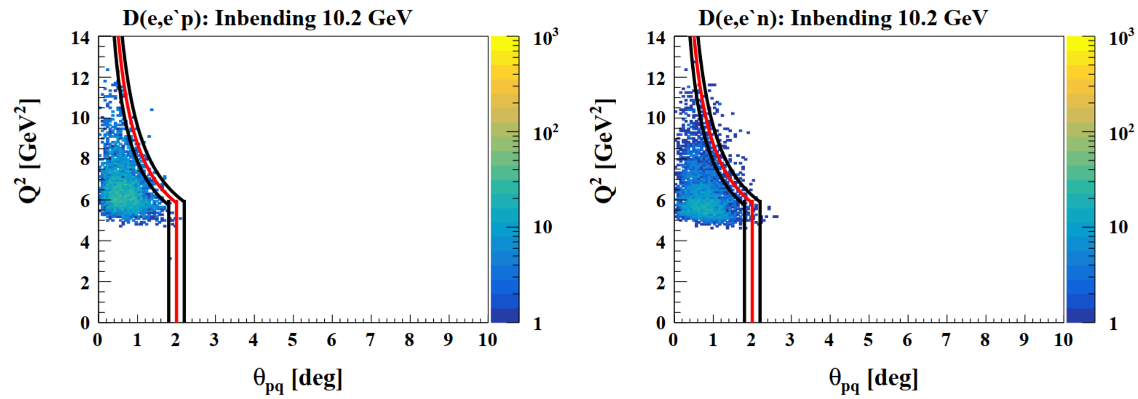

Figure 6.12: The Q^2 as a function of θ_{pq} distribution for $D(e, e'p)$ (left) and $D(e, e'n)$ (right) for 10.2 GeV dataset. The red curve represents the initial θ_{pq} cut applied to select quasi-elastic events. The black curves represent θ_{pq} cuts that are 10% larger and smaller than the original cut.

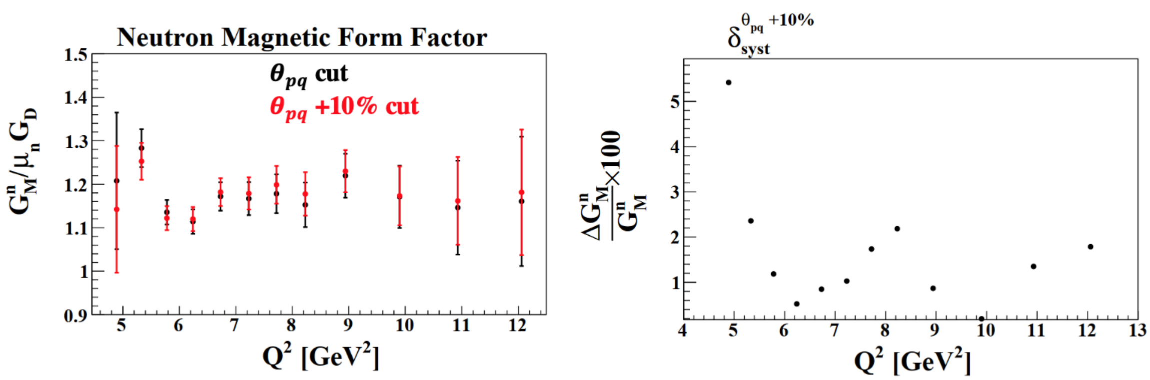

Figure 6.13: Left: Comparison of G_M^n measurements with different θ_{pq} cut that applied during quasi-elastic events selection. Right: The estimated systematic uncertainty on G_M^n due to a 10% larger than the original θ_{pq} cut.

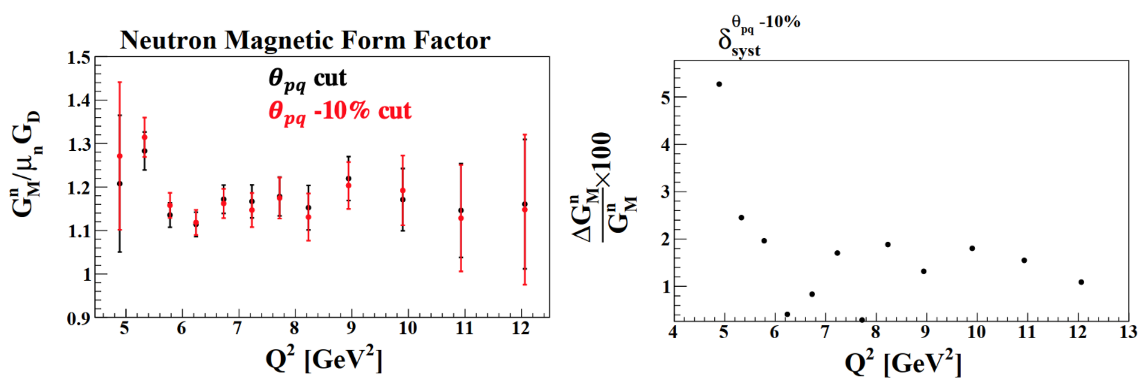

Figure 6.14: Left: Comparison of G_M^n measurements with different θ_{pq} cut that applied during quasi-elastic events selection. Right: The estimated systematic uncertainty on G_M^n due to a 10% smaller than the original θ_{pq} cut.

6.2.4 Systematic due to Radiative Effects

As mentioned in section 5.5, the systematic uncertainty associated with the radiative correction is determined by considering the differences between the smallest and largest values of the ratio of radiative corrections at each Q^2 value (see Fig. 5.13). The G_M^n is calculated twice: once using the smallest value of the ratio of radiative corrections at each Q^2 value and then using the largest value of the ratio of radiative corrections at each Q^2 value. The comparison between the resulting G_M^n measurements, based on the smallest and largest values of the ratio of radiative corrections, is shown in the left panel of Fig. 6.15. The right panel of the same figure show the estimated systematic uncertainty due to the radiative correction.

We set the systematic uncertainty at 0.1% or the average of the rhs of figs 6.15 or something like that.

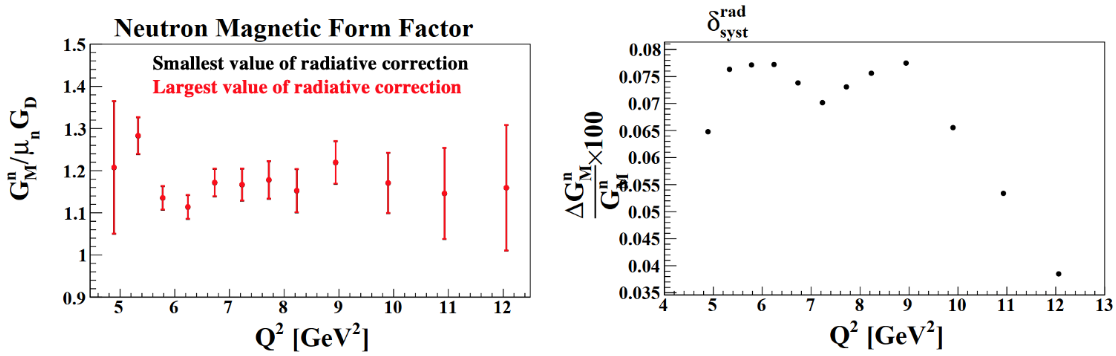

Figure 6.15: Left: Comparison of G_M^n measurements with smallest and largest value of the ratio of radiative corrections. Right: The estimated systematic uncertainty on G_M^n due to the radiative correction.

6.3 Total systematic uncertainty

The systematic uncertainty is computed individually for each Q^2 bin and for each source. Figure 6.16 provides an overview of how the different sources contribute to the systematic uncertainty across various Q^2 values. The figure shows that the uncertainty associated with $\Delta\phi$ (5.8%) is the dominant factor in most Q^2 bins. The other sources generally remain at or below a level of 1-2.5% over Q^2 values, except at the $Q^2 = 4.89$ GeV^2, where there is a noticeable increase in the systematic uncertainty. The other sources generally remain at or below a level of 1-2.5% over Q^2 values except at $Q^2 = 4.89$ GeV^2.

Good plot.

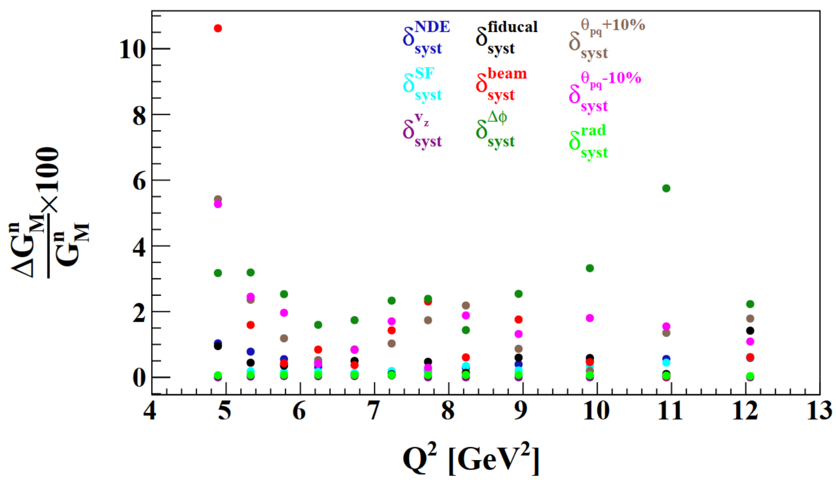

Figure 6.16: The estimated systematic uncertainty on G_M^n for the individual contributing sources as a function of Q^2 values.

The total systematic uncertainty δ^{total}_{syst} is determined by adding the individual contributions in quadrature:

$$\delta^{total}_{syst} = \sqrt{\sum_i {\delta^i_{syst}}^2}. \tag{6.13}$$

Figure 6.17 shows the total systematic uncertainty in the G_M^n measurement as a function of various Q^2 values. This figure shows that the total systematic uncertainty generally falls within the range of 2-6%. The calculated systematic uncertainties due to various sources at different Q^2 bins are listed in Table 6.1.

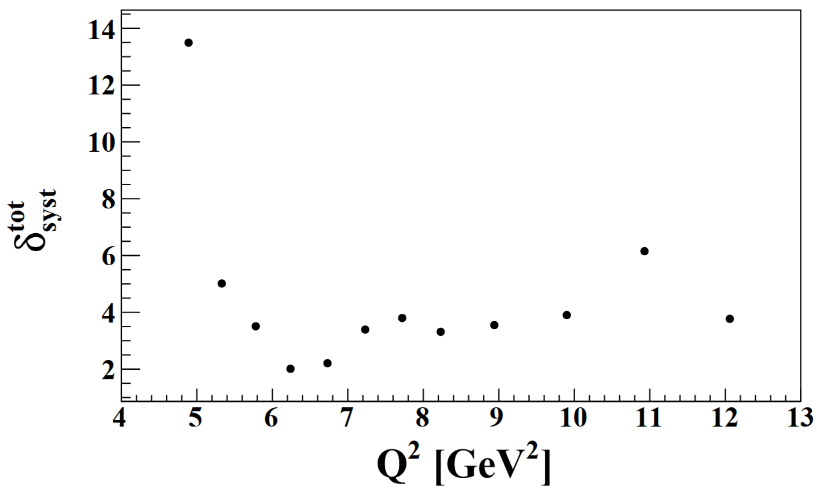

Figure 6.17: The total estimated systematic uncertainty on G_M^n in quadrature.

good table.

Q^2	δ_{syst}^{NDE}	$\delta_{syst}^{v_z}$	$\delta_{syst}^{fiducial}$	δ_{syst}^{SF}	δ_{syst}^{beam}	$\delta_{syst}^{\Delta\phi}$	$\delta_{syst}^{\theta_{pq}+10\%}$	$\delta_{syst}^{\theta_{pq}-10\%}$	δ_{syst}^{rad}	δ_{syst}^{total}
4.89	1.0343	0.0000	0.9506	0.0000	10.6224	3.1741	5.4195	5.2709	0.0648	13.4923
5.33	0.7810	0.0230	0.4439	0.1858	1.5937	3.1902	2.3604	2.4525	0.0763	5.0151
5.78	0.5531	0.0370	0.3548	0.1599	0.4289	2.5308	1.1866	1.9636	0.0771	3.5096
6.24	0.3189	0.0327	0.4498	0.1706	0.8438	1.5971	0.5233	0.4107	0.0772	2.0113
6.73	0.1140	0.0377	0.4995	0.1285	0.3735	1.7400	0.8492	0.8358	0.0738	2.2074
7.23	0.0608	0.0579	0.0954	0.1927	1.4293	2.3339	1.0289	1.7048	0.0702	3.393
7.72	0.1896	0.0000	0.4722	0.2295	2.3069	2.3887	1.7374	0.2905	0.0731	3.8010
8.23	0.2874	0.0000	0.1362	0.3435	0.6064	1.4379	2.1859	1.8841	0.0756	3.3148
8.94	0.3963	0.000	0.5983	0.2113	1.7592	2.5401	0.8679	1.3187	0.0775	3.5503
9.90	0.4900	0.000	0.5876	0.3320	0.4618	3.3214	0.1943	1.8031	0.0655	3.9030
10.93	0.5584	0.0000	0.1025	0.4469	0.0313	5.7523	1.3521	1.5500	0.0534	6.1519
12.06	0.5905	0.0000	1.4192	0.6105	0.6152	2.2289	1.7881	1.0901	0.0385	3.7699

Table 6.1: Systematic uncertainties due to various sources at different Q^2 bins.

CHAPTER 7

Conclusions and Outlook

Bibliography

[1] J. Manners. *Quantum physics: an introduction*, volume 7. CRC Press, 2000.

[2] F. Hanzel and AD. Martin. Quarks and Leptons: An Introductory Course in Modern Particle Phyics, 1984.

[3] S. J. Brodsky and G. R. Farrar. Scaling Laws at Large Transverse Momentum. *Physical Review Letters*, 31(18):1153, 1973.

[4] S. J. Brodsky and G. R. Farrar. Scaling Laws for Large-Momentum-Transfer Processes. *Physical Review D*, 11(5):1309, 1975.

[5] De Jager K. Arrington, J. and C.F. Perdrisat. Nucleon form factors – a jefferson lab perspective. *Journal of Physics: Conference Series*, 299:012002, may 2011.

[6] C.F. Perdrisat et al. Nucleon Electromagnetic Form Factors. *Progress in Particle and Nuclear Physics*, 59(2):694–764, 2007.

[7] G.D. Cates et al. Flavor Decomposition of the Elastic Nucleon Electromagnetic Form Factors. *Physical Review Letters*, 106(25):252003, 2011.

[8] Jefferson Lab. Experiment Proposal, 2007-2009. Available online at https://hallaweb.jlab.org/12GeV,https://www.jlab.org/exp_prog/generated/12GeV/apphallb.html,https://www.jlab.org/exp_prog/generated/12GeV/apphallc.html.

[9] M. E. Peskin and D. V. Schroeder. An Introduction to Quantum Field Theory Addison, 1995.

[10] F.J. Ernst et al. Electromagnetic Form Factors of the Nucleon. *Physical Review*, 119(3):1105, 1960.

[11] J. Binney and D. Skinner. *The physics of quantum mechanics*. Oxford University Press, 2013.

[12] B. Friedrich and H. Schmidt-Böcking. Otto Stern's Molecular Beam Method and Its Impact on Quantum Physics. In *Molecular Beams in Physics and Chemistry: From Otto Stern's Pioneering Exploits to Present-Day Feats*, pages 37–88. Springer International Publishing Cham, 2021.

[13] L. W. Alvarez and F. Bloch. A quantitative determination of the neutron moment in absolute nuclear magnetons. *Physical review*, 57(2):111, 1940.

[14] S. Galster et al. Elastic electron-deuteron scattering and the electric neutron form factor at four-momentum transfers 5 $\mathrm{fm}^{-2} < \mathrm{q}^2 < 14\ \mathrm{fm}^{-2}$. *Nuclear physics B*, 32(1):221–237, 1971.

[15] R.G. Sachs. High-Energy Behavior of Nucleon Electromagnetic Form Factors. *Physical Review*, 126(6):2256, 1962.

[16] F. Halzen and A. D. Martin. *Quark and Leptons: An Introductory Course in Modern Particle Physics*. John Wiley and Sons, 1984.

[17] J. J. Kelly. Nucleon Charge and Magnetization Densities From Sachs Form Factors. *Physical review C*, 66(6):065203, 2002.

[18] J. J. Kelly. Simple parametrization of nucleon form factors. *Physical Review C*, 70(6):068202, 2004.

[19] Gerald A Miller. Charge densities of the neutron and proton. *Physical review letters*, 99(11):112001, 2007.

[20] Michael Jeffery Musolf and T William Donnelly. The interpretation of parity-violating electron-scattering experiments. *Nuclear Physics A*, 546(3):509–587, 1992.

[21] Dmitry Borisyuk. Proton charge and magnetic rms radii from the elastic ep scattering data. *Nuclear Physics A*, 843(1-4):59–67, 2010.

[22] M Diehl, Th Feldmann, R Jakob, and P Kroll. Generalized parton distributions from nucleon form factor data. *The European Physical Journal C-Particles and Fields*, 39(1):1–39, 2005.

[23] H. Gao et al. Measurement of the neutron magnetic form factor from inclusive quasielastic scattering of polarized electrons from polarized ^{3}He. *Physical Review C*, 50(2):R546, 1994.

[24] B. Anderson et al. Extraction of the neutron magnetic form factor from quasielastic at Q^2= 0.1- 0.6 $(GeV/c)^2$. *Physical Review C*, 75(3):034003, 2007.

[25] W. Xu et al. Transverse $A_{T'}$ Asymmetry from the Quasielastic $A_{T'}$ Process and the Neutron Magnetic Form Factor. *Physical Review Letters*, 85(14):2900, 2000.

[26] W. Xu et al. Plane-wave impulse approximation extraction of the neutron magnetic form factor from quasielastic at Q^2= 0.3 to 0.6 $(GeV/c)^2$. *Physical Review C*, 67(1):012201, 2003.

[27] Richard F. Obrecht J. Electric Form Factor of the Neutron from Asymmetry Measurements. 2019.

[28] E.B. Hughes et al. Neutron form factors from inelastic electron-deuteron scattering. *Physical Review*, 139(2B):B458, 1965.

[29] S. Rock et al. Measurement of Elastic Electron-Neutron Cross Sections up to Q^2 = 10 $(GeV)^2$. *Physical Review Letters*, 49(16):1139, 1982.

[30] A.S. Esaulov et al. Measurement of the Neutron Magnetic Form Factor in the d(e, e')np Reaction for Momentum Transfers 0.48 <= Q^2 <= 0.83 GeV^2. *Yad. Fiz.;(USSR)*, 45(2), 1987.

[31] R.G. Arnold et al. Measurements of Transverse Quasielastic Electron Scattering From the Deuteron at High Momentum Transfers. *Physical Review Letters*, 61(7):806, 1988.

[32] A. Lung et al. Measurements of the electric and magnetic form factors of the neutron from Q^2= 1.75 to 4.00 $(GeV/c)^2$. *Physical Review Letters*, 70(6):718, 1993.

[33] P. Stein et al. Measurements of Neutron Form Factors. *Physical Review Letters*, 16(13):592, 1966.

[34] W. Bartel et al. Measurement of Proton and Neutron Electromagnetic Form Factors at Squared Four-Momentum Transfers up to 3 $(GeV/c)^2$. *Nuclear Physics B*, 58(2):429–475, 1973.

[35] P. Markowitz et al. Measurement of the Magnetic Form Factor of the Neutron. *Physical Review C*, 48(1):R5, 1993.

[36] K.M. Hanson, , et al. Large-angle quasielastic electron-deuteron scattering. *Physical Review D*, 8(3):753, 1973.

[37] H. Anklin et al. Precision Measurement of the Neutron Magnetic Form Factor. *Physics Letters B*, 336(3-4):313–318, 1994.

[38] E. E. W. Bruins et al. Measurement of the Neutron Magnetic Form Factor. *Physical review letters*, 75(1):21, 1995.

[39] G. Kubon et al. Precise Neutron Magnetic Form Factors. *Physics Letters B*, 524(1-2):26–32, 2002.

[40] J. Lachniet et al. Precise Measurement of the Neutron Magnetic Form Factor ${G_M}^n$ in the Few-GeV^2 Region. *Physical review letters*, 102(19):192001, 2009.

[41] Xilin Zhang, TJ Hobbs, and Gerald A Miller. Unified model of nucleon elastic form factors and implications for neutrino-oscillation experiments. *Physical Review D*, 102(7):074026, 2020.

[42] Lyubovitskij V.E. Gutsche, T. and I. Schmidt. Electromagnetic structure of nucleon and Roper in soft-wall AdS/QCD. *Physical Review D*, 97(5):054011, 2018.

[43] Ian C Cloët, Wolfgang Bentz, and Anthony W Thomas. Role of diquark correlations and the pion cloud in nucleon elastic form factors. *Physical Review C*, 90(4):045202, 2014.

[44] J.J. Sakurai. Vector-Meson Dominance and High-Energy Electron-Proton Inelastic Scattering. *Physical Review Letters*, 22(18):981, 1969.

[45] Jackson A.D. Iachello, F. and A. Lande. Semi-phenomenological fits to nucleon electromagnetic form factors. *Physics Letters B*, 43(3):191–196, 1973.

[46] M. Gari and W. Krümpelmann. Semiphenomenological Synthesis of Meson and Quark Dynamics and the EM Structure of the Nucleon. *Zeitschrift für Physik A Atoms and Nuclei*, 322(4):689–693, 1985.

[47] E. L. Lomon. Extended Gari-Krümpelmann Model Fits to Nucleon Electromagnetic Form Factors. *Physical Review C*, 64(3):035204, 2001.

[48] E. L. Lomon. Effect of Recent R_p and R_n Measurements on Extended Gari-Krümpelmann Model Fits to Nucleon Electromagnetic Form Factors. *Physical Review C*, 66(4):045501, 2002.

[49] E. L. Lomon. Effect of Revised R_n Measurements on Extended Gari-Krumpelmann Model Fits to Nucleon Electromagnetic Form Factors. *arXiv preprint nucl-th/0609020*, 2006.

[50] Richard Madey. E02-013 for gn e/gn m at q2 up to 3.4 (gev/c) 2.

[51] C. Crawford et al. Role of Mesons in the Electromagnetic Form Factors of the Nucleon. *Physical Review C*, 82(4):045211, 2010.

[52] G.A. Miller. Light front cloudy bag model: Nucleon electromagnetic form factors. *Physical Review C*, 66(3):032201, 2002.

[53] F. Gross, G. Ramalho and M.T. Pena. Pure S-wave covariant model for the nucleon. *Physical Review C*, 77(1):015202, 2008.

[54] E. Santopinto et al. High Q^2 behavior of the electromagnetic form factors in the relativistic hypercentral constituent quark model. *Physical Review C*, 82(6):065204, 2010.

[55] A. J. R. Puckett et al. Final analysis of proton form factor ratio data at $Q^2 =$ 4.0, 4.8, and 5.6 GeV^2. *Physical Review C*, 85(4):045203, 2012.

[56] F. Gross and P. Agbakpe. Shape of the nucleon. *Physical Review C*, 73(1):015203, 2006.

[57] M. De Sanctis, M. M et al. Electromagnetic form factors and the hypercentral constituent quark model. *Physical Review C*, 76(6):062201, 2007.

[58] Adnan Bashir, Lei Chang, Ian C Cloet, Bruno El-Bennich, Yu-Xin Liu, Craig D Roberts, and Peter C Tandy. Collective perspective on advances in dyson—schwinger equation qcd. *Communications in theoretical physics*, 58(1):79, 2012.

[59] IC Cloët, G Eichmann, B El-Bennich, T Klähn, and CD Roberts. Survey of nucleon electromagnetic form factors. *Few-Body Systems*, 46(1):1–36, 2009.

[60] X. Ji. Generalized parton distributions. *Annual Review of Nuclear and Particle Science*, 54(1):413–450, 2004.

[61] A.V. Belitsky and A.V. Radyushkin. Unraveling hadron structure with generalized parton distributions. *Physics reports*, 418(1-6):1–387, 2005.

[62] G. Ecker. Chiral Perturbation Theory. *Progress in Particle and Nuclear Physics*, 35:1–80, 1995.

[63] A. Faessler et al. Chiral Dynamics of Baryons in a Lorentz Covariant Quark Model. *Physical Review D*, 73(11):114021, 2006.

[64] S. J. Brodsky and G. F. de Téramond. AdS/CFT and light-front QCD. In *Search For The "Totally Unexpected" In The LHC Era*, pages 139–183. World Scientific, 2010.

[65] T. Gutsche et al. Nucleon structure including high Fock states in AdS/CFT. *Physical Review D*, 86(3):036007, 2012.

[66] Jefferson Lab. CEBAF at Jefferson Lab, 2022. Available online at https://www.jlab.org/brochures.

[67] N. Baltzell et al. The CLAS12 beamline and its performance. *Nuclear Instruments and Methods in Physics Research Section A: Accelerators, Spectrometers, Detectors and Associated Equipment*, 959:163421, 2020.

[68] V. D. Burkert et al. The clas12 spectrometer at jefferson laboratory. *Nuclear Instruments and Methods in Physics Research Section A: Accelerators, Spectrometers, Detectors and Associated Equipment*, 959:163419, 2020.

[69] M.A. Antonioli et al. The CLAS12 silicon vertex tracker. *Nuclear Instruments and Methods in Physics Research Section A: Accelerators, Spectrometers, Detectors and Associated Equipment*, 962:163701, 2020.

[70] D.S. Carman et al. The CLAS12 forward time-of-flight system. *Nuclear Instruments and Methods in Physics Research Section A: Accelerators, Spectrometers, Detectors and Associated Equipment*, 960:163629, 2020.

[71] P. Chatagnon et al. The CLAS12 central neutron detector. *Nuclear Instruments and Methods in Physics Research Section A: Accelerators, Spectrometers, Detectors and Associated Equipment*, 959:163441, 2020.

[72] R. Fair et al. The clas12 superconducting magnets. *Nuclear Instruments and Methods in Physics Research Section A: Accelerators, Spectrometers, Detectors and Associated Equipment*, 962:163578, 2020.

[73] A. Acker et al. The CLAS12 forward tagger. *Nuclear Instruments and Methods in Physics Research Section A: Accelerators, Spectrometers, Detectors and Associated Equipment*, 959:163475, 2020.

[74] M. D. Mestayer et al. The CLAS12 drift chamber system. *Nuclear Instruments and Methods in Physics Research Section A: Accelerators, Spectrometers, Detectors and Associated Equipment*, 959:163518, 2020.

[75] Y. G. Sharabian et al. The CLAS12 high threshold Cherenkov counter. *Nuclear Instruments and Methods in Physics Research Section A: Accelerators, Spectrometers, Detectors and Associated Equipment*, 968:163824, 2020.

[76] M. Ungaro et al. The CLAS12 low threshold Cherenkov detector. *Nuclear Instruments and Methods in Physics Research Section A: Accelerators, Spectrometers, Detectors and Associated Equipment*, 957:163420, 2020.

[77] M. Contalbrigo et al. The clas12 ring imaging cherenkov detector. *Nuclear Instruments and Methods in Physics Research Section A: Accelerators, Spectrometers, Detectors and Associated Equipment*, 964:163791, 2020.

[78] B. Raydo S. Boyarinov et al. The CLAS12 data acquisition system. *Nuclear Instruments and Methods in Physics Research Section A: Accelerators, Spectrometers, Detectors and Associated Equipment*, 966:163698, 2020.

[79] B. Raydo et al. The CLAS12 Trigger System. *Nuclear Instruments and Methods in Physics Research Section A: Accelerators, Spectrometers, Detectors and Associated Equipment*, 960:163529, 2020.

[80] V. Ziegler et al. The clas12 software framework and event reconstruction. *Nuclear Instruments and Methods in Physics Research Section A: Accelerators, Spectrometers, Detectors and Associated Equipment*, 959:163472, 2020.

[81] CLAS Collaboration at Jefferson Laboratory. CLAS12 RG-A - Analysis Note Overview and Procedures, 2020. https://clas12-docdb.jlab.org/DocDB/0009/000949/001/RGA_Analysis_Overview_and_Procedures-08172020.pdf.

[82] S. Das. A simple alternative to the Crystal Ball function. *arXiv preprint arXiv:1603.08591*, 2016.

[83] G. Ingelman, A. Edin, and J. Rathsman. Lepto 6.5—a monte carlo generator for deep inelastic lepton-nucleon scattering. *Computer Physics Communications*, 101(1-2):108–134, 1997.

[84] S. Stepanyan. Beam energy measurement with elastic scattering on CLAS, 2002. https://www.jlab.org/Hall-B/notes/clas_notes02/02-008.pdf.

[85] K. Alexei and S. Kuhn. Momentum Corrections for E6, 2003. https://www.jlab.org/Hall-B/notes/clas_notes03/03-005.pdf.

[86] GP Gilfoyle and O Alam. Queeg: A monte carlo event generator for quasielastic scattering on deuterium, 2014.

[87] V. Burkert A. Afanasev, I. Akushevich and K. Joo. QED radiative corrections in processes of exclusive pion electroproduction. *Physical Review D*, 66(7):074004, 2002.

[88] G. P. Gilfoyle and A. Afanasev. Radiative corrections for deuteron electro disintegration, 2005.

[89] S. Jeschonnek P. Ulmer Jr. Adam, F. Gross and J. W. Van Orden. Covariant description of inelastic electron-deuteron scattering: Predictions of the relativistic impulse approximation. *Physical Review C*, 66(4):044003, 2002.

[90] Zhihong Ye, John Arrington, Richard J Hill, and Gabriel Lee. Proton and neutron electromagnetic form factors and uncertainties. *Physics Letters B*, 777:8–15, 2018.

APPENDIX A

Fit Missing Mass Distribution using Gaussian Function

The following plots show the fitting of the expected and detected neutrons using Gaussian plus a 4th order Polynomial function. Also it shows the parameters of the fit as a function of P_{mm}.

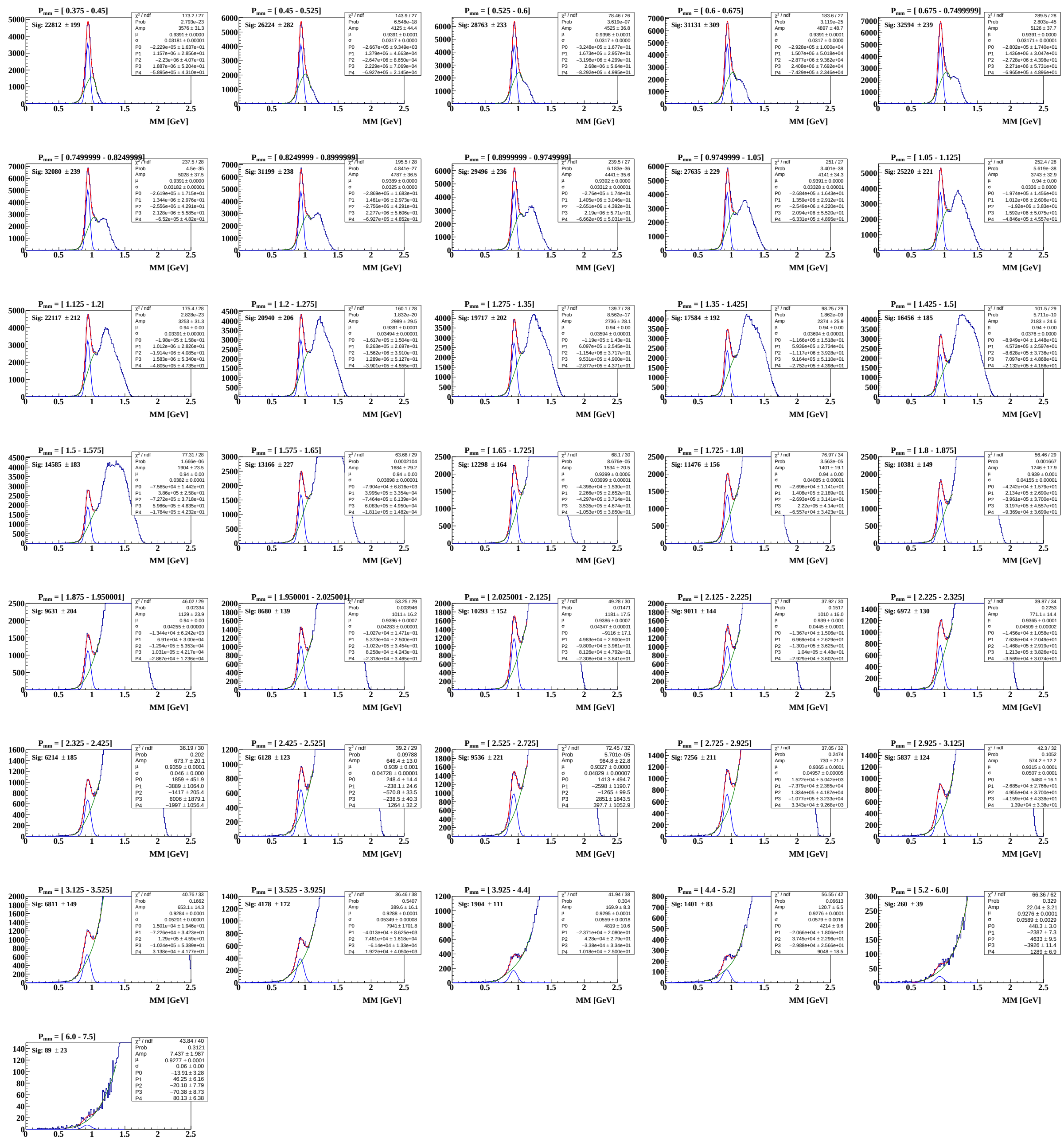

Figure A.1: The missing mass distribution of expected neutron $p(e, e'\pi^+)n$ for different P_{mm} bin. The distribution is fitted with a Gaussian plus polynomial background. The blue curve is the signal distribution after subtraction of the background distribution, the green is the background, and the red is the sum of the two. The fitting is shown for inbending 10.6 GeV dataset.

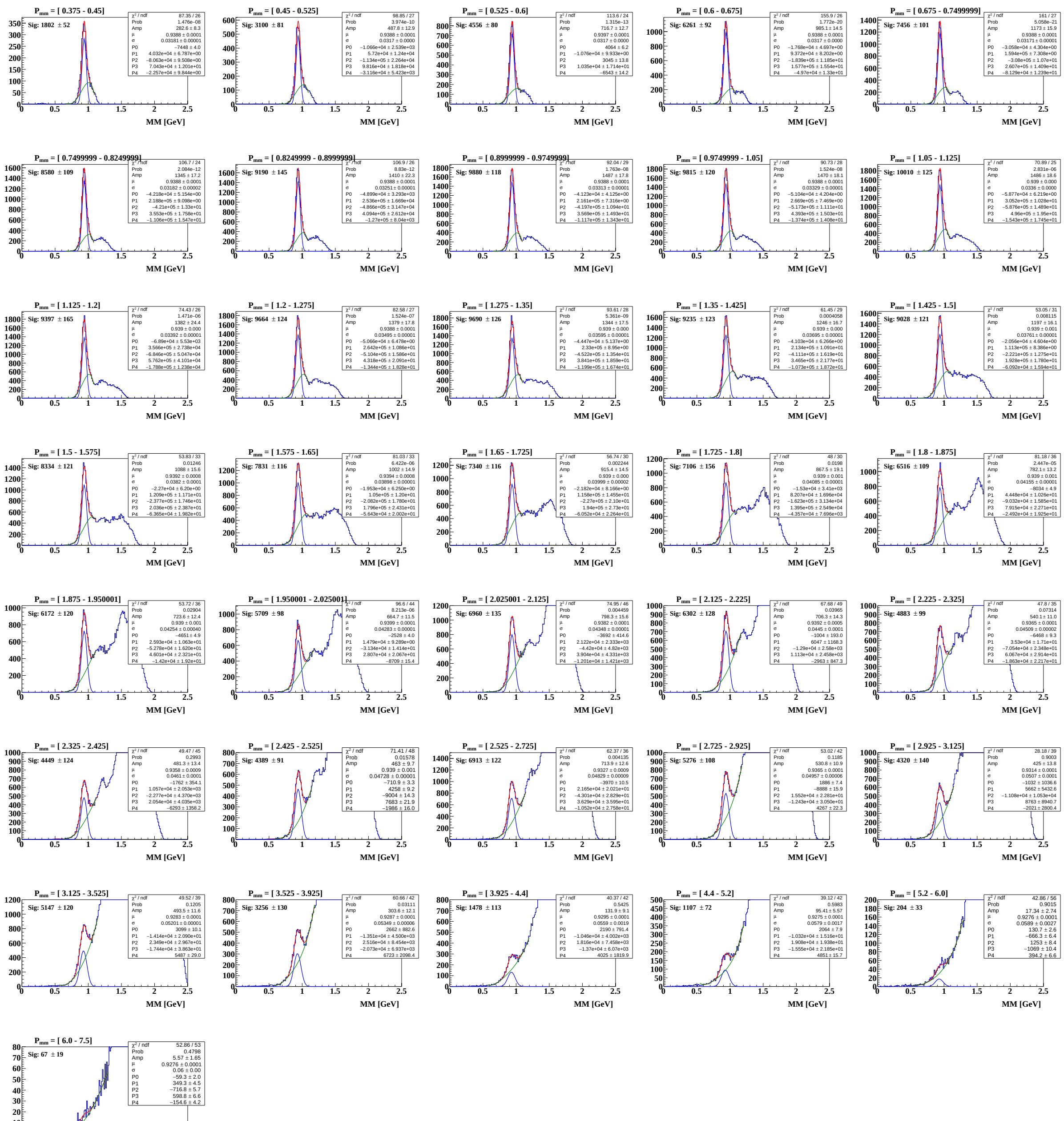

Figure A.2: The missing mass distribution of detected neutron $p(e, e'\pi^+n)$ for different P_{mm} bin. The distribution is fitted with a Gaussian plus polynomial background. The blue curve is the signal distribution after subtraction of the background distribution, the green is the background, and the red is the sum of the two. The fitting is shown for inbending 10.6 GeV dataset.

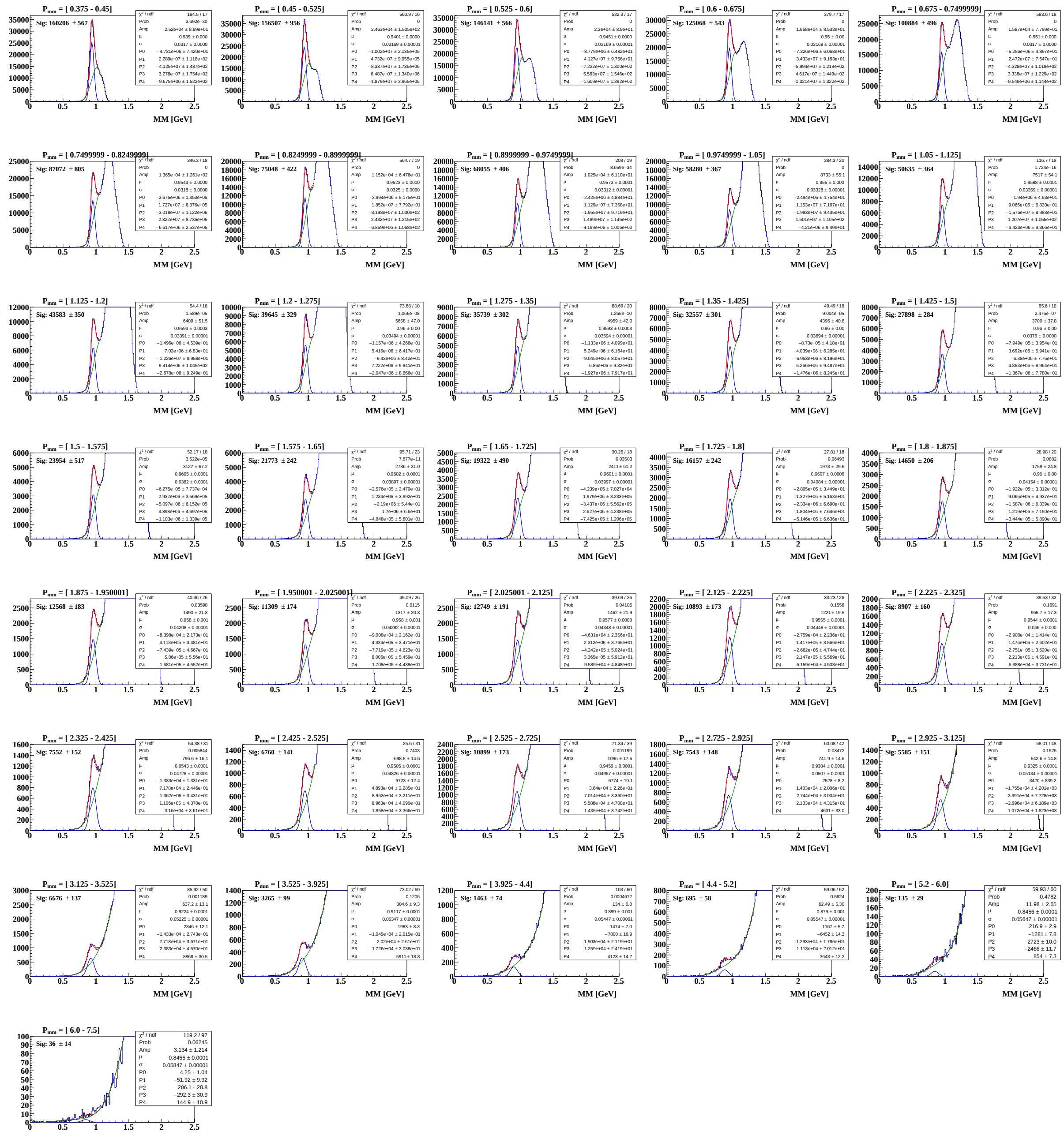

Figure A.3: Missing mass distribution of expected neutron $p(e, e'\pi^+)n$ for different P_{mm} bin. The distribution is fit with a gaussian + polynomial background. The blue curve is the signal distribution after subtraction of the background distribution, the green is the background, and the red is the sum of the two. The fitting is shown for outbending 10.6 GeV dataset.

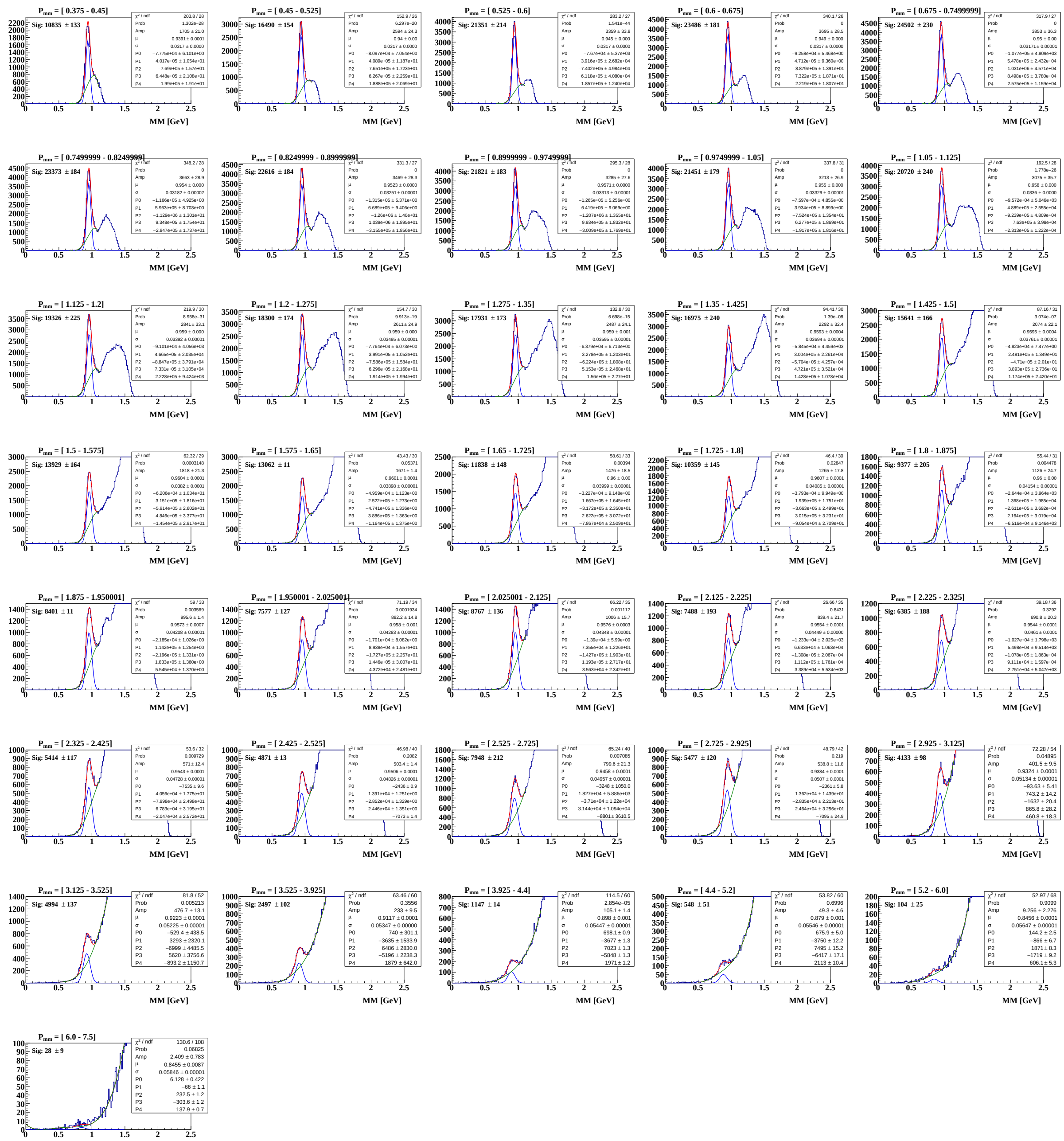

Figure A.4: Missing mass distribution of detected neutron $p(e, e'\pi^+ n)$ for different P_{mm} bin. The distribution is fit with a gaussian + polynomial background. The blue curve is the signal distribution after subtraction of the background distribution, the green is the background, and the red is the sum of the two. The fitting is shown for outbending 10.6 GeV dataset.

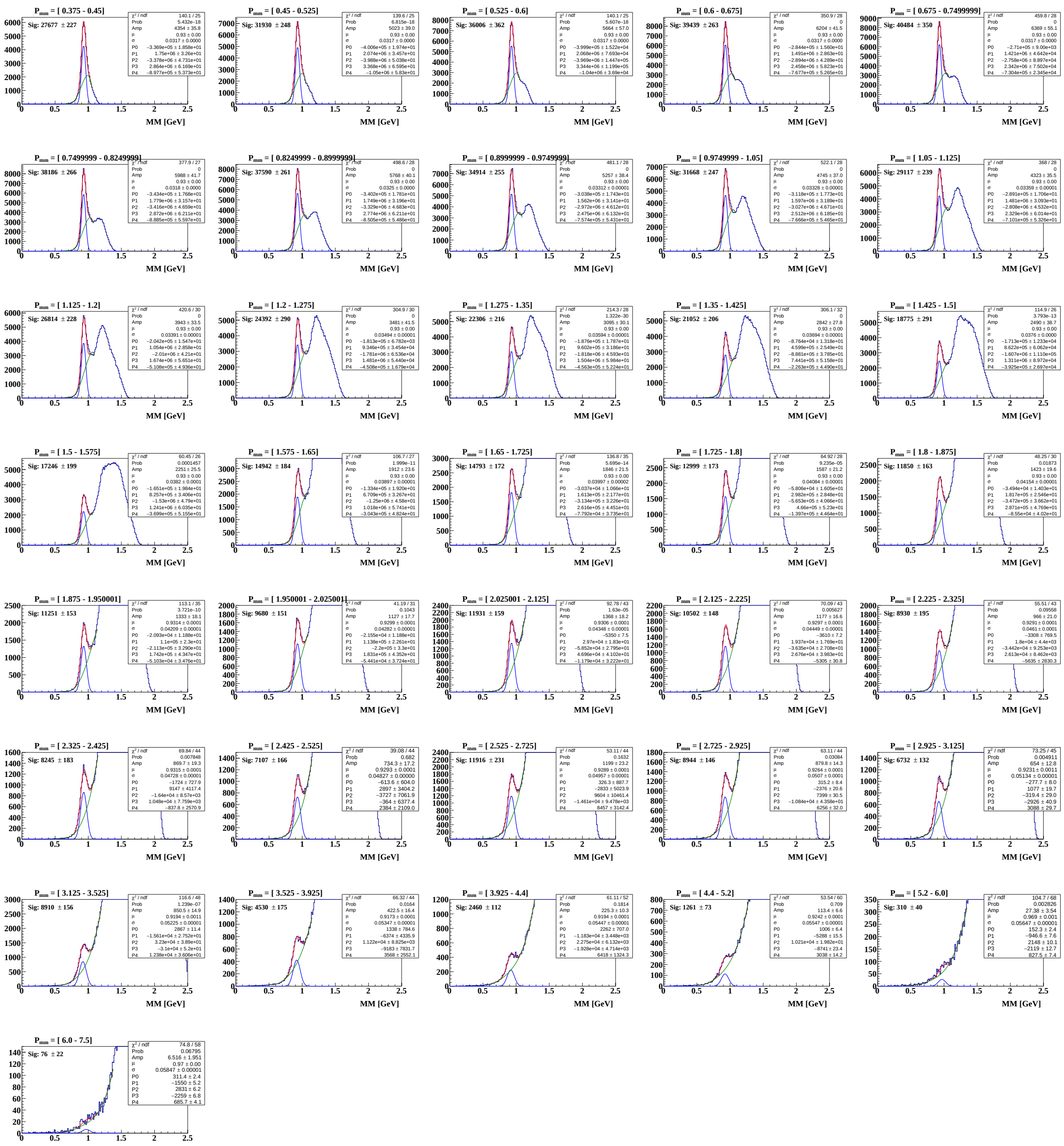

Figure A.5: Missing mass distribution of expected neutron $p(e, e'\pi^+ n)$ for different P_{mm} bin. The distribution is fit with a Gaussian + polynomial background. The blue curve is the signal distribution after subtraction of the background distribution, the green is the background, and the red is the sum of the two. The fitting is shown for inbending 10.2 GeV dataset.

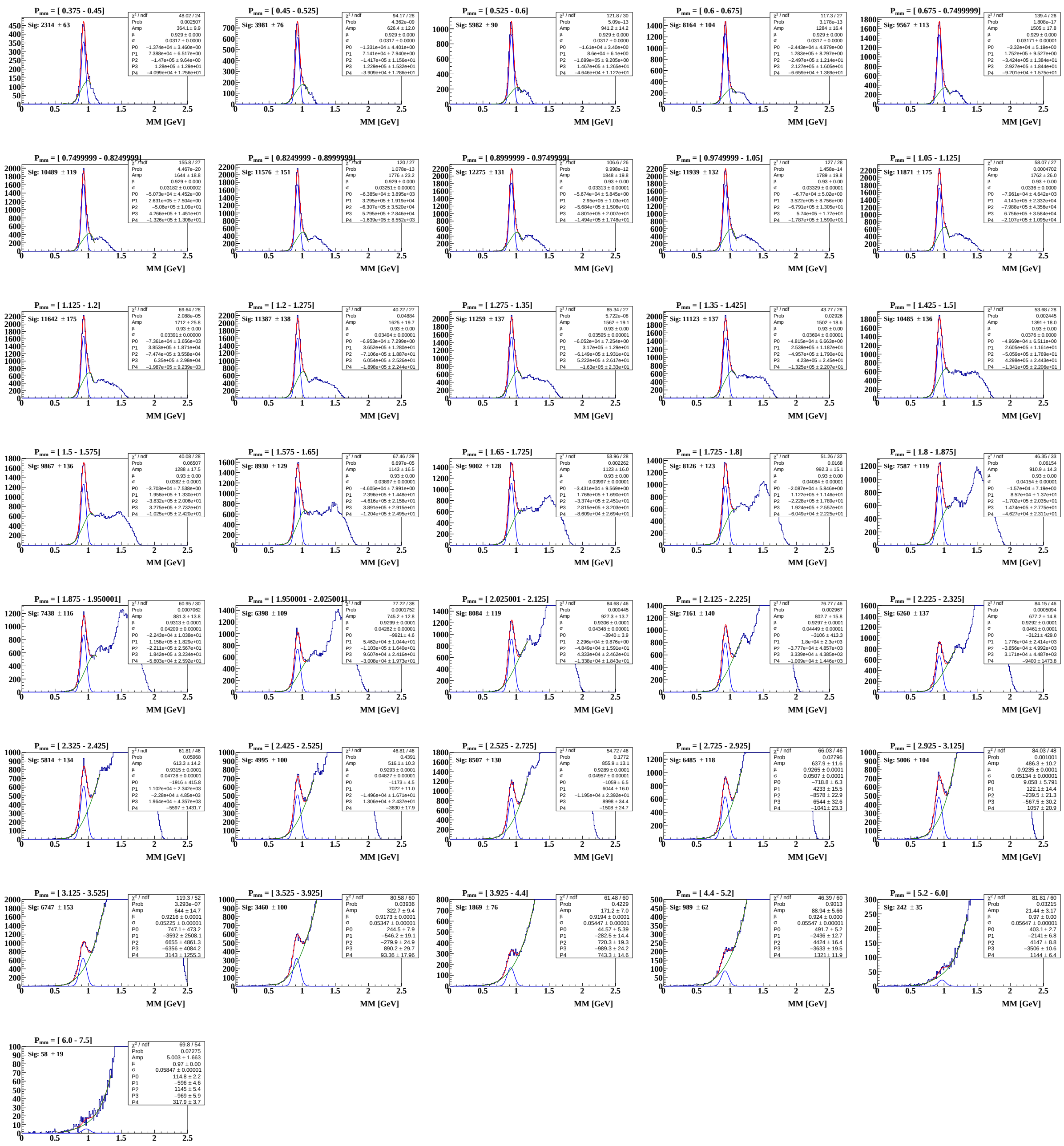

Figure A.6: Missing mass distribution of detected neutron $p(e, e'\pi^+n)$ for different P_{mm} bin. The distribution is fit with a Gaussian + polynomial background. The blue curve is the signal distribution after subtraction of the background distribution, the green is the background, and the red is the sum of the two. The fitting is shown for inbending 10.2 GeV dataset.

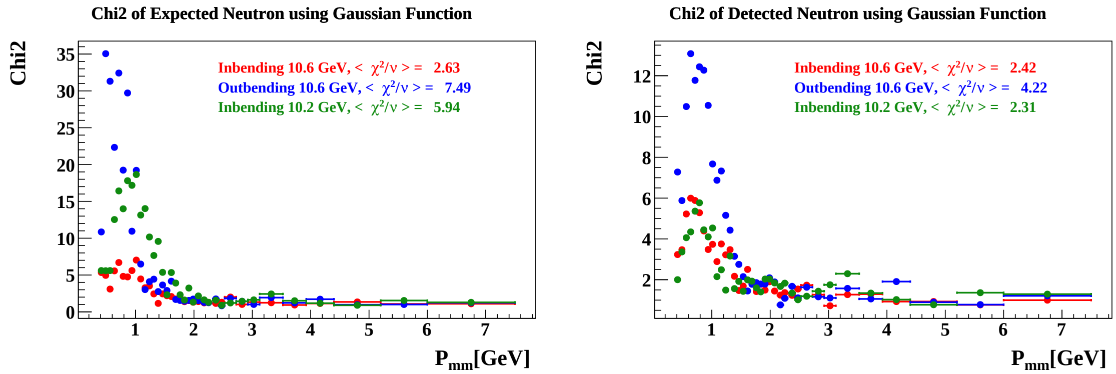

Figure A.7: The chi2 of the expected (left) and detected (right) neutron as a function of P_{mm} using Gaussian + polynomial background.

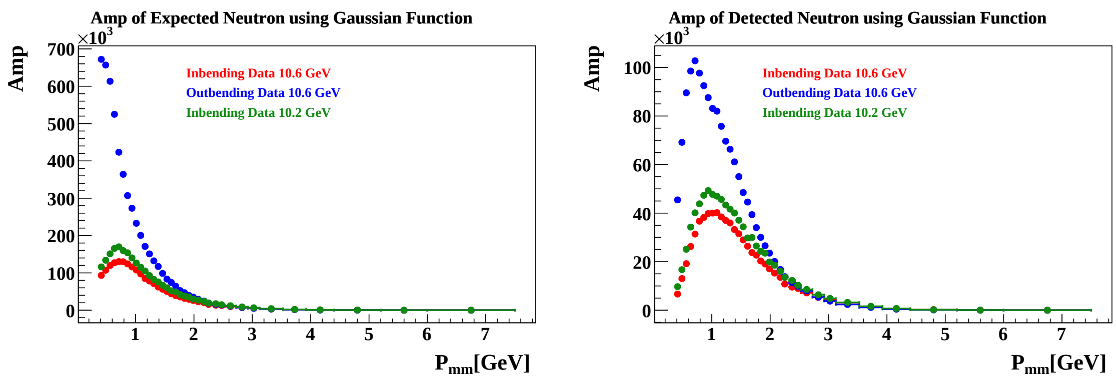

Figure A.8: The amplitude of the expected (left) and detected (right) neutron as a function of P_{mm} using Gaussian + polynomial background.

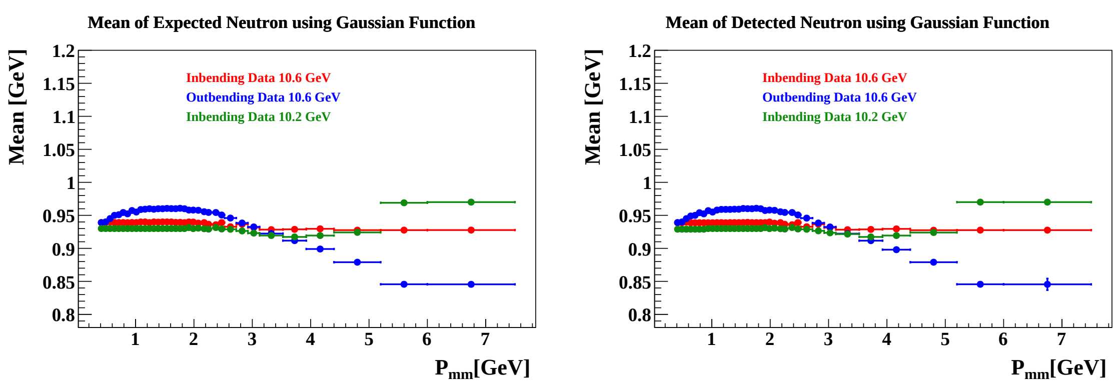

Figure A.9: The mean of the expected (left) and detected (right) neutron as a function of P_{mm} using Gaussian + polynomial background.

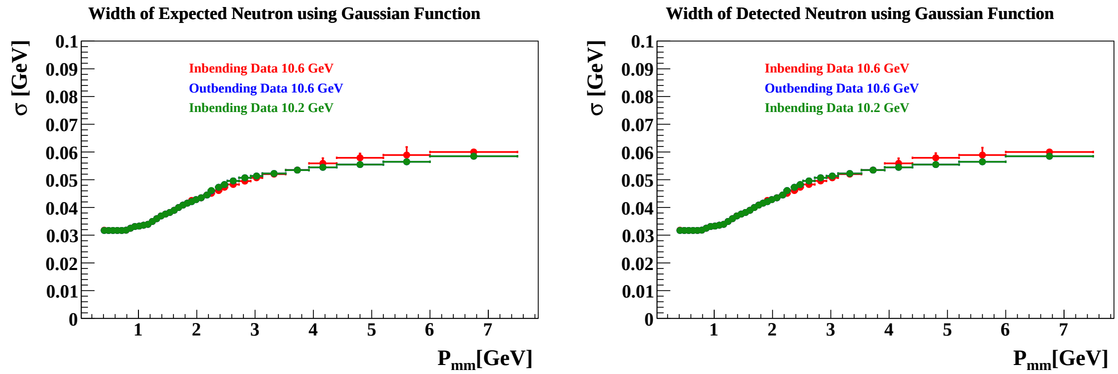

Figure A.10: The width of the expected (left) and detected (right) neutron as a function of P_{mm} using Gaussian + polynomial background.

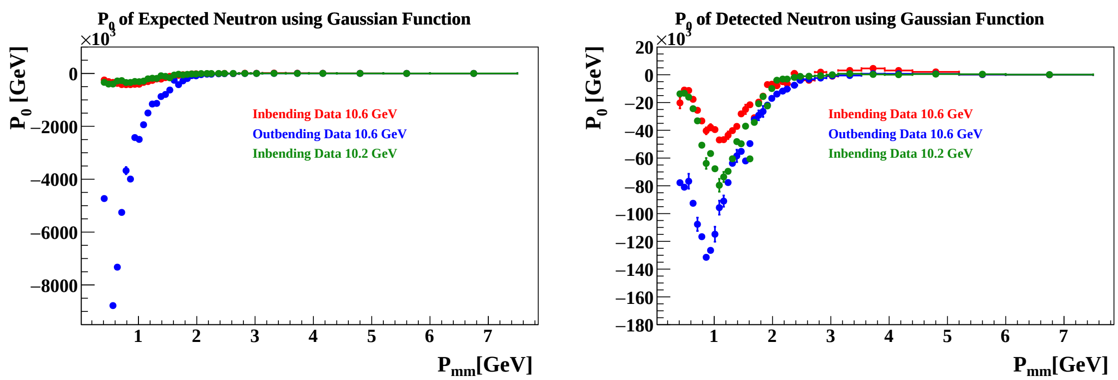

Figure A.11: The P_0 parameter of the expected (left) and detected (right) neutron as a function of P_{mm} using Gaussian + polynomial background.

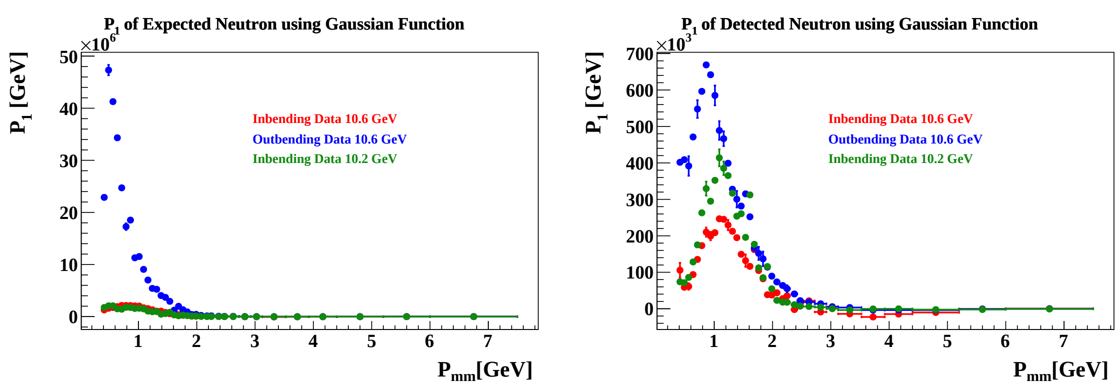

Figure A.12: The P_1 parameter of the expected (left) and detected (right) neutron as a function of P_{mm} using Gaussian + polynomial background.

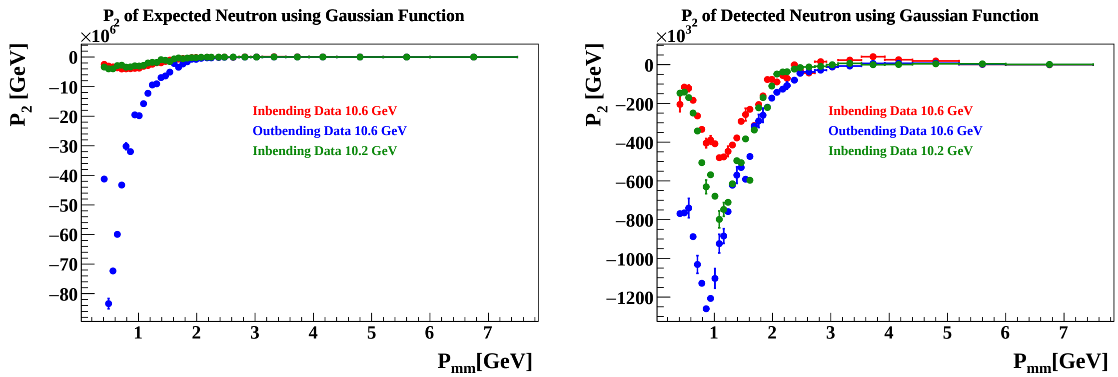

Figure A.13: The P_2 parameter of the expected (left) and detected (right) neutron as a function of P_{mm} using Gaussian + polynomial background.

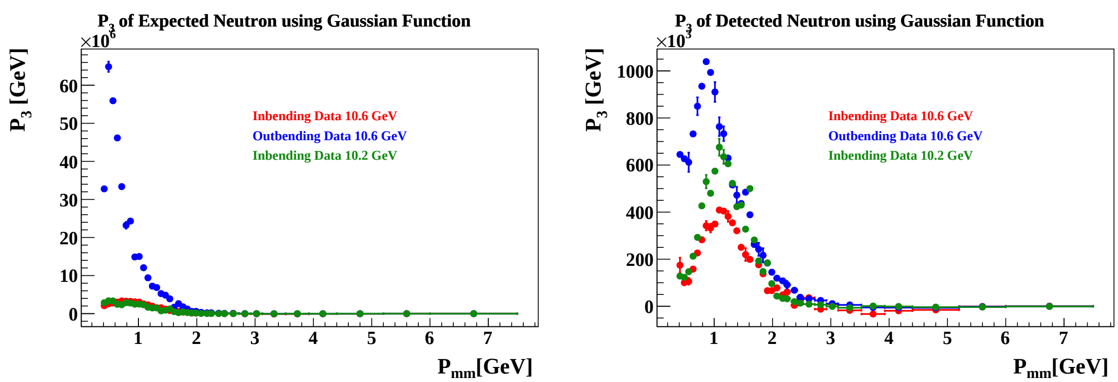

Figure A.14: The P_3 parameter of the expected (left) and detected (right) neutron as a function of P_{mm} using Gaussian + polynomial background.

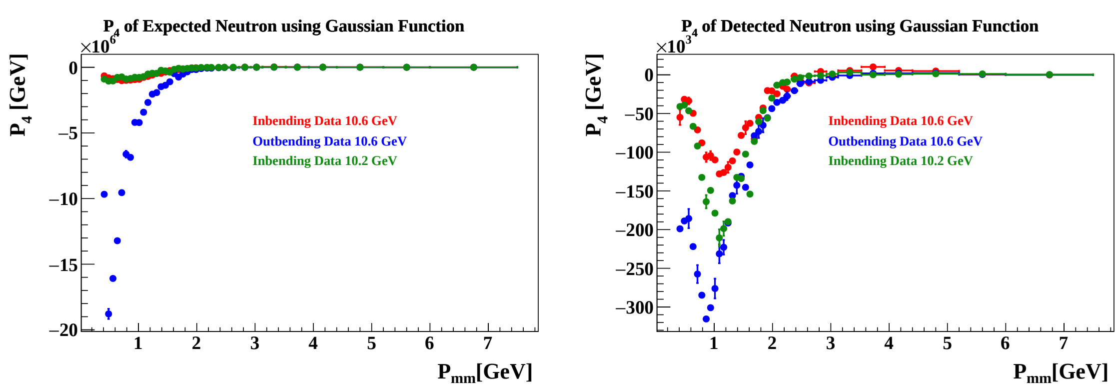

Figure A.15: The P_4 parameter of the expected (left) and detected (right) neutron as a function of P_{mm} using Gaussian + polynomial background.

APPENDIX B

Fit Missing Mass Distribution using Crystal Ball Function

The following plots show the fitting of the expected and detected neutrons using Crystal Ball plus a 4th order Polynomial function. Also it shows the parameters of the fit as a function of P_{mm}.

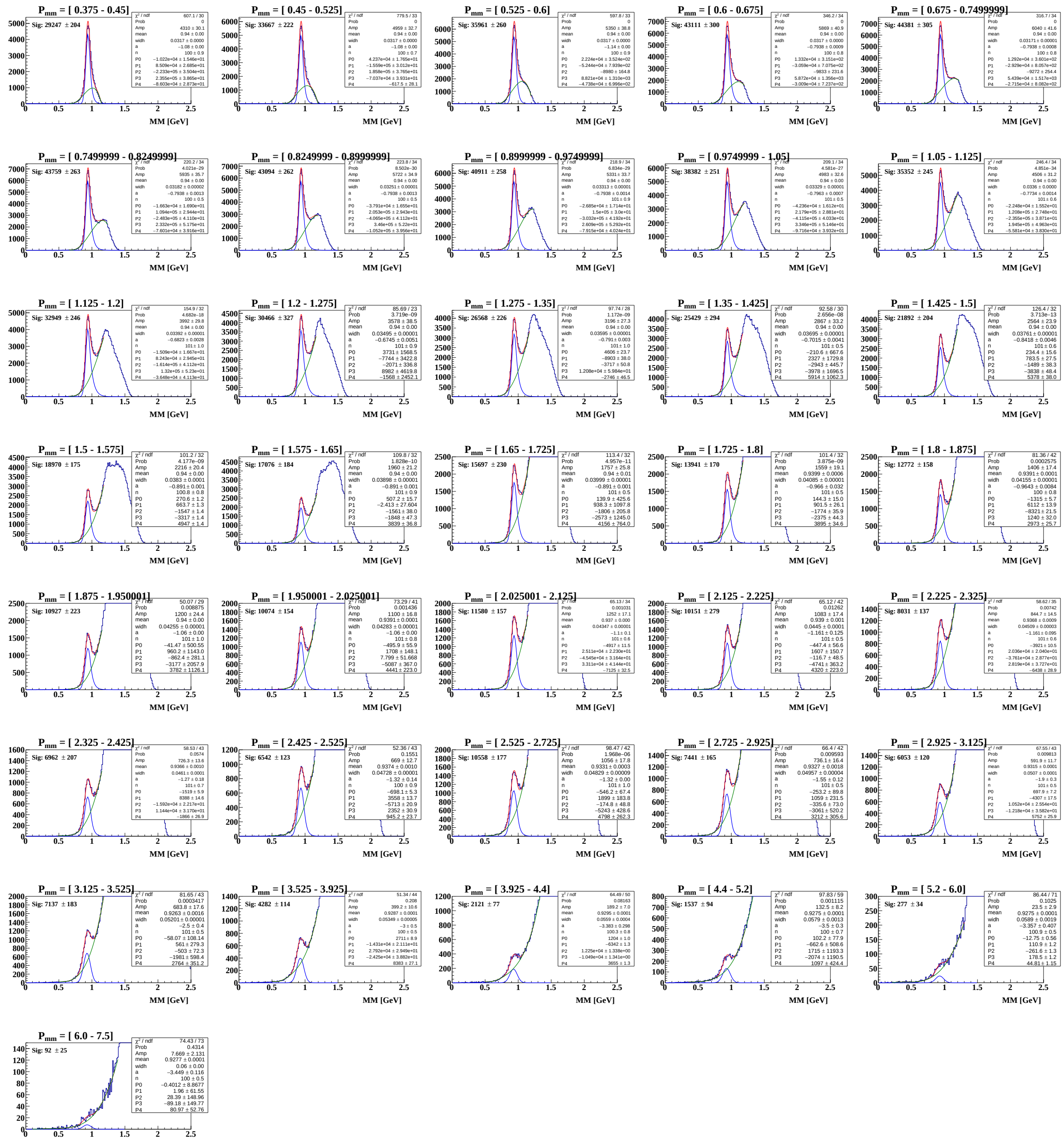

Figure B.1: The missing mass distribution of expected neutron $p(e, e'\pi^+)n$ for different P_{mm} bin. The distribution is fitted with a Crystal Ball + polynomial background. The blue curve is the signal distribution after subtraction of the background distribution, the green is the background, and the red is the sum of the two. The fitting is shown for inbending 10.6 GeV dataset.

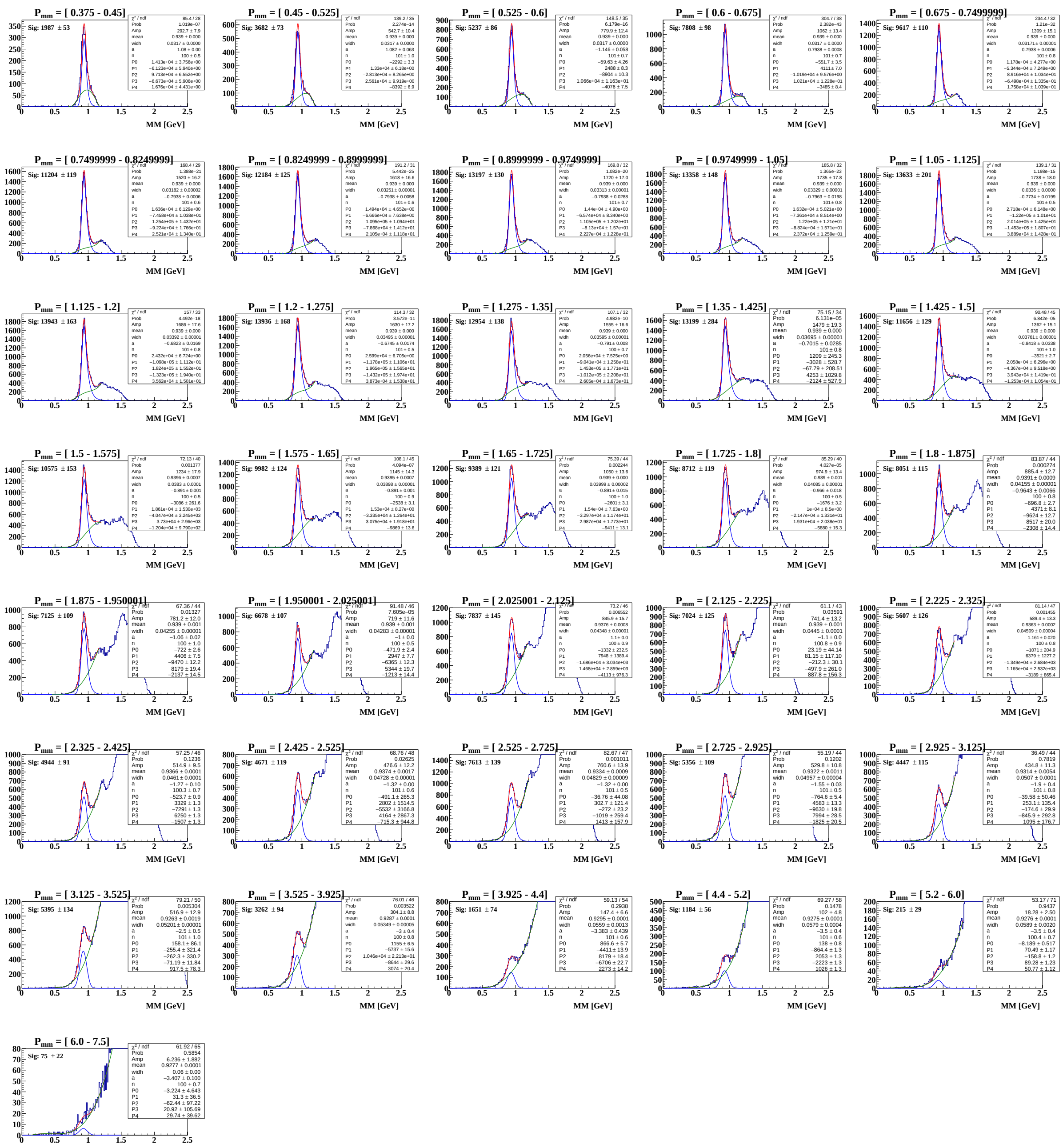

Figure B.2: The missing mass distribution of detected neutron $p(e, e'\pi^+n)$ for different P_{mm} bin. The distribution is fitted with a Crystal Ball + polynomial background. The blue curve is the signal distribution after subtraction of the background distribution, the green is the background, and the red is the sum of the two. The fitting is shown for inbending 10.6 GeV dataset.

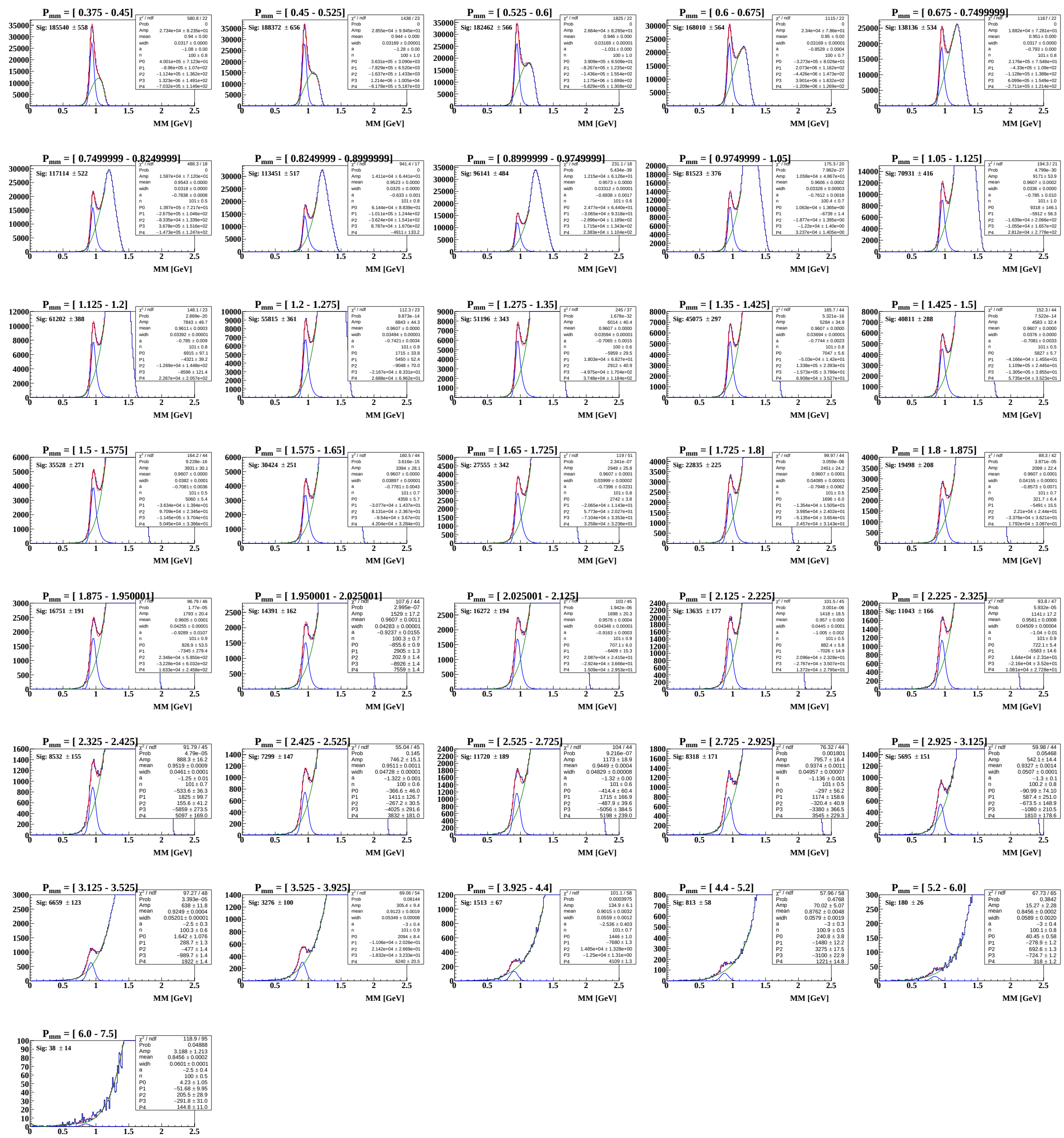

Figure B.3: Missing mass distribution of expected neutron $p(e, e'\pi^+)n$ for different P_{mm} bin. The distribution is fit with a Crystal ball + polynomial background. The blue curve is the signal distribution after subtraction of the background distribution, the green is the background, and the red is the sum of the two. The fitting is shown for outbending 10.6 GeV dataset.

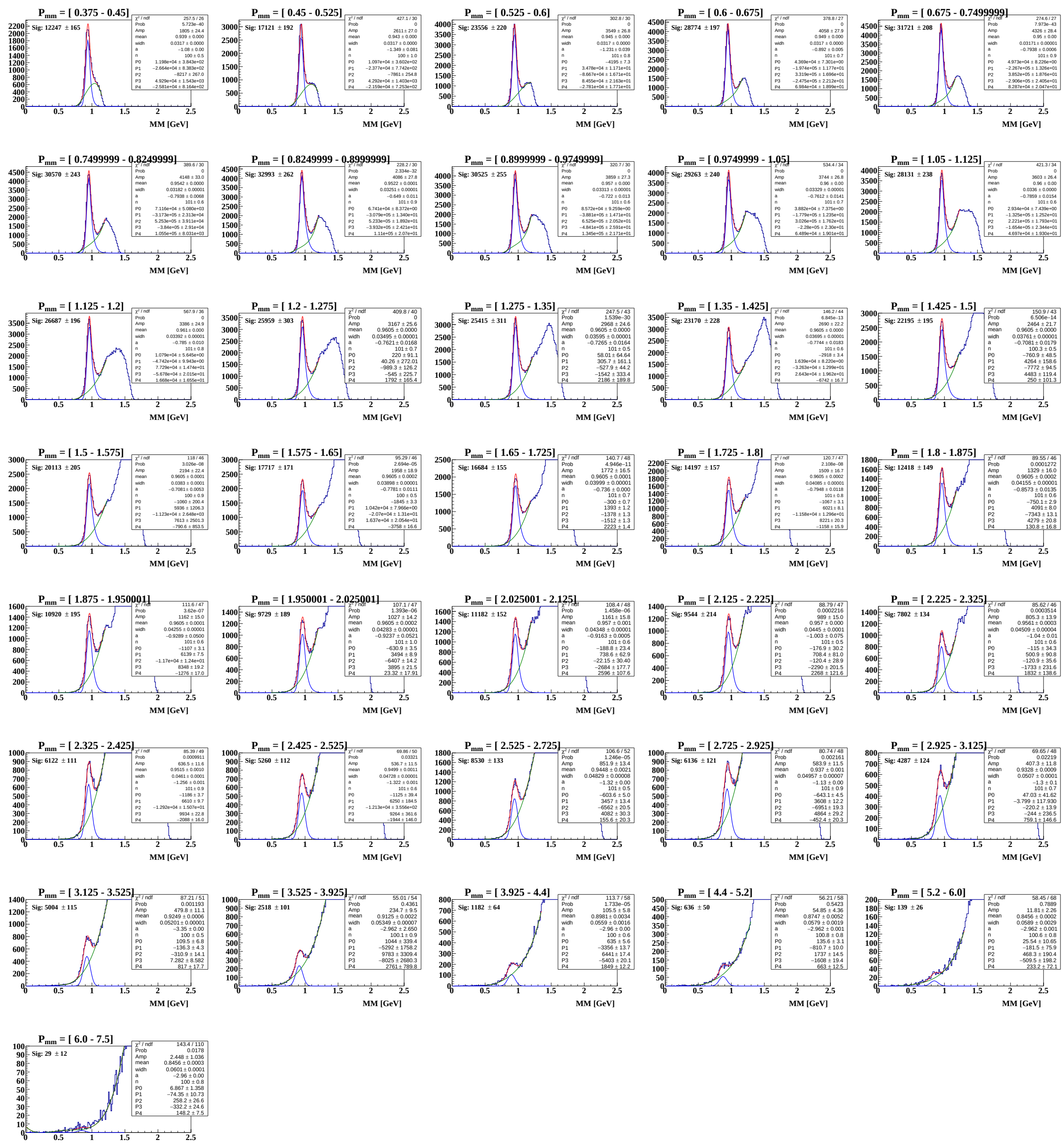

Figure B.4: Missing mass distribution of detected neutron $p(e, e'\pi^+)n$ for different P_{mm} bin. The distribution is fit with a Crystal ball + polynomial background. The blue curve is the signal distribution after subtraction of the background distribution, the green is the background, and the red is the sum of the two. The fitting is shown for outbending 10.6 GeV dataset.

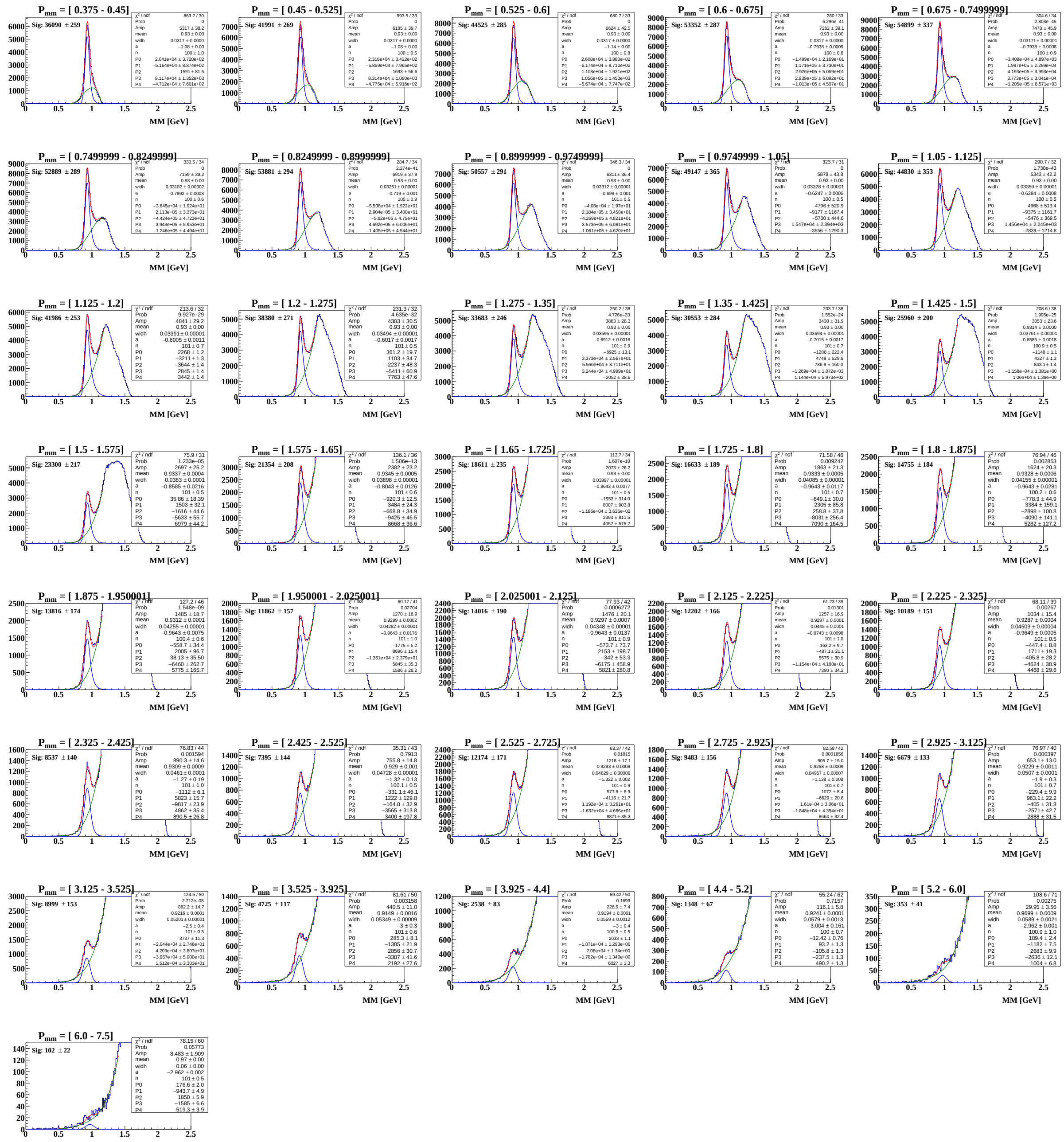

Figure B.5: Missing mass distribution of expected neutron $p(e, e'\pi^+)n$ for different P_{mm} bin. The distribution is fit with a Crystal ball + polynomial background. The blue curve is the signal distribution after subtraction of the background distribution, the green is the background, and the red is the sum of the two. The fitting is shown for inbending 10.2 GeV dataset.

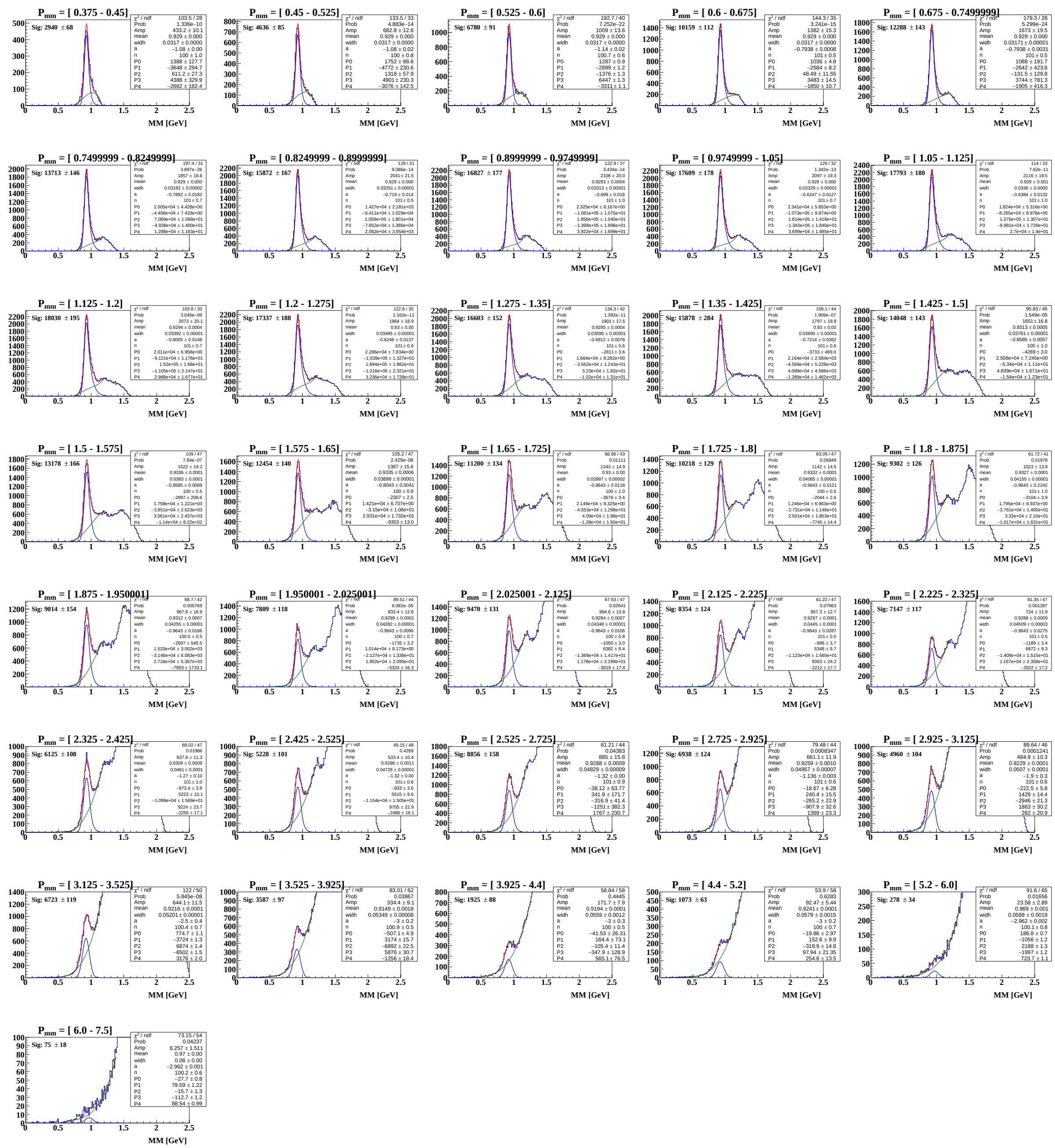

Figure B.6: Missing mass distribution of detected neutron $p(e, e'\pi^+)n$ for different P_{mm} bin. The distribution is fit with a Crystal ball + polynomial background. The blue curve is the signal distribution after subtraction of the background distribution, the green is the background, and the red is the sum of the two. The fitting is shown for inbending 10.2 GeV dataset.

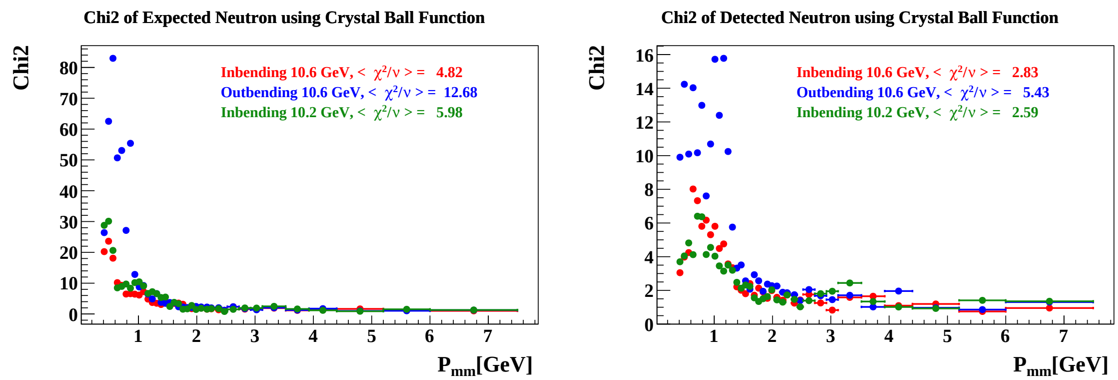

Figure B.7: The chi2 of the expected (left) and detected (right) neutron as a function of P_{mm} using Crystal ball + polynomial background.

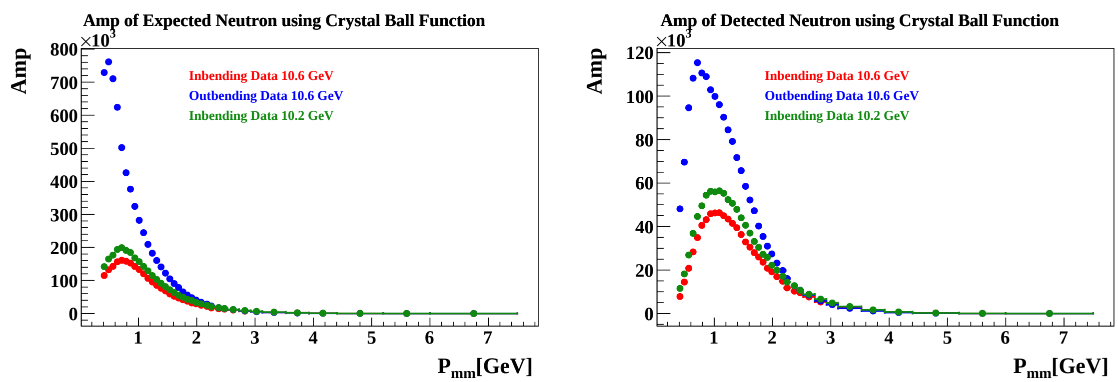

Figure B.8: The amplitude of the expected (left) and detected (right) neutron as a function of P_{mm} using Crystal ball + polynomial background.

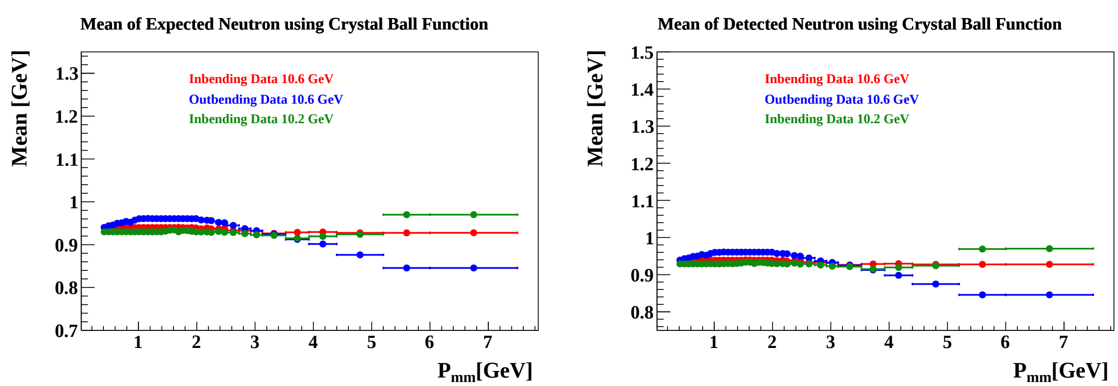

Figure B.9: The mean of the expected (left) and detected (right) neutron as a function of P_{mm} using Crystal ball + polynomial background.

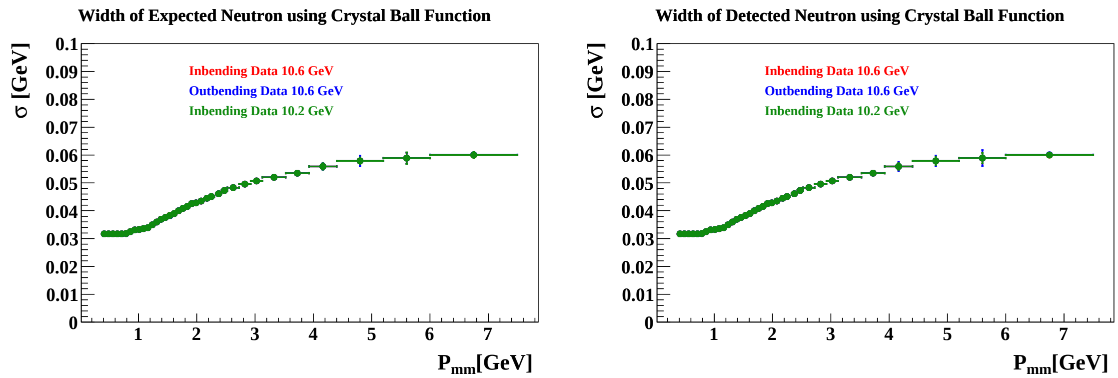

Figure B.10: The width of the expected (left) and detected (right) neutron as a function of P_{mm} using Crystal ball + polynomial background.

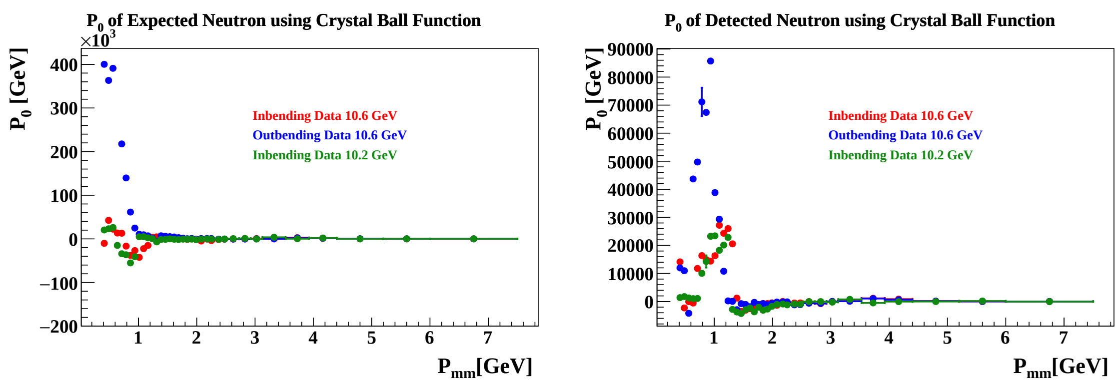

Figure B.11: The P_0 parameter of the expected (left) and detected (right) neutron as a function of P_{mm} using Crystal ball + polynomial background.

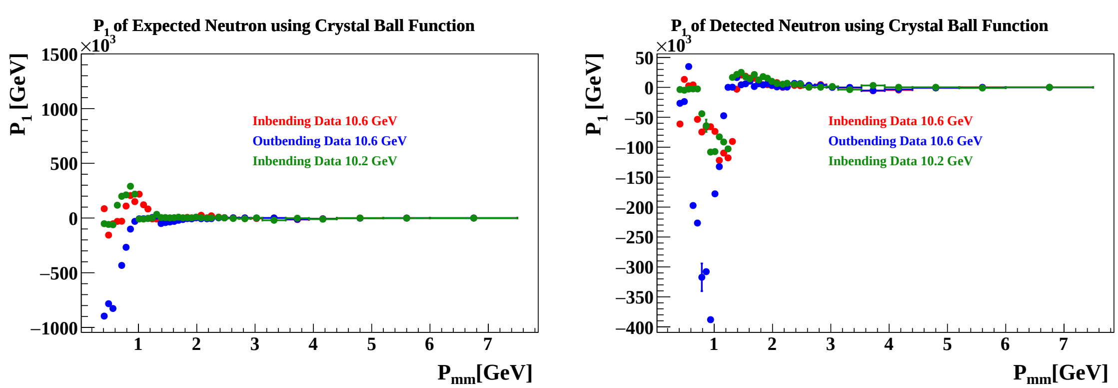

Figure B.12: The P_1 parameter of the expected (left) and detected (right) neutron as a function of P_{mm} using Crystal ball + polynomial background.

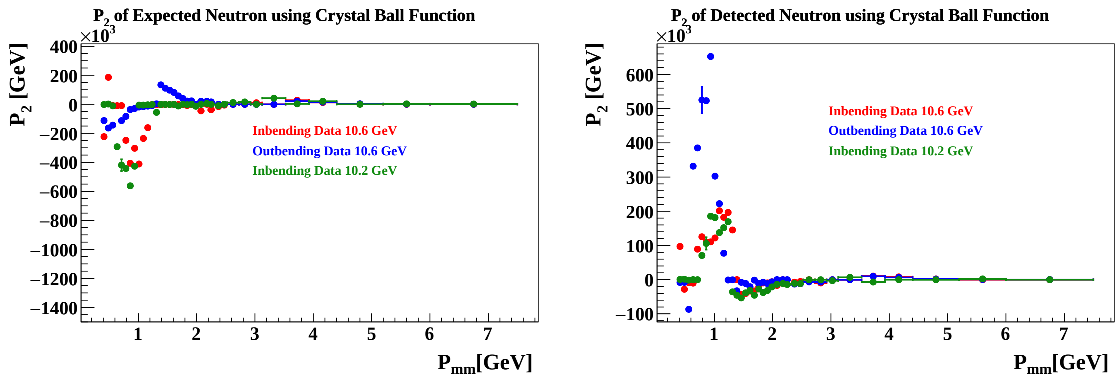

Figure B.13: The P_2 parameter of the expected (left) and detected (right) neutron as a function of P_{mm} using Crystal ball + polynomial background.

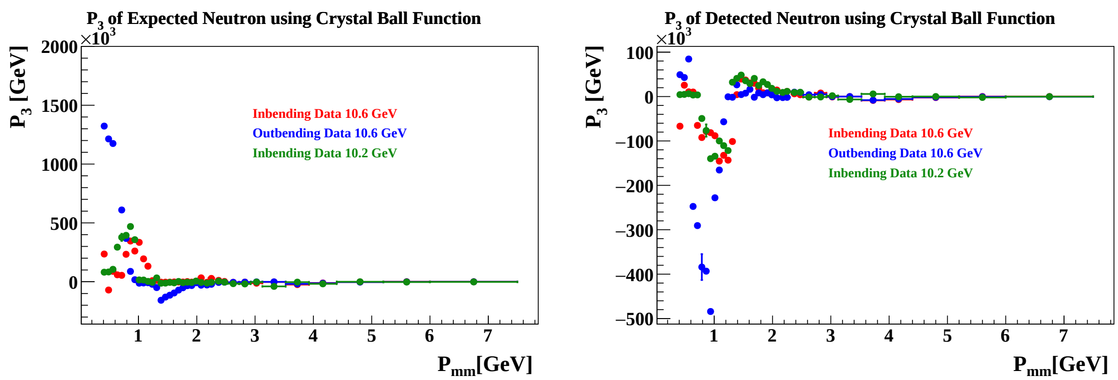

Figure B.14: The P_3 parameter of the expected (left) and detected (right) neutron as a function of P_{mm} using Crystal ball + polynomial background.

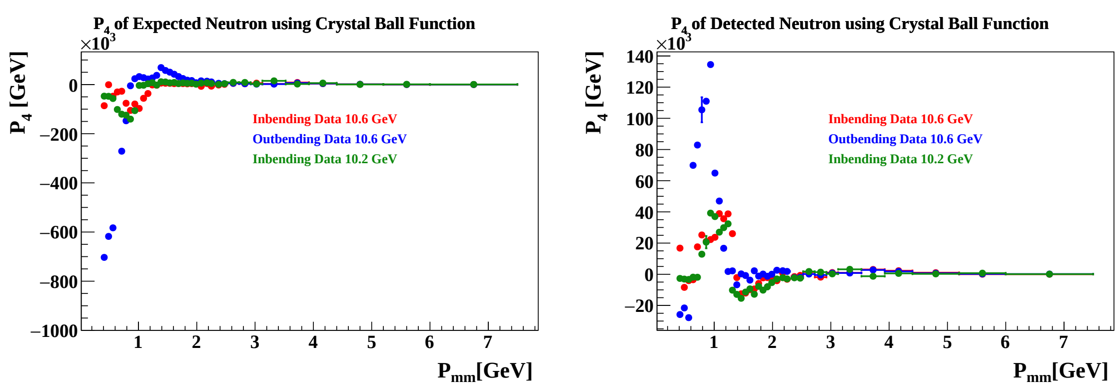

Figure B.15: The P_4 parameter of the expected (left) and detected (right) neutron as a function of P_{mm} using Crystal ball + polynomial background.

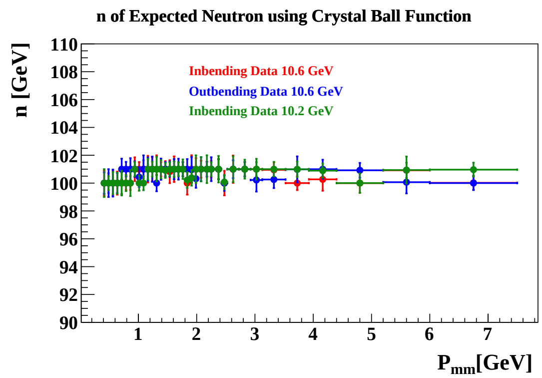

Figure B.16: The n parameter of the expected (left) and detected (right) neutron as a function of P_{mm} using Crystal ball + polynomial background.

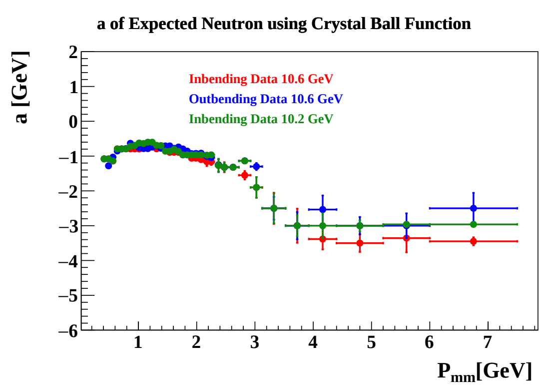

Figure B.17: The a parameter of the expected (left) and detected (right) neutron as a function of P_{mm} using Crystal ball + polynomial background.

APPENDIX C

Measured G_M^n values and errors

A table will be added that shows the final result of G_M^n and the statistical uncertainty for the three different beam energies individual as well as the weighted average of G_M^n and the statistical and systematic uncertainty

Q^2	10.2 GeV		10.4 GeV		10.6 GeV	
[GeV^2]	$G_M^n/\mu_n G_D$	σ_{stat}	$G_M^n/\mu_n G_D$	σ_{stat}	$G_M^n/\mu_n G_D$	σ_{stat}
4.89	1.2305	0.2051	1.1034	0.2956	1.3321	0.4369
5.33	1.2311	0.0624	1.3308	0.0849	1.3354	0.0885
5.78	1.1366	0.0450	1.1122	0.0495	1.1601	0.0524
6.24	1.1101	0.0457	1.0835	0.0489	1.1539	0.0522
6.73	1.1436	0.0519	1.1568	0.0569	1.2295	0.0617
7.23	1.1455	0.0603	1.1254	0.0651	1.2508	0.0732
7.72	1.1746	0.0723	1.1846	0.0797	1.1760	0.0809
8.23	1.1260	0.0815	1.1329	0.0893	1.2144	0.0979
8.94	1.1751	0.0803	1.2166	0.0887	1.2861	0.0957
9.90	1.0889	0.1080	1.1614	0.1270	1.3313	0.1449
10.93	1.1183	0.1682	1.1257	0.1979	1.2066	0.2004
12.06	1.0890	0.2497	1.1644	0.2486	1.2450	0.2780

Table C.1: Measured values of $G_M^n/\mu_n G_D$ and statistical errors for each dataset. The Q^2 values given are the central value of each Q^2 bin.

.

Q^2 [GeV^2]	$G_M^n/\mu_n G_D$	σ_{stat}	σ_{syst}	σ_{Total}
4.89	1.2077	0.1572	0.1349	0.2071
5.33	1.2830	0.0437	0.0512	0.0673
5.78	1.1355	0.0281	0.0351	0.0450
6.24	1.1140	0.0281	0.0201	0.0345
6.73	1.1719	0.0326	0.0221	0.0394
7.23	1.1669	0.0379	0.0339	0.0508
7.72	1.1782	0.0446	0.0380	0.0586
8.23	1.1526	0.0513	0.0331	0.0611
8.94	1.2195	0.0506	0.0355	0.0618
9.90	1.1710	0.0716	0.0390	0.0815
10.93	1.1462	0.1080	0.0615	0.124
12.06	1.1607	0.1488	0.0377	0.1535

Table C.2: Measured values of $G_M^n/\mu_n G_D$, statistical and systematic uncertainties from the waighted average. The Q^2 values given are the central value of each Q^2 bin.